An Explanation of the Behavior of Bottle-Shaped Struts Using Stress Fields

by

Cameron L. Sankovich, B.S.

Thesis

Presented to the Faculty of the Graduate School of

The University of Texas at Austin

in Partial Fulfillment

of the Requirements

for the Degree of

Master of Science in Engineering

The University of Texas at Austin

August, 2003

An Explanation of the Behavior of Bottle-Shaped Struts Using Stress Fields

Approved by
Supervising Committee:

Oguzhan Bayrak, Supervisor

James O. Jirsa, Supervisor

Dedication

To Larry, Carla, Lauren, Jim, and, of course, Kame`

Acknowledgements

For the physical production of the test specimens presented in this work, I would like to extend my deepest gratitude to Mike Brown who continuously and unselfishly helped in the fabrication and testing. I would also like to thank Annika Trevino for her endless application of instrumentation while continually smiling. Mike Bell, Blake Stassney, and Dennis Filip of the FSEL staff are also thanked for solving arising problems with great simplicity and efficiency. They are truly the engineers at FSEL.

For requiring an elevated train of thought, I would like to thank Dr. John E. Breen whose passing comment, “The specimens are trying to tell you something…your job is only to observe them” had a profound impact on the work presented here.

For never raising his voice in frustration with my stubbornness, I would like to thank my advisor Dr. Oguzhan Bayrak. His support and affable nature proved most valuable when the world was going to end.

For his willingness to assist in any task at any time, I would like to thank Mike Hagenberger, a true friend, whose sharp intellect and good humor was appreciated greatly and will truly be missed.

Jason K. Jones, S.E. is thanked for his infallible advice in anything ranging from specimen design to mixed drinks to deciphering code language for R-values of duel systems. Through his guidance, I was able

to catch glimpses of the overall picture encompassing structural engineering, which helped me immensely throughout my brief stay in Texas.

Heaven Yoshino is greatly thanked and appreciated for providing love, support, and a soothing voice from 2000 miles away. I would have been lost without her.

Lastly, I would like to thank the people who have supported my every endeavor. My Mother and Father have provided an environment in which mediocrity would be more difficult to achieve than excellence. I am extremely fortunate and grateful to have such wonderful people as my parents.

August, 2003

Abstract

An Explanation of the Behavior of Bottle-Shaped Struts Using Stress Fields

Cameron L. Sankovich, B.S.

The University of Texas at Austin, 2003

Supervisors: Oguzhan Bayrak, James O. Jirsa

The behavior of bottle-shaped struts was investigated using isolated concrete specimens with various amount and configurations of transverse reinforcement in which compressive stresses resulting from applied load through rigid plates was able to disperse creating transverse tensile stress within the specimens. The behavior of the specimens was observed and recorded to evaluate current provisions regarding compressive stress limitations, reinforcing requirements, and to unify the treatment of bottle-shaped struts by ACI 318-02 and AASHTO LRFD. The results from the experimental investigation indicated that both ACI-318-02 and AASHTO LRFD provisions for bottle-shaped struts are conservative in their specifications for compressive stress limits and reinforcing

requirements. Finally, a transition stress field developed by M. Schlaich was modified to model the observed behavior and failure mechanisms of the specimens, which was dependent on the amount of transverse reinforcement provided. The transition stress field exploits the tensile strength of concrete by incorporating a bi-axial failure criterion, with a statically admissible stress field with finite dimensions. The transitions stress field is presented as an alternate method of modeling the behavior of bottle-shaped struts.

Table of Contents

List of Tables

List of Figures

1.0 INTRODUCTION

1.1 HISTORICAL OVERVIEW

In the 1920's Richart [42] divided the total shear resistance of reinforced concrete beams into the contribution of shear resistance from the concrete Vc and the contribution from the stirrups Vs so that the nominal shear capacity can be expressed as Vn=Vc+Vs. The shear resistance of concrete was obtained through empirical observation while the contribution from the stirrups was obtained through truss models adapted from Ritter [43] and Mörsch [31, 32] who was the first to visualize truss mechanisms resisting applied force within reinforced concrete beams. The addition of the empirical Vc term dimmed the significance of truss models to many North American engineers, and as a result, no significant advancement was made in the area for 50 years.

Truss modeling in North America, saw a rebirth in the 1970's and 1980's with Mitchell and Collins [30] and Ramirez and Breen [37] using truss models and plasticity theory to predict combine shear, bending, and torsional behavior expanding on work done by Swiss contemporaries, Lampert and Thürlimann [24], and Marti [24]. The resurgence and extrapolation of truss models to wider ranges of structural elements and loading situations spawned the need for a unified approach to modeling of this type.

Schlaich et al.[45], in his 1987 journal paper *Toward a Consistent Design of Structural Concrete*, argued for the implementation of a single design concept applicable for all parts of concrete structures. This concept consisted of a generalized truss analogy in the form of strut-and-tie

modeling (STM). With strong theoretical explanation, finite element analyses, and results from limited testing, Schlaich logically showed that STM was accurate in predicting any behavior (within the accuracy of design) of cracked structural concrete in regions where Bernoulli's hypothesis remains a rational assumption (B-regions), regions of static or geometric discontinuity (D-regions), and even the anchorage of reinforcing.

STM is only an efficient design tool within D-regions. The design of B-regions with STM requires complex compatibility analysis to merge the gap between a lower bound STM equilibrium solution with an upper bound kinematic solution to achieve the same levels of efficiency for the design of B-regions by standard practice.

Schlaich [45], with his presentation of STM as an efficient design tool for D-regions, provided dimensioning guidelines, stress limitations for ductile behavior, and extensive design examples and fathered the current basis for STM. Subsequent work follows two primary paths-the work of Mitchell and Collins [30] on B-regions ultimately led to the Modified Compression Field Theory, while others (mostly at the University of Texas at Austin) began researching D-regions such as post-tensioned anchorage zones, dapped beam ends, and corbels, as well as, testing isolated components of strut-and-tie models such as nodes, struts, and most recently the anchorage of headed bars within C-C-T nodes.

With the foundation laid for the codification of STM by Schlaich, The Canadian CSA Standard [6], Ontario Bridge Code [7], and AASHTO [1] all adopted the provisions of STM for the general analysis of any D-region. The inclusion of Appendix A, *Strut-and-Tie Models,* in the ACI

318-02 raises the height of awareness of STM as a tool for analyzing and detailing D-regions by practicing engineers. The increasing use of STM by practicing engineers, variety of detailing problems, and range of solutions possible using this design tool raise many questions that will need to be answered through research and experimental study.

1.2 IMPETUS FOR STUDY

The decision by the Texas Department of Transportation (TxDOT) to conduct Research Project 0-4371, *Examination of the ASSHTO LRFD Strut-and-Tie Specifications,* was the result of questions and concerns raised by bridge engineers regarding the application of the AASHTO strut-and-tie model provisions to elements within their scope of design. The limitations of the AASHTO STM provisions as well as the discomfort felt by engineers initially using the these provisions when he displayed drawings for various strut-and-tie models considered to verify the capacity of an as-built bent cap section which had been misplaced in the field resulting in a 2 foot extension of the moment arm of the applied load. The strut-and-tie models considered by TxDOT engineers and the as-built reinforcing of the bent cap are shown in Figure 1.1.

Figure 1.1 A displays the initial truss model considered by TxDOT engineers that was immediately dismissed because the angles of inclination between the upper tie and struts I and II were too small for an acceptable compressive stress limit f_{cu} given by AASHTO equations 5.6.3.3.3-1 and 5.6.3.3.3-2 shown here by equations 1-1 and 1-2.

$$f_{cu} = \frac{f_c'}{0.8 + 170\varepsilon_1} \leq 0.85 f_c' \qquad (1\text{-}1)$$

$$\varepsilon_1 = \varepsilon_s + (\varepsilon_s + 0.002)\cot^2\theta_s \qquad (1\text{-}2)$$

f_{cu} = ultimate stress of the strut (ksi)

f_c' = concrete compression strength (ksi)

ε_1 = principal tension strain perpendicular to the axis of the strut (in/in)

ε_s = tension strain in tie steel crossing the axis of the strut usually taken as the yield strain of the reinforcing bars (in/in)

θ_s = angle between the axis of the strut and the axis of the tie that it anchors

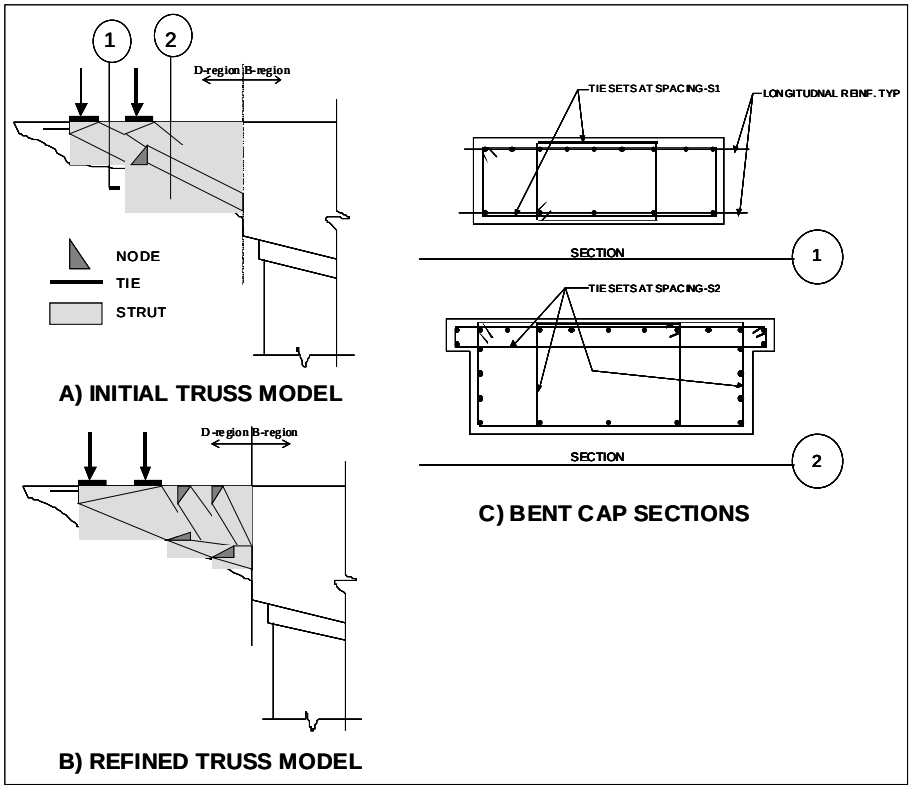

Figure 1.1 Strut-and-Tie Models and As-Built Reinforcing for TxDOT Misplaced Bent

TxDOT engineers were not satisfied with the model only having one vertical tie. They understood that the forces would flow according to the

stiffness of the in-situ placement of the reinforcement, and a more accurate model would therefore have a greater number of modeled vertical ties. Figure 1.1 B shows the model after some refinement was made and illustrates new uncertainties. The uncertainties about the model include the assumed geometry of the nodes and stress field under the applied loads, the geometry of the smeared nodes anchoring compressive struts at vertical ties, the allocation of actual vertical stirrups to a single modeled vertical tie, the geometry of struts anchoring vertical tension ties (closed stirrups) if modeled according to AASHTO provisions 5.6.3.3.2, and overall model optimization. The number of questions regarding the refined model led the TxDOT engineers to abandon the STM solution entirely.

It should be noted that bent cap STM is one prime for the combination of finite element analyses (FEA) and STM, as recommended by Schlaich [45]. The incorporation of a FEA would provide insight about basic strut orientation and possible node geometries.; however, a FEA can not answer all of the questions posed, especially those dealing with stress limitations (which vary subjectively in different codes).

The example provided by TxDOT displayed the difficulty in producing acceptable physical dimensions of a truss model that could be used to check limiting compressive stresses in the concrete. Furthermore, the stress limit for struts proposed by AASHTO given by equations 1-1 and 1-2 tend to cripple the overall model. The adoption of Appendix A, *Strut-and-Tie Models*, into the ACI 318-02 building code, which is congruent with the provisions for STM in the European FIB code [9],

provides another set of guidelines that can be evaluated using new experimental data.

1.2.1 Evaluation of ACI 318-02 and AASHTO LRFD STM Provisions

In order to define inconsistencies with current ACI / AASHTO STM provisions, and to highlight areas where research could be used to improve STM guidelines, typical TxDOT designed structural elements such as inverted T girders, pier caps, and pile caps, were alternately designed using strut-and-tie models. The iterative truss models were developed and dimensioned using the provisions provided by each code. The acceptability of these models was based on current AASHTO and ACI stress limitations coupled with serviceability requirements. The ratio of the reinforcing steel cage weight resulting from each model to the reinforcing steel cage weight produced by the original TxDOT design was computed as a measure of model efficiency assuming that traditional TxDOT designs provide safe, serviceable structures based on experience with and performance of the traditional designs.

As a result of this exhaustive exercise, specific areas where guidance is lacking in application of the provisions of each code, as well as, specific discrepancies between the provisions in different codes emerged and were noted. The following bulleted list summarizes these difficulties and discrepancies:

- discrepancies in the provisions for producing the physical geometry for singular nodes
- discrepancies in the provisions for producing the physical geometry of struts anchored by closed ties
- discrepancies in the provisions for the stress limits of struts
- discrepancies in the provisions for the reinforcement of bottle shaped struts

1.2.2 BOTTLE-SHAPED STRUTS

The last two items in the preceding list are inter-related, and were persistent problems in all the STM redesigns and represent prime topics for experimental study. Schlaich [45] first suggested the need for experimental study of the reinforcement of dispersed compression fields. Sanders [44], Burdet [17] and Thompson [47] called for further investigation into the capacity of struts in general after they observed that of bottle-shaped struts constantly failed at higher levels of stress than suggested by either AASHTO or CEB-FIP now FIB codes.

The AASHTO 5.6.3.3 STM provisions for strut capacity involve checking the stress of the strut on the smallest area governed by adjacent node geometry against a maximum stress produced by substituting Equation 1-2 into 1-1. Equations 1-1 and 1-2 were developed by Collins [30] based on data from deep beams and shell elements. The original derivations were developed for ties composed of stirrups crossing the paths of shear struts within deep beams at well-distributed intervals. The adaptation of these equations to the general STM case has not been verified by tests, nor has it been proven that these equations are adequate for such situations as compact elements like corbels or three-dimensional strut-and-tie models such as those which model pile caps [47].

The ACI specifications use basic design assumptions based on the condition of the concrete through which the strut passes, and the reinforcement available to resist transverse tension within the compression field. The strut to adjacent tie angle is limited to 25^o and the ultimate stress at the smallest cross section is given by equation 1-3:

$$f_{cu} = 0.85\beta_S f_c' \tag{1-3}$$

where β_S is chosen from the following conditions:

- struts passing through uncracked concrete in a uniaxial fashion (such as in the compression zone of a beam): $\beta_S = 1.00$
- struts passing through concrete in tension: $\beta_S = 0.40$
- bottle shaped struts with appropriate reinforcement: $\beta_s = 0.75$
- bottle shaped struts with no reinforcement: $\beta_S = 0.60$
- all other cases: $\beta_s = 0.60$

Reinforcement for bottle shaped struts must satisfy the following:

$$\sum \frac{A_{si}}{bs_i} \sin\gamma_i \geq 0.003 \tag{1-4}$$

A_{si} = area of steel in spacing, s_i, that crosses the path of the strut (in^2)

s_i = spacing of reinforcement crossing the path of the strut (in)

b = the width of the strut perpendicular to the axis of the crossing reinforcement (in)

γ_i = the angle between the axis of the strut and the axis of the crossing reinforcement; γ must be greater than 40^o if only one layer of reinforcement crosses the strut

Furthermore, equation 1-4 may be replaced by proportioning reinforcement based on 2:1 dispersion of compressive stresses. Three-dimensional strut capacities are considered by ACI, not to be influenced by reinforcing indicated in ACI RA.3.3:

> Often, the confining reinforcement given in A.3.3 ***(1-3)*** is difficult to place in three-dimensional structures such as pile caps. If the reinforcement is not provided, the value of f_{cu} given in A.3.3.3 (b) ***(β_S = 0.60)*** is used.

Figures 1.2 and 1.3 clearly depict the extreme differences between the acceptance criteria as provided by ACI 318-02 Appendix A and AASHTO LRFD strut-and-tie modeling provision for struts in which compressive stresses have sufficient room to expand within the confines of the structural element (bottle-shaped struts) creating associated transverse tension-a frequently occurring condition in most reinforced concrete structures. Figure 1.2 illustrates the capacities for bottle-shaped struts anchoring tension ties. Figure 1.3 illustrates the capacity specified for bottle-shaped struts not anchoring tension ties such as bottle shaped struts adjoining two C-C-C Nodes. The differences illustrated by these figures help to understand the a designer's dilemma with a design based on a strut-and-tie model acceptable for bridge structures (AASHTO) but unacceptable for building structures (ACI).

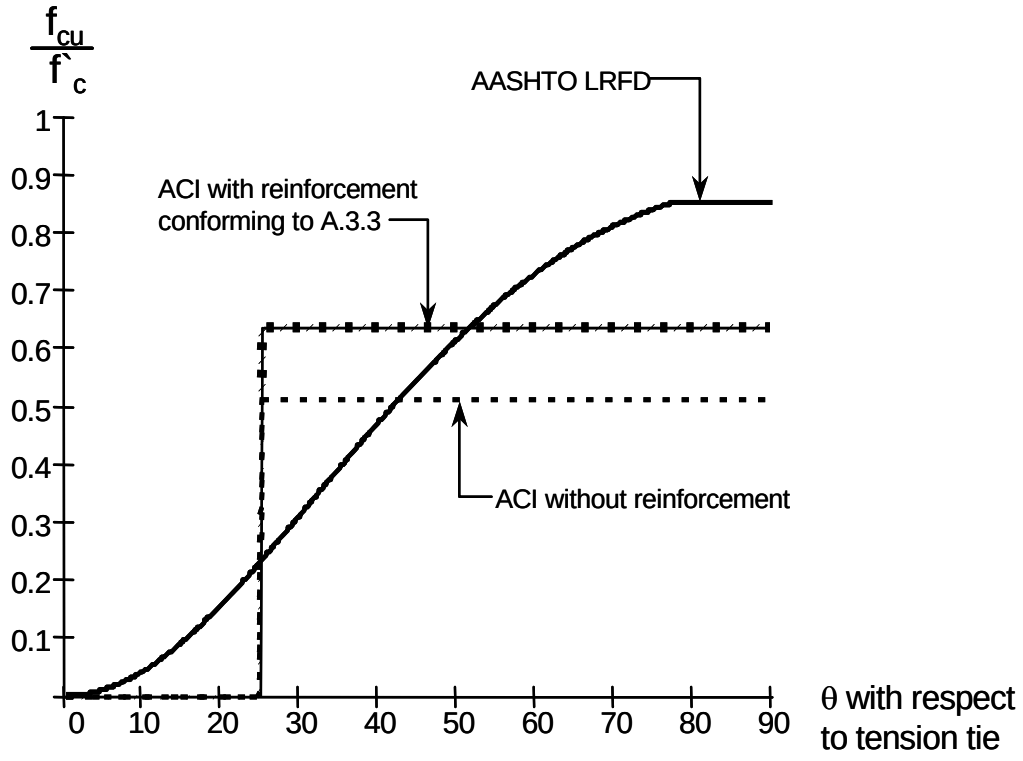

Figure 1.2 Bottle-Shaped Strut Capacity as a Function of the Angle with an Adjacent Tension Tie

The margin of discrepancies presented in Figure 1.2 and Figure 1.3 must be narrowed if STM is to achieve a status as a consistent, reliable, economical design tool.

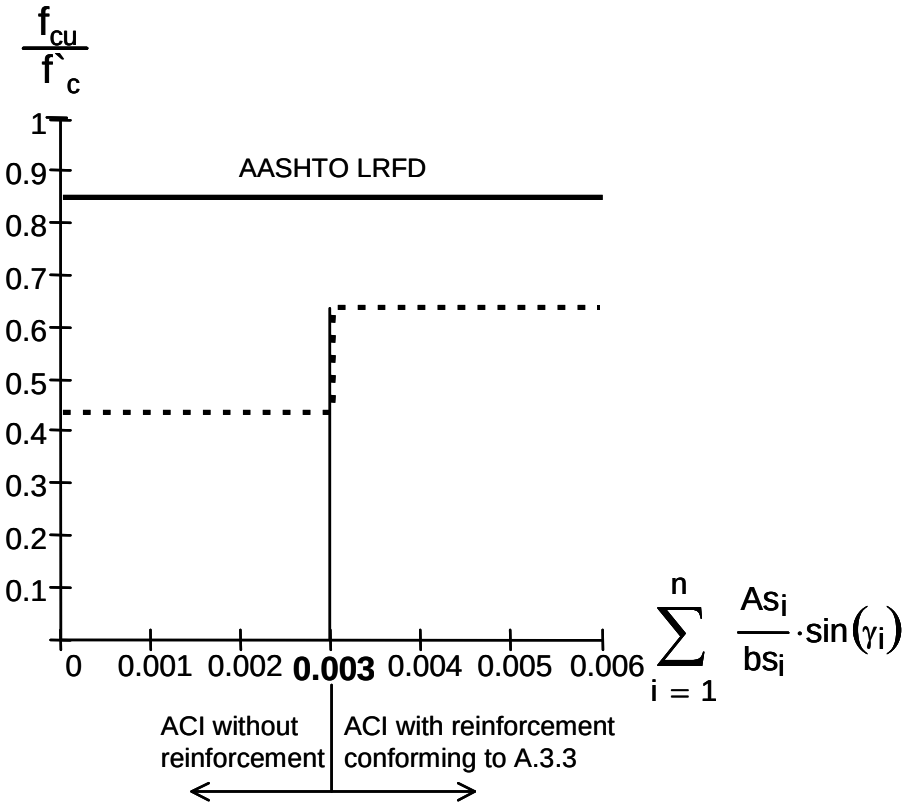

Figure 1.3 Bottle-Shaped Strut Capacity as a Function of the Confining Reinforcement Ratio

1.3 RESEARCH OBJECTIVES AND SCOPE OF THESIS

The investigation into the application of ACI and AASHTO STM provisions to TXDOT typical structural elements demonstrates the lack of guidance within both provisions and the discrepancies between provisions. Existing literature was reviewed to make sure that all applicable data was included in resolving the problems noted. Those areas where the experimental data was limited that questions and

discrepancies between the codes could not be addressed, were denoted as areas for possible research.

The work presented herein constitutes Phase I of Research Project 0-4371, *Examination of the ASSHTO LRFD Strut-and-Tie Specifications* sponsored by the Texas Department of Transportation. The objective of Phase I was to study the compressive stress limitations for bottle-shaped struts based on the effective amount of reinforcement available to confine the strut and to unify the treatment of bottle-shaped struts by ACI and AASHTO.

2.0 CURRENT STATE OF PRACTICE

2.1 INTRODUCTION

STM is a method that can both provide a conservative, lower bound estimate of the ultimate capacity of a structural concrete section and provide insight to proper detailing of structural concrete elements. The method is most efficiently employed in regions where point loads, reactions, and geometric discontinuities create states of stress that violate simple beam theory. The method may be used for any region of structural concrete elements regardless of the state of stress due to the method's strong basis in structural mechanics as argued by Schlaich et al [45]. Pragmatic North American designers, however, would find the method tedious in application where simplified equations may be used that have been substantiated by exhaustive experimental testing and result in ductile structural behavior. In light of this attitude by the professional society, STM has been delineated for use within disturbed regions (D-regions) exclusively.

The STM method is a lower bound plasticity solution that will result in a conservative estimate of the actual ultimate capacity of a section if:

- equilibrium is satisfied
- at no point does the material exceed its failure criteria
- detailing is such that sufficient ductility is provided to ensure plastic strains and rotations

Since structural concrete is heterogeneous material consisting of a non-ductile material (concrete) and ductile material (reinforcing steel) the last two items of the bulleted list are dependent upon each other, and the

proper interaction of the two ensures plastic behavior by forcing ductile failures of reinforcing steel prior to the non-ductile failures of concrete crushing or anchorage failure.

STM is a relatively new concept to North American engineers; although the basic concepts driving the method have been known and employed by European engineers for over a hundred years, North American research has not yet provided a consistent treatment of the yielding criteria of concrete to ensure plastic behavior; instead, most research has been concentrated on substantiating the method as a basic design tool for specific structural elements. When applying the method in practice, the production of the physical geometry of the truss models employed in the STM method may be argued as the most frustrating aspect of the overall STM process to engineers. STM allows complete autonomy in the selection of a specific truss model. With more experience engineers will find that while the absolute geometric definition of struts, tie, and nodes and finding the exact location of these members within the confines of the structural element under consideration are important; they are not as critical as satisfying the three items in the preceding bulleted list exclusively.

As an example, consider the bolt group connecting a gusset plate to a structural steel section of a braced frame. The designer is only concerned with equilibrium of forces in the analysis of the load path from the brace to the column. The designer ensures that the yield criterion of structural steel is met by specifying weld sizes, gusset plate thickness, and the number of bolts and their spacing based on the simple equilibrium

calculation. The actual path the forces take from the brace through the bolt group to the gusset plate through the welds and finally to the column web or flange is inconsequential since equilibrium is satisfied. The designer is able to achieve a safe design because the forces will redistribute themselves as appropriate through a completely plastic media.

2.2 PROCEDURE FOR PRODUCING A STRUT-AND-TIE MODEL

After overall structural analysis has been performed to determine exterior reactions, the designer must delineate the B and D-regions of the structural element under consideration by using Saint Venant's principle. The adjacent B-region forces are determined through cracked section analysis and placed on the adjacent D-region at the centroid on which they act. The D-region can then be isolated and loaded with any exterior reactions or loads and forces calculated from the B-region. The internal flow of forces is then visualized through intuition, experience, or with the help of a finite element analysis for complex situations. The designer then chooses uni-axial struts and ties placed in the basic orientation of the visualized forces. These struts and ties concentrate their curvature in nodes to form a truss. The "stick-model" truss is then analyzed using classical structural analysis to determine member forces. Reinforcement is portioned for the corresponding tension force and the reinforcement is placed such that the centroid of the reinforcement is concentric with the centroid of the modeled tension tie. Singular node dimensions are then estimated using code provisions. Singular nodes are defined as nodes whose geometry can reasonably be ascertained due to the deviation of a

highly concentrated stress field such as applied load through rigid plates with finite dimensions. On the other end of the spectrum, smeared nodes are those in which stress fields are deviated over a smeared area. An example of a smeared node is the deviation of a compressive stress field crossed by evenly distributed reinforcement in which the actual deviation of the stress field might spread over some length. An example of each type of node is shown in Figure 2.1. Simultaneously with the estimation of node dimensions, end critical strut dimensions are also defined. The member forces calculated from the "stick-model" are then checked against member capacities calculated by using the ultimate stress limits (dependent on code) multiplying by the estimated area at critical locations. Critical locations for singular nodes include the face under direct bearing and the strut/node face. After assuring that stress levels are less than ultimate, development lengths may be checked using code provisions. This process is iterative and is repeated if stress levels at nodes and struts exceed the maximum and/or anchorage is inadequate.

Detailed descriptions of the process are available in earlier publications on STM, but none is as complete as Schlaich et al.'s [45] 1987 work, *Toward a Consistent Design of Structural Concrete*. However, a comprehensive example regarding the physical production of a strut-and-tie model including the findings of all current research from 1987 to date is presented in 2.4.1.

2.3 EXPERIMENTAL INVESTIGATIONS

2.3.1 GENERAL

The scope of this research project encompassed the treatment of stress limitations for bottle-shaped struts based on the amount of effective reinforcement available within a concrete section to resist passive tensile stresses transverse to the direction of applied load. Earlier publications do not address this issue in depth; however, several publications described in the proceeding sections form the foundation of experimental research that produced guidelines for producing the physical geometry of strut-and-tie models and provided guidelines for application of the method in order to achieve safe and efficient designs.

2.3.2 NCHRP PROJECT 10-29

The National Cooperative Highway Research Program (NCHRP) initiated Project 10-29 at UT in 1986 with the objective to develop design procedures for end and intermediate anchorage zones for post-tensioned girders, slabs, blisters, and diaphragms. In general, the investigation proved STM to be a conservative approach for the design of anchorage zones. The conclusions were supported by the results of more than 50 laboratory tests. As well as showing that STM is a valid overall design approach, the project also provided the most comprehensive insight into critical regions of strut-and-tie models, provided guidelines on model dimensioning, and presented areas within STM that need further research.

2.3.2.1 Roberts

Roberts' [39] studied the local zone of post-tensioned anchorage zones. The local zone as defined by the NCHRP project, is the area of concrete directly ahead of the anchorage device usually consisting of concrete confined by spiral or ties. Twenty-eight isolated end anchorage specimens were tested to ultimate capacities of the end anchorage devices. In relation to STM, Roberts' tests [39] investigated the capacity available within confined C-C-C nodes. She concluded Equation 2-1, adapted from one proposed by Schlaich, best fit the data recorded.

$$P_{bearing\ strut} = 0.7 \cdot f'c \cdot A_b \sqrt{\frac{A}{A_b \cdot A_g}} + \frac{k \cdot f_y \cdot A_s}{(s \cdot d) \cdot \left(1 - \frac{s}{d_c}\right)^2} \cdot A_{core} \leq 3 \cdot f'c \cdot A_b \qquad (2\text{-}1)$$

$P_{bearing,\ strut}$	=	bearing capacity of the node or strut
A	=	the effective area, which is the maximum area of the supporting surface that is geometrically similar to the loaded area and concentric with it
A_b	=	bearing or strut area
A_g	=	gross area of the bearing plate
A_{core}	=	area bounded by the confining reinforcement
d_c	=	diameter of spirals or width of ties
k	=	4 for spirals and 2 for ties
s	=	the pitch of the spiral or spacing of ties

2.3.2.2 Sanders

Sanders [44] concentrated on the general zones for end-surface anchorages. Sanders focused on the verification of the adequacy of strut-

and-tie models for predicting anchorage zone capacity. This was achieved by developing specific strut-and-tie models for each specimen which entailed the specific dimensioning of nodes and struts where applicable, as well as, proportioning reinforcement to the modeled tie force. The ultimate load of each model was taken as the minimum load that caused either a compressive or tensile failure within the truss model. Maximum compressive stresses were taken as a baseline of $0.7f`_c$ plus additional capacity if confinement was present as derived by Roberts [39]. Maximum strut member capacities were established by multiplying the uniform stress limit to designated critical node and strut areas The maximum compressive load was taken as the sum of the strut capacities framing into the node ahead of the anchorage device. The maxim tensile capacity of the specimen was established through the equilibrium of specimens cracked down the specimen centerline with a known distribution of reinforcement as shown in Figure 2.4. The minimum of the maximum tensile capacity and the maximum compressive capacity was taken as the specimen ultimate capacity and agreed well with experimental results.

Sanders constructed 36 specimens in four categories as described in the following:

- 17 concentric anchorage specimens with straight tendons
- 6 eccentric specimens with straight tendons
- 8 multiple anchorage specimens with straight tendons
- 4 inclined anchorage specimens with curved tendons.

The concentric anchorage specimens provided the most insight to STM as it related to the scope of the research reported in this thesis. The models

used to predict the ultimate loads of these specimens are similar to those used for bottle-shaped struts. Sanders used two basic strut-and-tie models as shown in Figure 2.1.

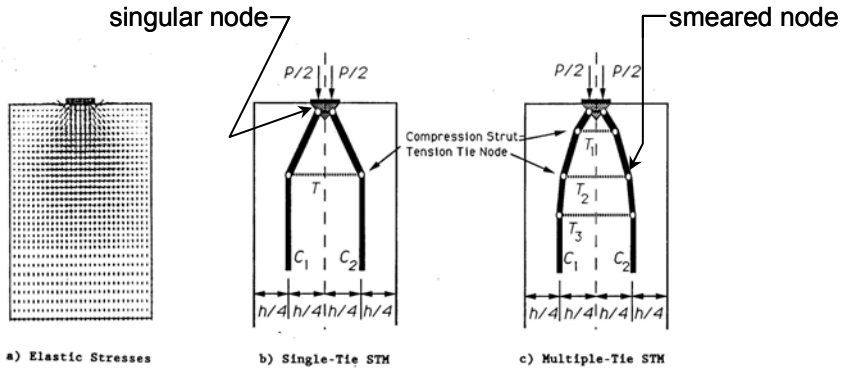

Figure 2.1 Strut-and-Tie models used in Sanders Specimens from [44]

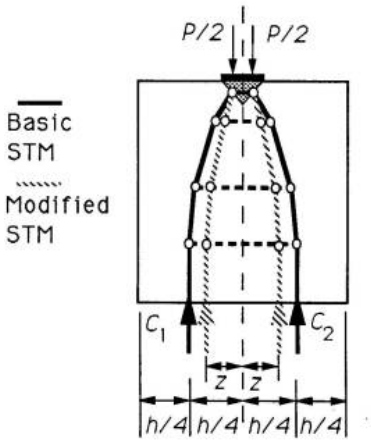

Figure 2.2 Modified Strut-and-Tie Model to Include the Full Plastic Capacity from [44]

As well as analyzing his specimens with this model, Sanders also produced a model that took into account the full plastic behavior of the specimen. Sanders achieved this capacity by moving the struts inward until the tensile capacity of the reinforcement equaled the compression strut capacity. The model used to estimate the full plastic behavior is seen in Figure 2.2.

The ultimate capacity of each specimen based on the elastic strut-and-tie model as well as the plastic strut-and-tie model was estimated by taking the minimum of the calculated tensile load as shown in Figure 2.5 with the estimated maximum compressive load carried by the singular node and adjoining struts. To estimate the compressive capcity, Roberts' [39] equation (2-1) was employed at the bearing surface, the node-strut interface, and the local zone-general zone interface of the singular node and adjacent struts. To employ equation 2-1, critical areas must be determined and depended on the bearing plate dimension and the angle of the strut as shown in Figure2.4. Figure 2.5, Figure 2.6, and Figure 2.7 illustrates how Sanders[44] defined these areas and on which planes the capacites were predicted.

$$\tan(\alpha) = \frac{\frac{h}{4} - \frac{a}{4}}{d_{centroid} - \frac{a}{4}}$$

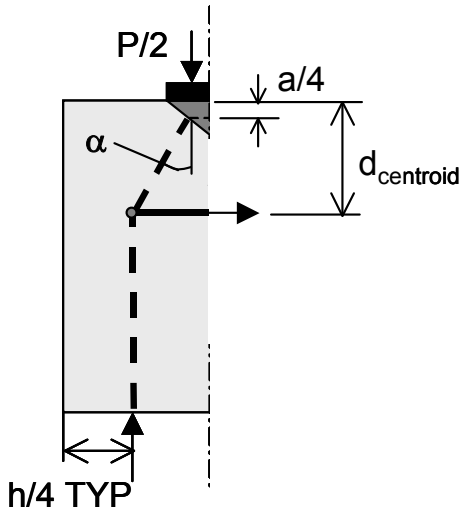

Figure 2.3 Determining the Angle of Struts from [44]

$$\sum_{T_j} M_x = 0 = \sum_{j} T_j \cdot \left(d_j - \frac{1}{4}\right) - \frac{P}{2} \cdot \left(\frac{h}{4} - \frac{a}{4}\right)$$

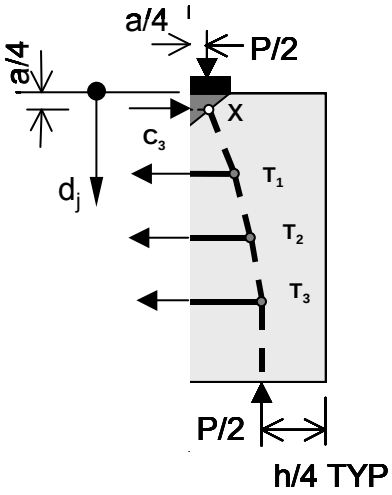

$$P = 2\,\frac{\left[\Sigma T_j \cdot \left(d_j - \frac{a}{4}\right)\right]}{\frac{h}{4} - \frac{a}{4}}$$

Figure 2.4 Determination of the Tensile Ultimate Load from [44]

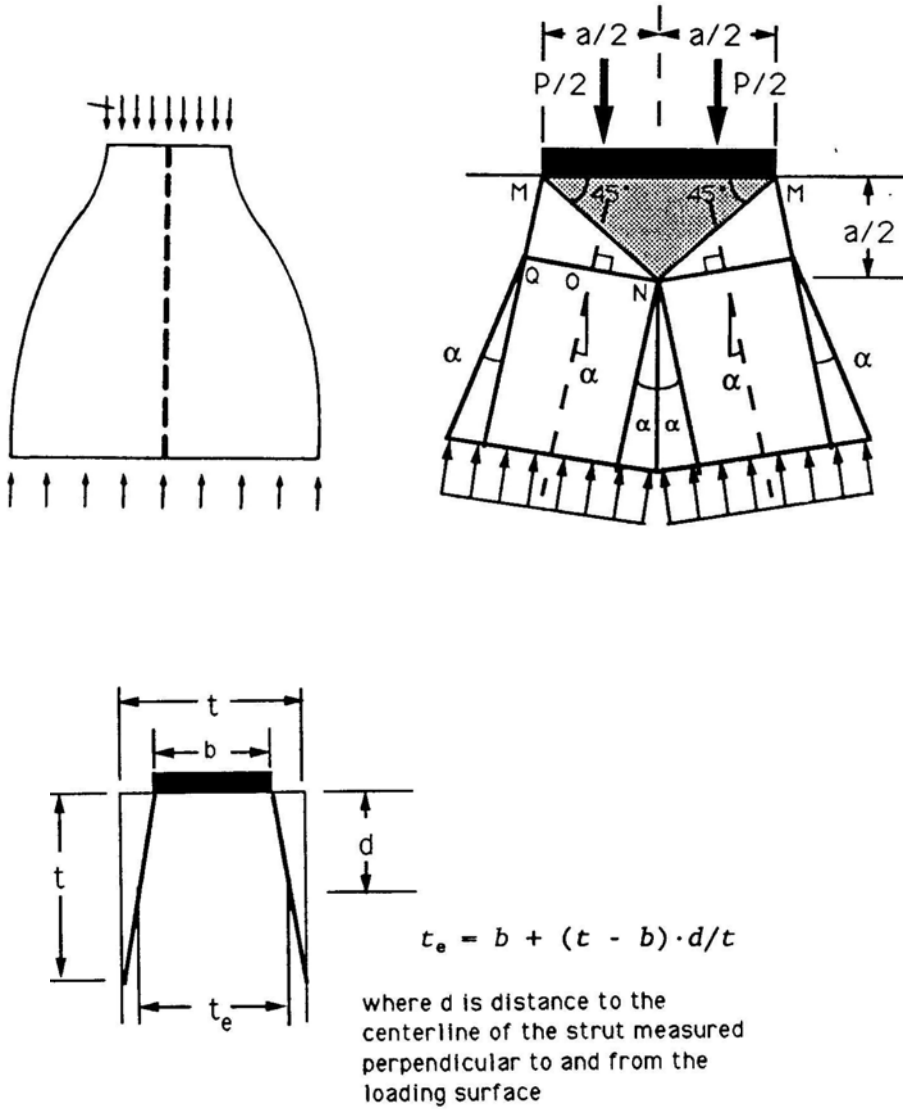

Figure 2.5 Singular Node and Strut Dimensions from [44]

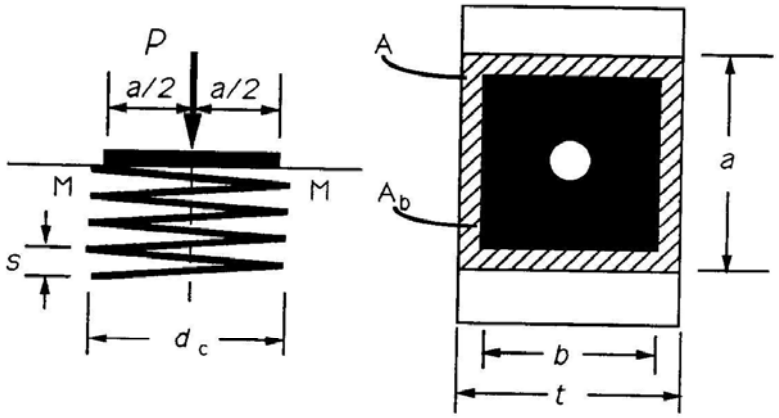

$$P_b = 0.7f'_c\sqrt{A/A_g}A_b + k \cdot f_y \cdot A_s/(s \cdot d) \cdot (1 - s/d_c)^2 \cdot A_{core} \leq 3f'_c \cdot A_b$$

a) Bearing Capacity

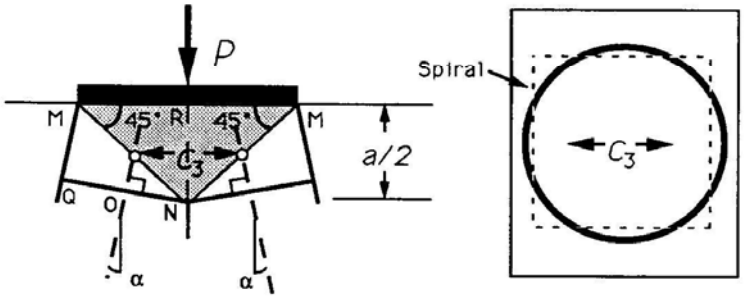

Z-Y Plane $C_s = [0.7f'_c + 4P/A_b]ab/2$

X-Y Plane $C_s = [0.7f'_c\sqrt{A/A_g}A_b + k \cdot f_y \cdot A_s/(s \cdot d) \cdot (1 - s/d_c)^2]ab/2$

Figure 2.6 Pertinent Planes and Equations for Singular Node and Strut Capacities from [44]

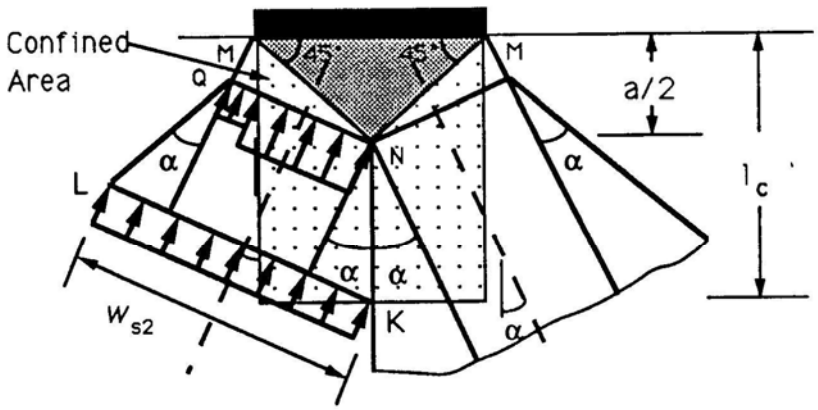

$$w_{s2} = a/2 \cdot (\cos(\alpha) + \sin(\alpha)) + 2 \cdot (l_c - a/2)\sin(\alpha) \leq h/2 \cdot \cos(\alpha)$$
$$w_{s2} = a/2 \cdot \cos(\alpha) + (2 \cdot l_c - a/2)\sin(\alpha)$$

Figure 2.7 Example of Area Defined for Local Zone-General Zone from [44]

From the results of the concentric anchorage specimens, it was concluded that ultimate capacities based on an elastic model are conservative with an average test to predicted ratio of 1.32 and a coefficient of variance of 0.19. The analysis of the specimens with the plastic strut-and-tie model yielded more accurate results; a test to predicted ratio of 1.12 and a coefficient of variance of 0.17.

2.3.2.3 Burdet

Burdet's [17] studied the blending of Sander's [44] experimental work with finite element analysis. Burdet concluded that the tensile contribution from the concrete is far more significant than that of bending or shear. The tensile contribution of the concrete, neglected in strut-and-

tie models, manifested itself by forcing concrete crushing leading to brittle failure and overall low ductility of the specimens. Significant redistribution of stresses was apparent which was substantiated by the behavior of specimens with tensile reinforcement placed in areas away from the elastic centroid of tensile stress whose performance was not substantially different from the behavior of those specimens with tensile reinforcement placed at the elastic centroid of tensile stresses. Furthermore, Burdet stated that the most important aspect for achieving good behavior in service and ultimate states is proportioning reinforcement based on equation 2-2, and placing this reinforcement at the elastic centroid of tensile stress given by equation 2-3. Burdet also concluded that concrete can resist compressive stresses in the about 0.75f`c if it is not confined by reinforcement or surrounding concrete, such conditions exist at the local-general zone interface and, in some cases, at the node-strut interface. He recommended that a check of concrete compressive stresses at a distance equal to lateral dimension of the anchorage device be made using equation 2-4. Finally, Burdet concluded that the accuracy of the strut-and-tie model for predicting compressive capacity decreases with the complexity of the model and, for these cases numerical analyses are desirable.

$$T_{burst} = 0.25 \cdot P\left(1 - \frac{a}{h}\right) + 0.5 \cdot P \cdot \sin(\alpha) \tag{2-2}$$

$$d_{centroid} = 0.5 \cdot \left(1 - \frac{2e}{h}\right) + 0.5 \cdot e \cdot \sin(\alpha) \tag{2-3}$$

$$f_{ca} = \frac{0.60 \cdot P_u}{a \cdot b} \cdot \frac{1}{1 + a\left(\frac{1}{b - \frac{1}{t}}\right)} \leq 0.75 f'c \tag{2-4}$$

T_{burst}	=	tensile bursting reinforcement
$d_{centroid}$	=	centroid of tensile stresses
F_{ca}	=	compressive at distance a ahead of anchorage device
P	=	Total load applied
a	=	lateral dimension of anchorage device
h	=	transverse dimension of the cross section in direction considered
α	=	angle of inclination of the tendon with respect to the centerline of the member
b	=	side length of anchorage device in the thin direction of the specimen
t	=	thickness of the cross section

2.3.2.4 Wollman

As the final phase of Project 10-29, Wollman [51] investigated the influence of end reactions on anchorage zones, as well as, investigated the applicability of strut-and-tie models to ribs, blisters, and diaphragms. Wollman's conclusions were based on all previous work done by Roberts [39], Sanders [44], and Burdet [17]. To facilitate the implementation of

STM, Wollman [51] proposed rules for developing strut-and-tie models shown in Figure 2.8

Wollman further substantiated the work done by Sanders [44] in producing the physical geometry of the strut-and-tie models used to analyze anchorage zones. The physical geometry of the models created by Sanders, Burdet and finally Wollman reflect bottle-shaped struts with a confined singular node at the anchorage device and were the foundation for the physical geometry of the strut-and-tie models used to describe the behavior of specimens for this research project.

To substantiate the work done by Sanders [44] in regard to the physical geometry of nodes and struts, he made a simple comparison of models used in the analysis of specimens that had slight but significant differences. The main differences were concentrated in the geometry of the singular nodes, but manifested themselves in the bearing capacity of the struts. The impetus of the second analysis by Wollman was that a node with a smaller dimension in the plane of loading (a/4 dimension in Figure 2.4) would ultimately reduce the amount of bursting reinforcement necessary by increasing the moment arm of the tensile reinforcement. Sanders [44] used non-hydrostatic node geometries in his analysis with the height of the node always equal to half the dimension of the anchorage device. Wollman [51] compared Sanders [44] models to ones that included non-hydrostatic nodes and fan shaped struts that have non-uniform stress distributions. The details and structural mechanics behind Wollman's [51] analysis are complicated and not necessarily relevant to the scope of this thesis, and therefore, are not shown here. The

importance of Wollman's [51] second analysis can be seen in Figure 2.10 which shows that the ultimate loads predicted by each assumed geometry of the singular node are very similar, and that assuming the struts to have uniform stress distribution not exceeding 0.7f`c is a reasonable assumption compared to the alternative.

Other important conclusions from this comparison include, the fact

rule	requirement	
1	satisfy equilibrium conditions	basic STM
2	satisfy material strength limitations	
3	satisfy simple beam theory at the boundaries of the anchorage zone	refined STM
4	select angle between struts and ties larger than 25 degrees	
5	orient the geometry of the strut-and-tie model on the linear-elastic stress trajectories	
6	split struts carrying large compression forces into a number of sub-struts	
7	keep practical reinforcement arrangements in mind when selecting the orientation of the ties	
8	avoid inefficient load paths	

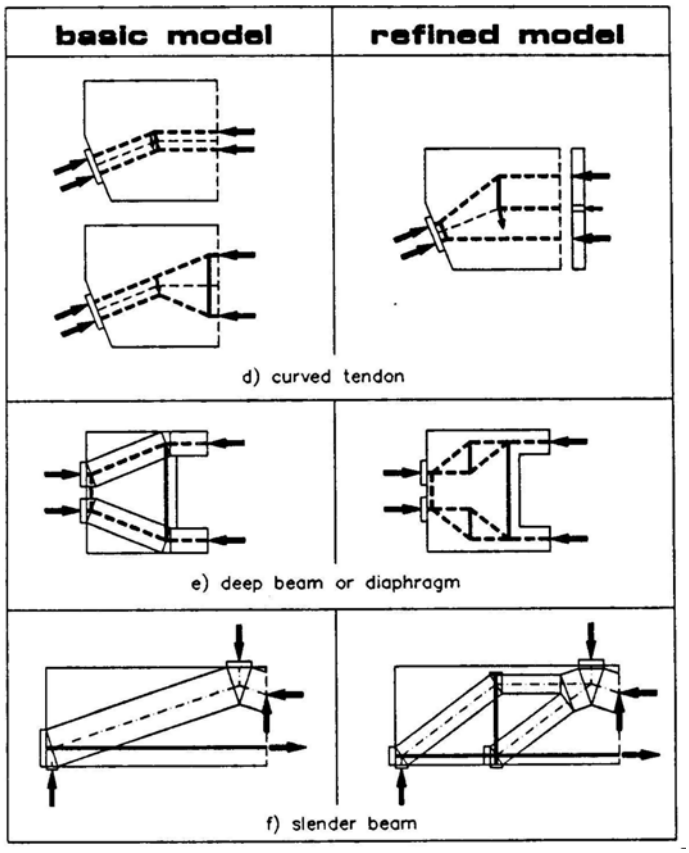

Figure 2.8 Rules for STM from [51]

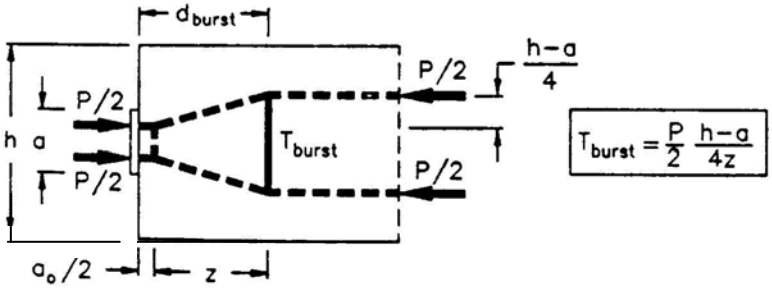

		A strut-and-tie model (code procedure)			B strut-and-tie model (Section 3.4)		
specimen	P_{test} (kips)	calc f_c / max f_c	P_{calc} (kips)	P_{test} / P_{calc}	a_o / a	P_{calc} (kips)	P_{test} / P_{calc}
B3	335	0.80	296	1.13	0.41	306	1.09
Beam1	315	0.91	332	0.95	0.58	322	0.98
Beam2 (LE)	-	0.71	373	-	0.30	405	-
Beam2 (DE)	445	0.66	363	1.23	0.29	401	1.11
Beam3 (LE)	380	1.00	359	1.06	0.72	336	1.13
Beam3 (DE)	-	0.97	363	-	0.67	332	-
		average		1.09	average		1.08
		standard dev.		0.10	standard dev.		0.06

Method A Sanders non-hydrostatic node geometry

Method B hydrostatic node and and fan-shaped struts

f/fc_{max} level of stress in the struts relative to 0.7f'c

a_o height of node in the direction of loading assumed to be a/4 for method A

Figure 2.9 Comparison of Strut-and-Tie Models Varying Node Geometry from [51]

that only live end model for beam 3 predicted a failure of concrete crushing and all others predicted a failure of the tensile reinforcement, yet the laboratory experiments all failed by concrete crushing at the local zone-general zone interface. In another important comparison conducted by Wollman [51], he predicted the failure of the same specimens using only a simple compressive stress check provided by Burdet [17] using equation 2-4. The four laboratory specimens yielded results with mean test to predicted ration of 1.09 with a standard deviation of 0.13 using equation 2-4.

Further adding insight relative to the scope of this investigation, Wollman [51] made a concise statement about the role of bursting reinforcement within the end-anchorage specimens. He concluded that role of bursting reinforcement was to resist direct tensile stress, not to increase effective concrete strength in compression. The bursting reinforcement plays no role until the concrete has cracked at which point the reinforcement is utilized through the redistribution of stresses resulting from the loss of stiffness available from the concrete acting in tension. After cracking has occurred, the main role of the reinforcement is to reduce the dispersion of compression radiating from the point of load application. If no reinforcement is present then the failure mode is purely related to the loss of shear friction at the strut-node interface as illustrated in Figure 2.10.

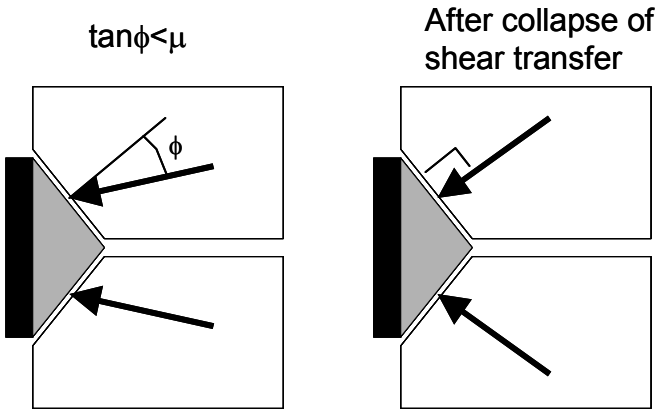

Figure 2.10 Collapse of Shear Transfer from [51]

2.3.3 THOMPSON

Thompson [47] investigated CCT nodes with the anchorage of the tension tie provided by headed reinforcement. There are some important aspects of Thompson's work that relate to the scope of thesis and will briefly be presented here.

In two of Thompson's [47] specimens, he investigated the in-plane and transverse-plane splitting behavior of bottle-shaped struts to investigate where splitting of the strut initiates. The two specimens are shown in Figure 2.11. The results of these two specimens revealed that the transverse strain distribution was similar to that of a concrete cylinder under the loading of a double punch test in which tensile strains are highest at the application of load and lowest at the center.

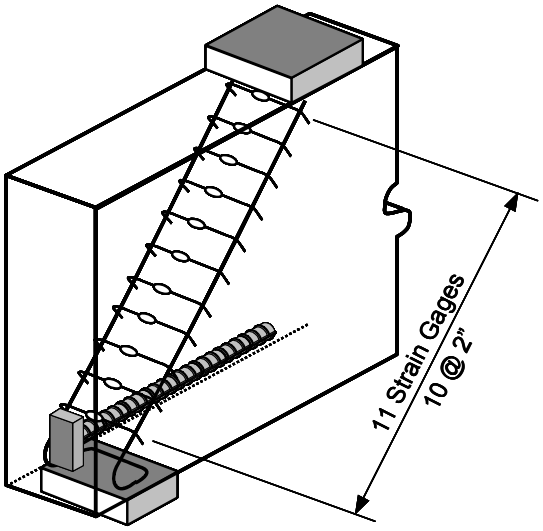

A) Strain Gauges measuring Transverse Splitting Strains

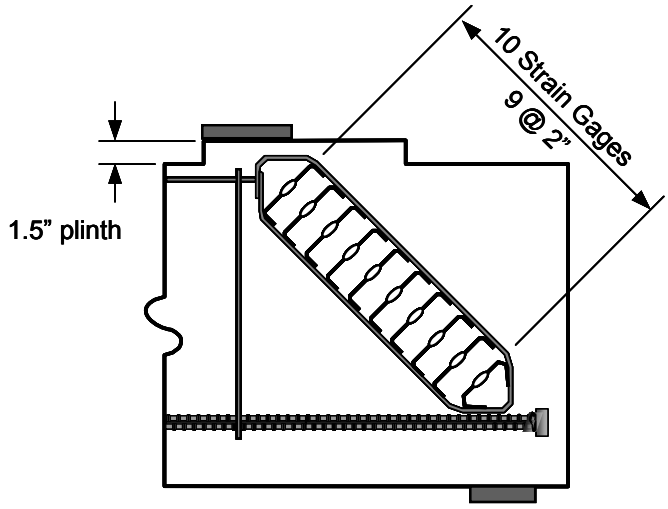

B) Strain Gauges measuring In-Plane Splitting Strains

Figure 2.11 Two of Thompson's CCT Node Specimens Measuring In-Plane and Transverse Splitting of Bottle-shaped Struts from [47]

This is opposite to the behavior typically modeled using bottle-shaped struts. The in-plane strain results indicated that splitting occurred at the CCT node, and strains increased at the center once a crack parallel to the strut formed. The capacity of the section reached ultimate just before this crack formed and lost capacity slowly as further load was applied and the crack widened. This might indicate that, if the strut was reinforced across the crack, the final capacity could have been higher.

Thompson also investigated the efficiency factor for the bottle-shaped struts produced through the geometry and loading of his specimens. The efficiency factor is defined as the ultimate stress on the strut face normalized to $f`_c$. The area of the strut face was determined by the bearing plate and the head size of the headed bar and assumed to be trapezoidal. The efficiency factors calculated by Thompson [47] were far greater than those provided by ACI 318-02. The results also refute the AASHTO LRFD provisions that if accurate, would have shown at least a trend of higher efficiency as the strut angle increased using a simple yield strain of .002 in equations 1-1 and 1-2.

Finally, Thompson's series of confined specimen tests which are the most likely configuration of reinforced bottle-shaped struts within structural concrete having reinforcement provided as closed stirrups showed no trend in of increased strut capacity as the confinement ratio of $A_s/(bs)$ increased. Comparing the five confined specimens with specimens that had the same overall configuration with out the stirrup reinforcement (control specimens) showed that the strut capacity was more sensitive to the tension reinforcement end detail; hence the strut

capacity was more sensitive to the node formed by the anchorage of reinforcement. A plot comparing the like specimens with and with out confinement is shown in Figure 2.12 which displays the maximum strut force normalized with respect to the concrete strength.

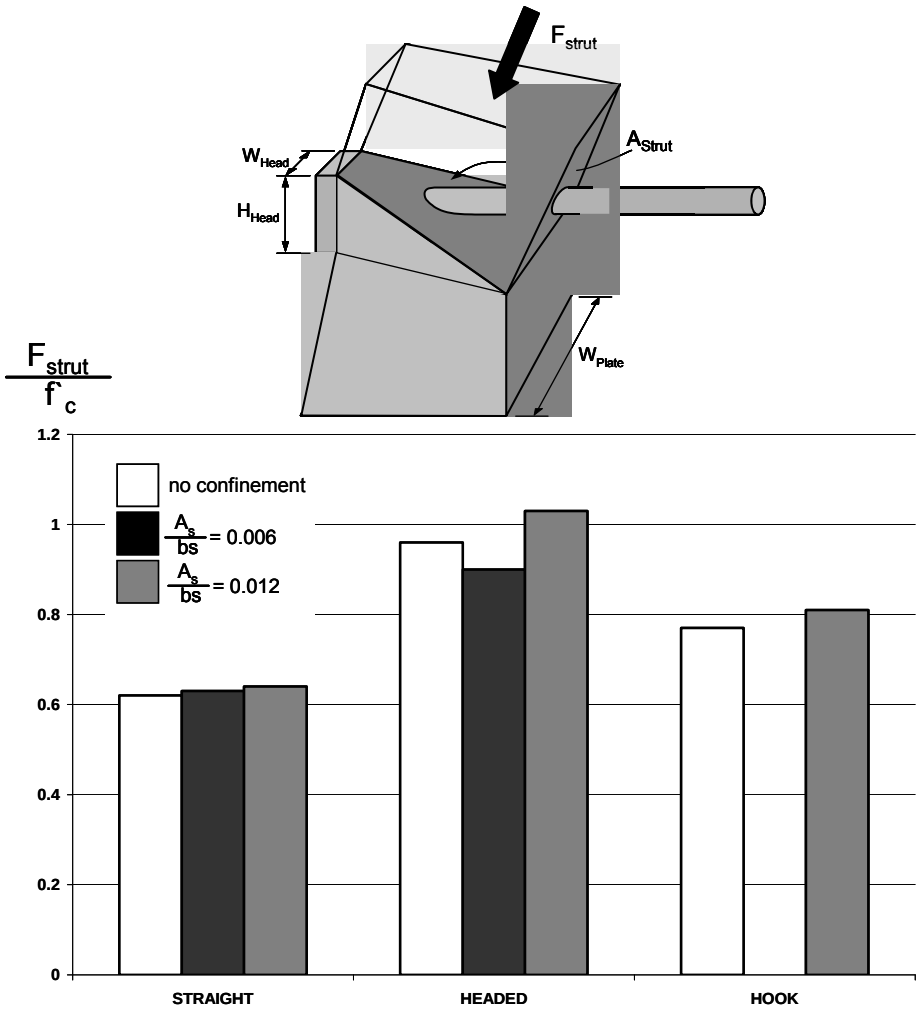

Figure 2.12 Reinforced Bottle-Shaped Strut Comparison from Thompson's [47] CCT Node Specimens

The bearing face of the strut is not represented in the plot because it remains constant with respect to the main tension reinforcement end detail.

2.4 DESIGN EXAMPLE

To best illustrate the current state of practice a design example is shown is the following section with additional step-by-step commentary. The design example is intended to display all of current modeling techniques acquired throughout the literature with emphasis on the findings presented in section 2.4. The design example is only bounded by the limitations set forth by the current ACI 318-02 Appendix A and the AASHTO LRFD 5.6.3 STM provisions in regard to stress limitations and guidelines set forth for the physical geometry of struts, ties, and nodes. Calculations are presented in parallel to display similarities and differences of the provisions of each major North American code authority.

The drilled shaft cap is presented here whose physical geometry creates an ideal situation for the designer to exercise his own judgment in the creation of the truss model, autonomous from any other condition other than satisfying internal and external equilibrium.

This element was chosen for illustration before other commonly illustrated models such as the strut-and-tie model for an inverted T-girder shown in Figure 2.13. Models such as the one shown in Figure 2.13 have been reproduced in many publications and are “boiler plate” reproductions that do not display the wide variability with the STM process. The goal of the design example presented in 2.4.1 is to display the range of modeling

procedures inherent in the STM method; all of which will result in lower-bound estimates of the actual ultimate capacity of the section if equilibrium is satisfied and at no point does the material exceed its failure criterion.

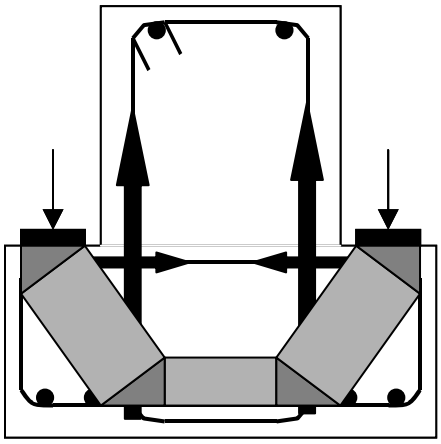

Figure 2.13 Inverted T Girder, Widely Accepted Strut-and-Tie Model

2.4.1 TxDOT Drilled Shaft Cap.

The design example presented here represents one strut-and-tie model for a drilled shaft cap under a single loading condition. The load case chosen was the factored vertical load that produced the largest reaction in the drilled shaft. This load case may not represent the most severe conditions within the drilled shaft cap; however, the limited structural calculations provided by TxDOT did not show any other factored loads because the cap was designed using allowable stress. Factored loads were desired to compare the LRFD specifications for STM within ACI 318-02 and the AASHTO LRFD.

The drilled shaft cap provides the base for a 45 ft. tall precast segmental column supporting an elevated highway. The TxDOT drawing showing an details of this structural element is shown in Figure 2.15.

To begin the process of designing an element using the strut-and-tie method, the designer must first establish the B and D regions of the structural element under consideration as shown in Figure 2.16. Once the D-region is established, a truss model may be chosen such that the tension and compression members are aligned with direction of principal tensile and compressive stresses. A finite element analysis may be performed at this point to determine the elastic flow of stresses from which the orientation of members within the truss model can be more easily visualized. For this example, a finite element analysis proves to be superfluous because the flow of forces from the column to the drilled shafts through the cap can easily be visualized.

Once the flow of forces can be visualized through, experience, intuition, or the help of a finite element analysis, a truss model can be established with members orientated in the general direction of these forces. Some candidate truss models are shown in Figure 2.17

Since strut-and-tie modeling is a lower bound solution, any model chosen which is in equilibrium with applied load, has sufficient ductility to ensure plastic rotations, and meets all specified failure criteria is acceptable and will provide a conservative or lower bound estimate of the actual ultimate load.

This selection of the strut-and-tie model often proves to be most difficult for designers who would like to immediately find the optimum

solution for each problem. To help designers meet this objective some rules of thumb regarding the optimization of a model for the most favorable structural behavior have been defined by Schlaich [45],

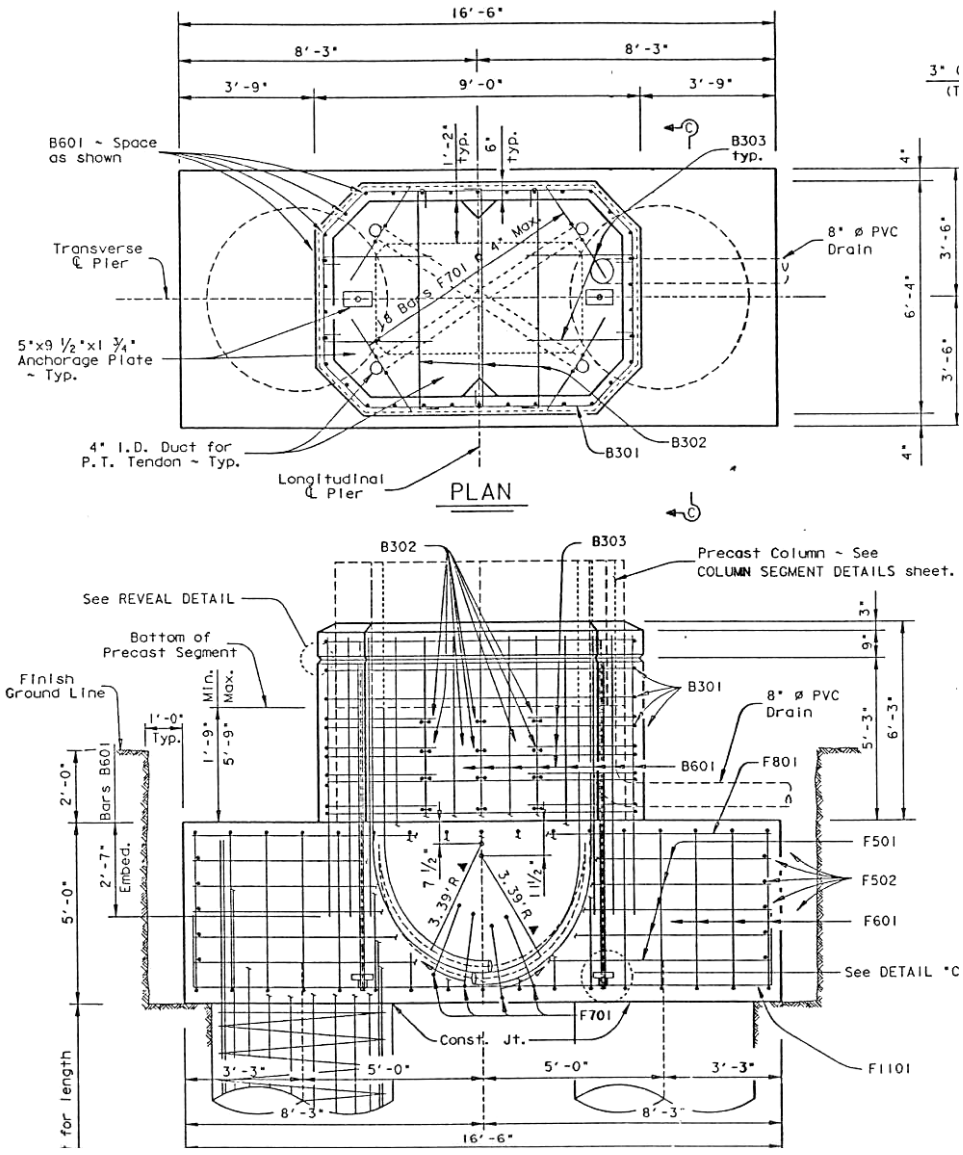

Figure 2.14 TxDOT Elevation of the Drilled-Shaft Cap

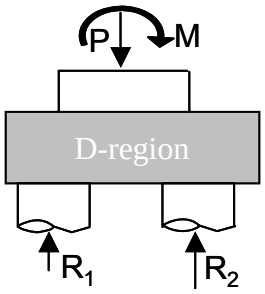

Figure 2.15 Separation of the Structural Element into B and D Regions

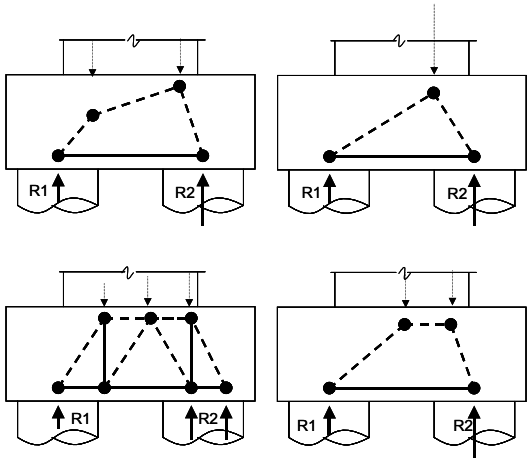

Figure 2.16 Candidate Truss Models for Drilled-Shaft Cap

Burdet [17], and Wollman [51].

For this example several iterations of truss models were considered relying on intuition, experience, and guidance provided by Schlaich et.al, [45] as well as any information applicable in the resources listed and discussed in this chapter. The process in which the final model was achieved is explained in the following paragraphs and figures.

One crucially important aspect of strut-and-tie modeling easily overlooked by inexperienced designers is the accurate placement of

applied loads on the boundaries of the D-region under consideration. In most cases this step is fairly simple as shown in Figure 2.17 in which the D-region of a dapped end beam is isolated and the forces applied to the D-region from external loads and adjacent B-regions are shown. In this example the forces acting on the D-region can be ascertained by simple statics and bending theory. The bearing plate and the Whitney compression block provide easily derived stresses from which singular nodal dimensions can be estimated. These nodal dimensions drive the angles and dimensions for the entire truss model.

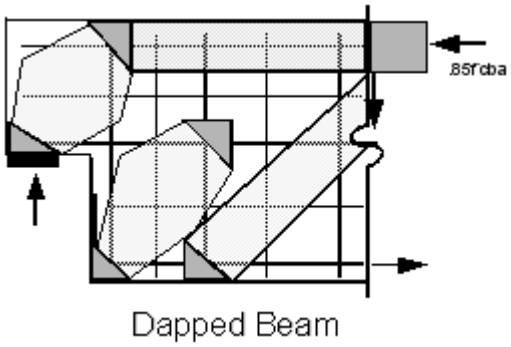

Figure 2.17 Forces acting on the D Region of a Dapped Beam

In the case of the drilled-shaft cap, there are no bearing plates and the stresses from the adjacent B-regions can not be as easily ascertained leaving ambiguity in the dimensioning of singular nodes which, as mentioned above, drive the overall geometry of the truss model. An analysis may be carried out to derive the depth of the neutral axis of the pre-cast column; however, the compressive stresses from the column must first pass through the cast-in-place pedestal before reaching the cap. The manner in which these stresses disperse through the pedestal may

be complicated and requires further analysis which in turn decreases the efficiency of strut-and-tie modeling for designers. In order to alleviate this problem, it was decided to treat all nodes at the pedestal-cap interface as smeared nodes with ambiguous dimensions instead of having one singular node with dimensions in proportion to the compression zone of the precast column as shown in Figure 2.18. This decision drove the formation of the final model. The stresses acting on the D-region from the adjacent B-region were obtained through combined elastic bending and compression in the form of $\sigma = P/A \pm Mc/I$ and is shown in Figure 2.19 broken up into four areas of stress for which resultant forces can be computed.

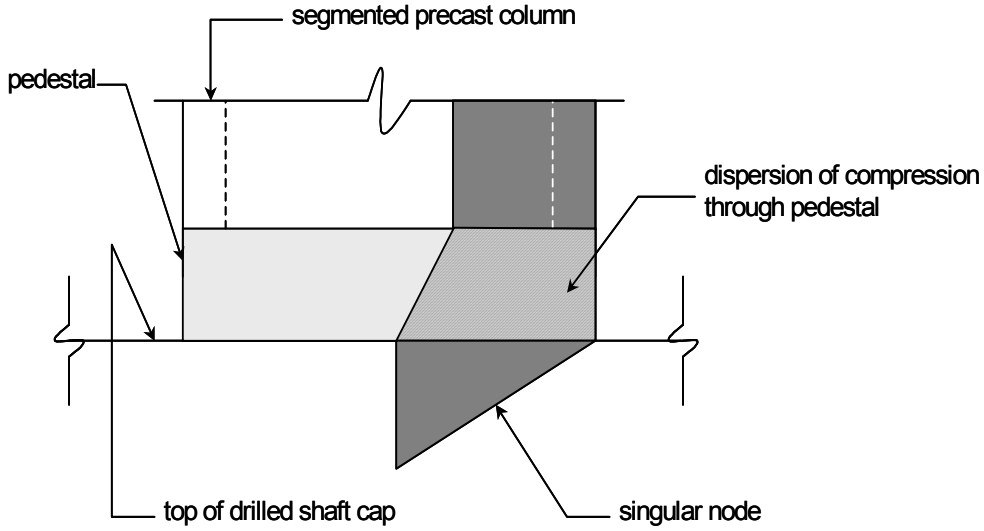

Figure 2.18 Dispersion of Compressive Stresses through the Pedestal

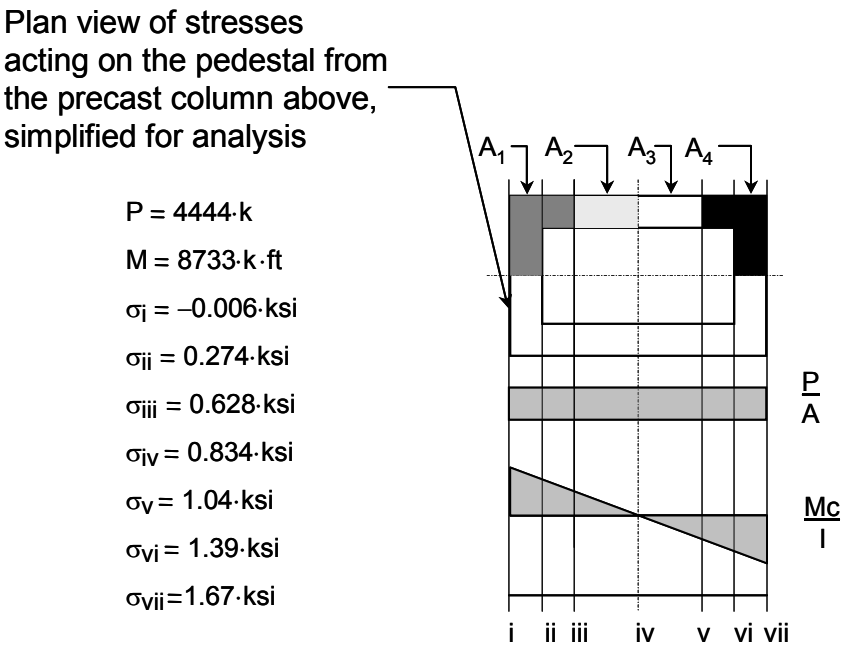

Figure 2.19 Analysis of Stresses acting on the D Region from Adjacent B Regions

The sub-division of the stresses into resultant forces is another matter that must be taken into consideration. A large number of sub-divisions will yield a more accurate depiction of the flow of forces; however, the designer must balance the number of sub-divisions with simplicity of analysis in order to achieve the efficiency of this design tool. After some iteration a decision to divide the pedestal into 4 distinct areas was arrived that balanced an accurate depiction of the flow of forces and simplicity of analysis. The four resultant forces locate the nodes of the upper chord of the truss model. The resultant forces acting on A_1 through A_4 in Figure 2.19 is shown in Figure 2.20.

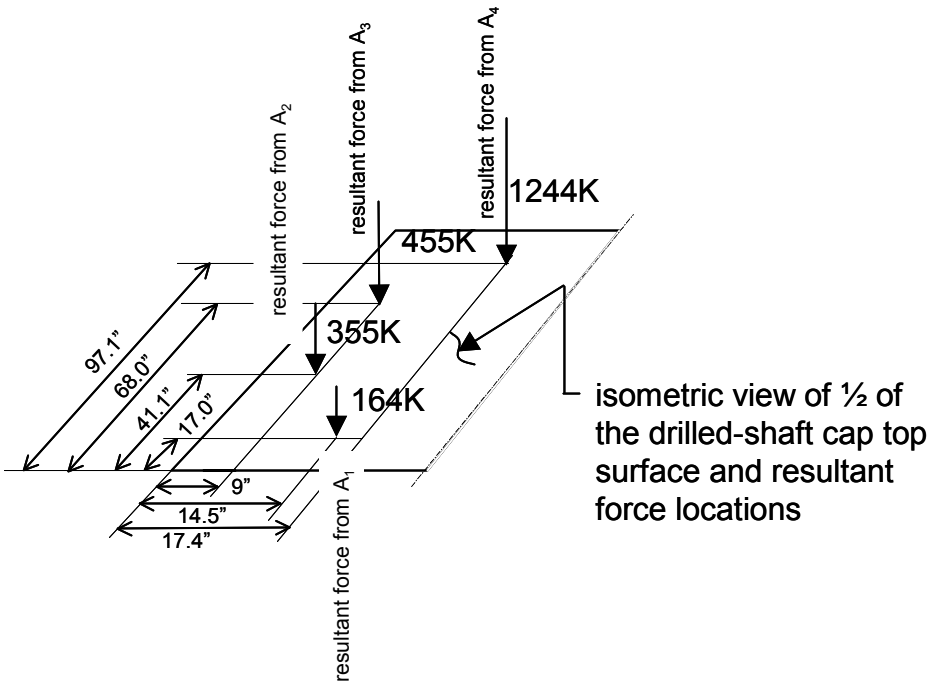

Figure 2.20 Resultant Forces from the Analysis Shown in Figure 2.19

Figure 2.20 clearly shows the three-dimensional nature of this problem; however, for ease of analysis the forces on both sides of the axis of symmetry were added and placed at the centerline of the cap. Once the location of the resultant forces are known the node locations of the upper chord of the truss model at the pedestal-cap interface are defined and the truss model can be finalized. The final truss model chosen was shown in Figure 2.21.

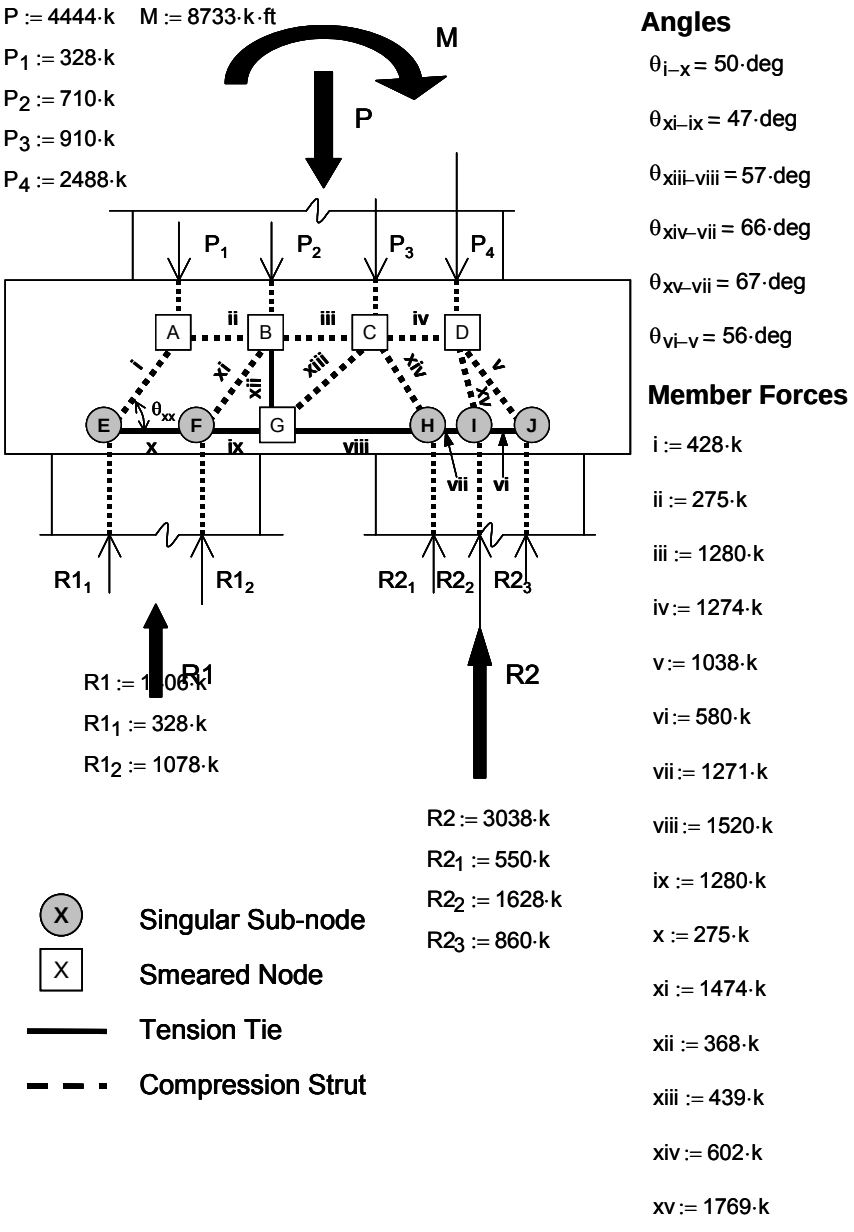

Figure 2.21 Final Truss Model

The final truss model chosen was strictly based on the judgment of the designer, and the following items were considered in the selection of this model:

- Based on the recommendation of Schlaich et al [45], an optimal model is one that exhibits minimal strain energy that is assumed to be concentrated in the ties. This model exhibits this property although it has an internal vertical tension tie. The simple triangular and trapezoidal models shown in Figure 2.17 only have one main tension tie; however, the tension ties within these models exhibit tension forces ranging from 1.5-2.25 times the tension force in member viii shown in Figure 2.21.
- The model subdivides the forces flowing to each node at the drilled shaft / cap interface into separate forces in reasonable proportion to separate sub-nodes. This deviation of forces to a single node acting over a large area provides insight into the actual flow of forces.
- The model subdivides the stresses acting on the D-region from the adjacent B-region into 4 resultant forces, which provides a favorable balance between the actual flow of forces and easily analyzed model.
- The model chosen illustrates a truss that is statically determinate with no compression members crossing each other. There is no need to complicate the analysis with indeterminate trusses. Equilibrium was achieved by sub-dividing the reactions in proportion to the vertical component of struts at each location.

In describing the model further, the depth of the upper compression chord was taken at the cap's quarter point with the assumption that compressive

stresses acted over half of the depth of the entire cap. A finite element analysis could be carried out to validate this assumption; however, the analysis was not provided here to illustrate the point that a FEM is not necessarily needed in cases where the designer has a good understanding of the natural flow of forces. In addition, the transverse tension associated with spread of compressive forces flowing from the pedestal / cap interface to the drilled shafts is not directly shown in the model, but is most certainly present and will be discussed in subsequent paragraphs.

Once the member forces are calculated through classic methods of structural analysis, tension reinforcement can be proportioned and compressive stresses may be checked against limiting stresses.

It should be noted again that resistance factors used in this design example are ones listed in AASHTO LRFD due to the fact the limited structural calculations provided by TxDOT engineers provided only an ultimate load case leaving the exact nature of the loading ambiguous. AASHTO LRFD resistance factors are used exclusively because the ultimate loads were obtained with AASHTO LRFD load factors, and a comparison between codes was desired within this example.

The main tension tie reinforcement is proportioned based on the largest tensile force in the tension chord

$Tmax := viii$

$\phi\_tens\_AASHTO := 0.9$

$$As := \frac{Tmax}{\phi\_tens\_AASHTO \cdot 60 \cdot ksi} \qquad As = 28.15 in^2$$

use # 11 bars

$$num\_bars := \frac{As}{1.56 \cdot in^2} \qquad num\_bars = 18.04$$

Use 18 # 11 bars

The vertical tie reinforcement is proportioned in the same manner; however the ambiguity of the physical dimensions of the smeared node leaves the placement of this reinforcement up to the judgment of the designer.

$T := xii$

$$Av := \frac{T}{\phi\_tens\_AASHTO \cdot 60 \cdot ksi} \qquad Av = 6.81 in^2$$

use # 6 bars

$$num\_bars := \frac{Av}{.44 \cdot in^2 \cdot 2} \qquad num\_bars = 7.74$$

Node B lies almost directly at the midpoint between nodes A and C as shown Figure 2.21, and the placement of these bars should such that their centroid lies at or as close as possible to node B.

Use # 6 bars at 6" O.C entire length

The next step in the process is to check the compressive stresses at the nodal faces and the node-strut interface. In this example there are only two nodes and struts to check since only the geometry of singular nodes can reasonably ascertained. Nodes A, B, C, D, and G in Figure 2.21 are

smeared nodes and are irrelevant in the stress-limit check for two reasons: the geometry of these nodes are not known, and the stresses at these nodes are not critical because they act over a smeared area and are not "bottle-necked" to a concentration of stresses which represent the worst case. Figure 2.22 depicts a singular node at the drilled shaft with the largest reaction.

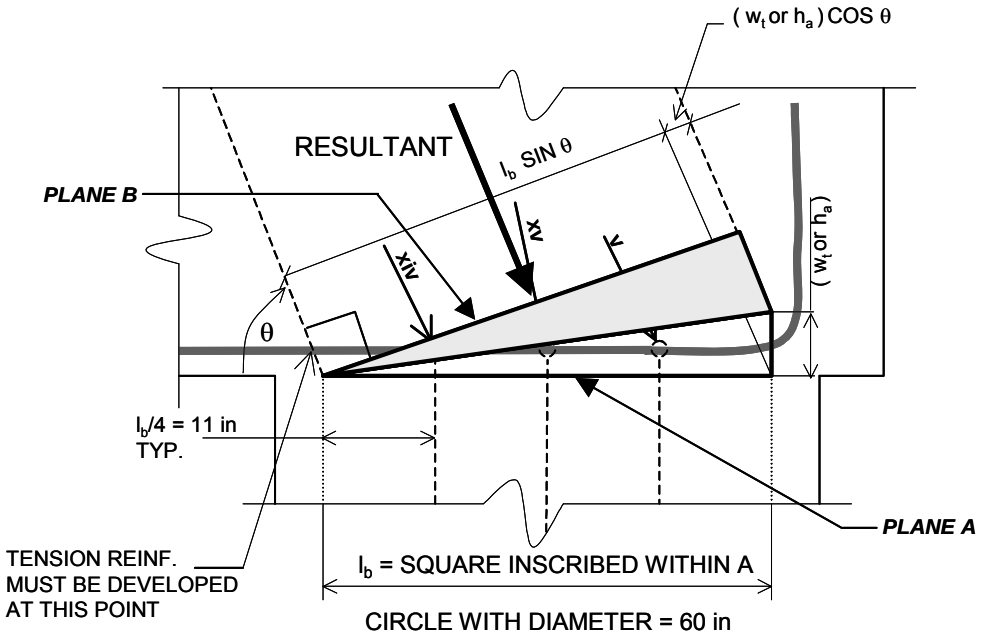

Figure 2.22 Singular Node at Drilled-Shaft

The singular node shown in Figure 2.22 is comprised of three sub-nodes which are the anchoring points of struts xiv, xv, and v as shown in Figure 2.21. The anchoring points were chosen at quarter points of the length of a square inscribed in a circle with radius equal to that of the drilled shaft (60 in.) and placed in the same plane as the longitudnal reinforcement. The resultant force of struts xiv, xv, and v is the force used

to calculate the stress acting on the node-strut interface while the reaction R2 is the force used to calculate the force on the node/drilled-shaft interface. The geometry of the element and main tension reinforcement is such that, the hook takes no part in the formation of the geometry of the node. The radius of the hook lies outside the reaction area so that the struts frame directly into the drilled shaft and not into the bend radius of the hook; therefore, the nodal face dimension perpendicular to main tension reinforcement is given by each code similar to C-C-T nodes anchoring straight reinforcement. The stress on this face need not be calculated. This condition may not always be true and should be analyzed on a case by case basis. The development length of the main tension reinforcement is taken as the distance behind the point at which the centroid of tension reinforcement meets the compression strut at node H in Figure 2.21 and is deemed satisfactory by inspection.

Until this point, the ACI 318-02 and AASHTO LRFD differ only in load and resistance factors. The treatment of limiting stresses of nodes and struts by either code authority marks the divergence of provisions by each.

Applied Stresses

plane A

$$\sigma 2\_A := \frac{R2}{lb^2} \qquad \sigma 2\_A = 1.69\,ksi$$

plane B

resultant_xiv_xv_v := 3417·k

resultant_θ := 63·deg

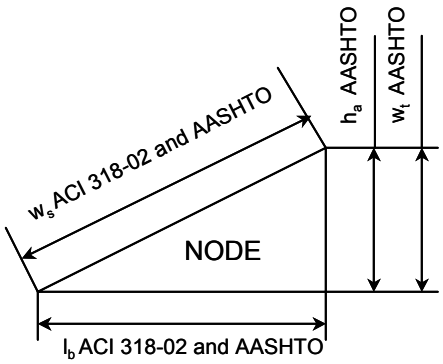

ACI 318-02

wt := 9.4·in

ws_ACI := lb·sin(resultant_θ) + wt·cos(resultant_θ)

$$\sigma 2\_B\_ACI := \frac{resultant\_xiv\_xv\_v}{ws\_ACI \cdot lb}$$

σ2_B_ACI = 1.91 ksi

AASHTO LRFD

ha := 13.8·in

ws_AASHTO := lb·sin(resultant_θ) + ha·cos(resultant_θ)

$$\sigma 2\_B\_AASHTO := \frac{resultant\_xiv\_xv\_v}{ws\_AASHTO \cdot lb}$$

σ2_B_AASHTO = 1.83 ksi

ACI 318-02 and AASHTO LRFD Node and Strut Limiting Stresses

ϕ_comp_AASHTO := 0.7 f'c := 3.6·ksi

for C-C-T nodes

σ2_limit_node_ACI := ϕ_comp_AASHTO·.85·.8·f'c

σ2_limit_node_ACI = 1.71 ksi

σ2_limit_node_AASHTO := ϕ_comp_AASHTO·.75·f'c

σ2_limit_node_AASHTO = 1.89 ksi

Compression Struts

ACI 381-02

$\sigma 2\_limit\_strut\_ACI\_no\_reinf := \phi\_comp\_AASHTO \cdot .85 \cdot .6 \cdot f'c$

$\sigma 2\_limit\_strut\_ACI\_with\_reinf := \phi\_comp\_AASHTO \cdot .85 \cdot .75 \cdot f'c$

$\sigma 2\_limit\_strut\_ACI\_no\_reinf = 1.29\,ksi$

$\sigma 2\_limit\_strut\_ACI\_with\_reinf = 1.61\,ksi$

AASHTO LRFD

assuming $\varepsilon s = .002$

$$\varepsilon_1 := .002 + (.002 + .002)\frac{1}{\tan(resultant\_\theta)^2}$$

$$fcu := \frac{f'c}{0.8 + 170 \cdot \varepsilon_1}$$

$\sigma 2\_limit\_strut\_AASHTO := \phi\_comp\_AASHTO \cdot fcu$

$\sigma 2\_limit\_strut\_AASHTO = 1.91\,ksi$

In a similar manner the stresses at the singular node above reaction 1 are calculated as well as the limiting stresses provide by each code authority.

$resultant\_i\_xi := 1902 \cdot k$

$resultant\_\theta := 48 \cdot deg$

APPLIED STRESSES

plane A

$$\sigma 1\_A := \frac{R1}{lb^2}$$

$\sigma 1\_A = 0.78\,ksi$

plane B

ACI 318-02

$wt := 9.4 \cdot in$

$ws\_ACI := lb \cdot \sin(resultant\_\theta) + wt \cdot \cos(resultant\_\theta)$

$\sigma 1\_B\_ACI := \frac{resultant\_i\_xi}{ws\_ACI \cdot lb}$ $\sigma 1\_B\_ACI = 1.19\,ksi$

AASHTO LRFD

$ha := 13.8 \cdot in$

$ws\_AASHTO := lb \cdot \sin(resultant\_\theta) + ha \cdot \cos(resultant\_\theta)$

$\sigma 1\_B\_AASHTO := \frac{resultant\_i\_xi}{ws\_AASHTO \cdot lb}$ $\sigma 1\_B\_AASHTO = 1.1\,ksi$

ACI 318-02 and AASHTO LRFD Node and Strut Limiting Stresses

for C-C-T nodes the limiting stress remains unchanged

$\sigma 1\_limit\_node\_ACI := \sigma 2\_limit\_node\_ACI$

$\sigma 1\_limit\_node\_AASHTO := \sigma 2\_limit\_node\_AASHTO$

$\sigma 1\_limit\_node\_ACI = 1.71\,ksi$

$\sigma 1\_limit\_node\_AASHTO = 1.89\,ksi$

for compression struts the ACI 318-02
provisions are indepent of the angle with respect to the tension tie and
remains unchanged

$\sigma 1\_limit\_strut\_ACI\_no\_reinf := \sigma 2\_limit\_strut\_ACI\_no\_reinf$

$\sigma 1\_limit\_strut\_ACI\_with\_reinf := \sigma 2\_limit\_strut\_ACI\_with\_reinf$

$\sigma 1\_limit\_strut\_ACI\_no\_reinf = 1.29\,ksi$

$\sigma 1\_limit\_strut\_ACI\_with\_reinf = 1.61\,ksi$

AASHTO LRFD

assuming $\varepsilon s = .002$

$$\varepsilon_1 := .002 + (.002 + .002)\frac{1}{\tan(resultant\_\theta)^2}$$

$$fcu := \frac{f'c}{0.8 + 170\cdot\varepsilon_1}$$

$\sigma 1\_limit\_strut\_AASHTO := \phi\_comp\_AASHTO \cdot fcu$ $\sigma 1\_limit\_strut\_AASHTO = 1.49\,ksi$

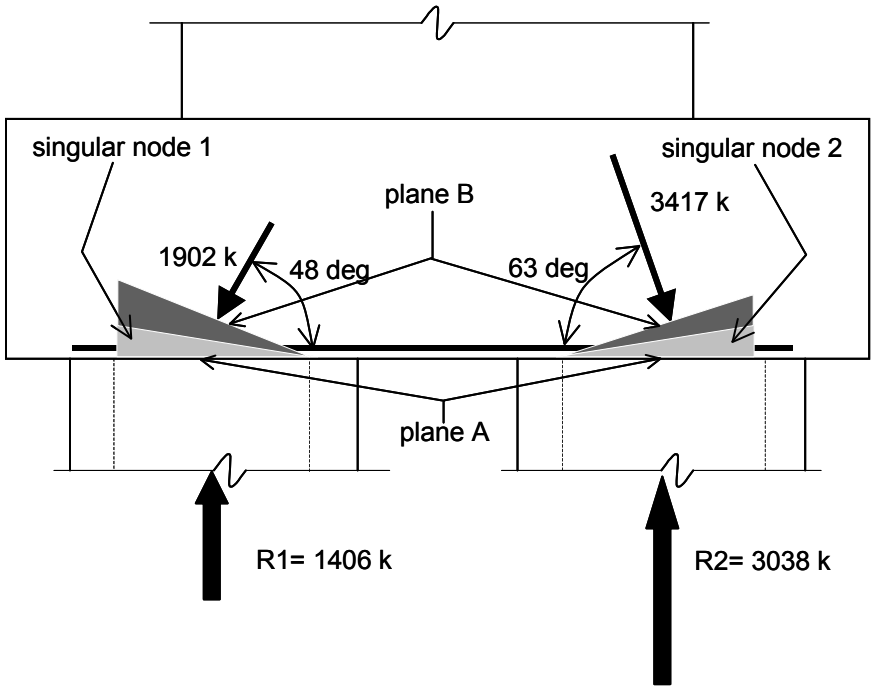

Figure 2.23 Singular Nodes and Resultant Strut Forces

Node Stress Checks

$\sigma 1\_A = 0.78\,ksi$	$\sigma 1\_limit\_node\_ACI = 1.71\,ksi$	$\sigma 1\_limit\_node\_AASHTO = 1.89\,ksi$
$\sigma 1\_B\_ACI = 1.19\,ksi$	$\sigma 1\_limit\_node\_ACI = 1.71\,ksi$	
$\sigma 1\_B\_AASHTO = 1.1\,ksi$	$\sigma 1\_limit\_node\_AASHTO = 1.89\,ksi$	
$\sigma 2\_A = 1.69\,ksi$	$\sigma 2\_limit\_node\_ACI = 1.71\,ksi$	$\sigma 2\_limit\_node\_AASHTO = 1.89\,ksi$
$\sigma 2\_B\_ACI = 1.91\,ksi$	$\sigma 2\_limit\_node\_ACI = 1.71\,ksi$ **NO GOOD**	
$\sigma 2\_B\_AASHTO = 1.83\,ksi$	$\sigma 2\_limit\_node\_AASHTO = 1.89\,ksi$	

Strut Stress Checks

$\sigma 1\_B\_ACI = 1.19\,ksi$	$\sigma 1\_limit\_strut\_ACI\_no\_reinf = 1.29\,ksi$		
$\sigma 1\_B\_AASHTO = 1.1\,ksi$	$\sigma 1\_limit\_strut\_AASHTO = 1.49\,ksi$		
$\sigma 2\_B\_ACI = 1.91\,ksi$	$\sigma 2\_limit\_strut\_ACI\_no\_reinf = 1.29\,ksi$	$\sigma 2\_limit\_strut\_ACI\_with\_reinf = 1.61\,ksi$	**NO GOOD**
$\sigma 2\_B\_AASHTO = 1.83\,ksi$	$\sigma 2\_limit\_strut\_AASHTO = 1.91\,ksi$		

In summary the stresses acting on the node and adjacent strut face at node 2 in Figure 2.23 exceed the limiting stresses provided by the ACI 318-02 but fall within the limitation of the AASHTO LRFD provisions. To examine the differences of each code in regard to the acceptance level of stresses applied to struts, a closer look into the reinforcement of struts is required.

The level of stress applied to the strut-node face of singular node 2 would still exceed the limiting compressive stress provided by ACI 318-02 even with appropriate reinforcement that is sufficient to confine the inherent spreading of compressive stresses at the mid-height of the bottle-shaped strut. This reinforce quantity is given by ACI A.3.3.1.

$$\sum_{i=1}^{n} \frac{A_{si}}{bs_i} \cdot \sin(\gamma_i) \geq .003$$

Equation A-4

with the additional commentary of RA.3.3:

Often, the confinement reinforcement given in A.3.3 is difficult to place in three-dimensional structures such as pile caps. If this reinforcement is not provided, the value of f_{cu} given in A.3.2.2 (b) (βs = 0.6 instead of βs = 0.75) ***is used.***

The commentary means that reinforcement placed in typical US construction practices, about the side faces as stirrups and skin reinforcement, may not be effective in confining the strut, and therefore the strut should be considered unconfined. To understand the

reinforcement needed to confine struts in two or three-dimensional structures refer to Figure 2.24 and following discussion.

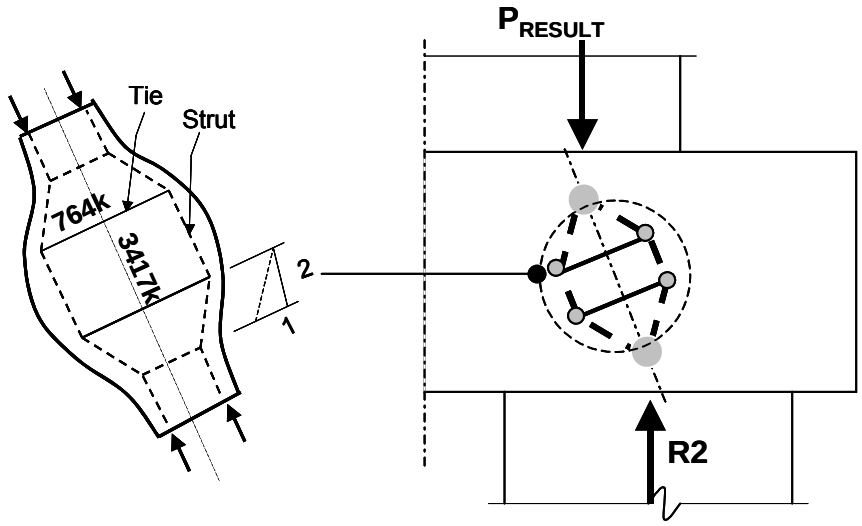

Figure 2.24 Modeling Dispersed Compression Field with 2:1 Bottle-Shaped Strut

To supply the reinforcement required to confine this strut according to ACI 318-02 the designer may employ equation A-4 or proportion steel directly based on the 2:1 model which always results in tension = 0.447x compression. The following sample calculation displays how the quantity of confining steel may be computed using equation A-4 or the 2:1 model for spread of compressive stresses.

using equation A-4

try # 6 bars at 3" OC each way and take b = width of the drilled shaft

$\theta := 63deg$ $b := 60 \cdot in$

$\gamma_1 := 63 \cdot deg$ $\gamma_2 := 90deg - 63 \cdot deg$

$As_1 := .44 \cdot in^2$ $As_2 := .44 \cdot in^2$

$s_2 := 3 \cdot in$ $s_1 := 3 \cdot in$

$$\sum_{i=1}^{2} \frac{As_i}{b \cdot s_i} \cdot \sin(\gamma_i) = 0.0033$$

use # 6 bars @ 3" OC each way placed down the centerline of the cap

using 2:1 model

$T := 0.447 \cdot 3417 \cdot k$ $T = 1527.4\,k$

determine θ with respect to horizontal of tension force

$\theta := 27 \cdot deg$

use # 6 bars $As := .44 \cdot in^2$

$height\_cap := 60 \cdot in$

$$w\_strut := \frac{height\_cap}{\tan(63 \cdot deg)}$$

$$num\_bars\_y := \frac{T \cdot \sin(\theta)}{\phi\_tens\_AASHTO \cdot 60 \cdot ksi \cdot As} \qquad num\_bars\_y = 29.18$$

$$num\_bars\_x := \frac{T \cdot \cos(\theta)}{\phi\_tens\_AASHTO \cdot 60 \cdot ksi \cdot As} \qquad num\_bars\_x = 57.28$$

$$sy := \frac{w\_strut}{num\_bars\_y} \qquad sy = 1.05\,in$$

$$sx := \frac{height\_cap}{num\_bars\_x} \qquad sx = 1.05\,in$$

use # 6 bars at 1" OC each way
placed at the centerline of the cap

The calculations above show the large discrepancy in the current state of practice in the treatment of acceptance criteria with the two major codes governing the design of concrete structures within North America. AASHTO LRFD provisions permit the stress level for this strut, which is unacceptable by ACI 318-02 standards with the added confining reinforcement consisting of # 6 bars at 3 in. on center each way placed down the centerline of the cap using equation A-4 or # 6 bars at 1”on center using the 2:1 model. Adhering to commentary RA3.3 would mean that the confining steel calculated above must be placed at the centerline of the strut in order for it to be effective.

While not in the scope of this experimental work, it should be noted that the acceptance criteria for C-C-T nodes provided by each code are conservative as proven by Thompson [47]. The C-C-T singular node 2

exceeded the stress limit provided by ACI; however, this node as well as node 1 is bi-axially confined as with any node whose bearing dimension is smaller than that of the surrounding concrete.

Although every stress level was acceptable by AASHTO LRFD standards, the same stress level exceeded ACI 318-02 standards leaving the designer unsure and uncomfortable about a final design acceptable by only one standard. It would be desirable to have agreement on the same method and achieve a consistent design standard regardless of the method being used in bridge or building structures. Finally the strut-and-tie method produced an equivalent amount of main tension reinforcement as that originally calculated by TxDOT engineers using an allowable stress criterion with pure bending theory. The vertical tension reinforcement calculated by the strut-and tie method is twice that provided by TxDOT engineers who discerned that shear is not a factor; however the tie reinforcement was placed as good practice. The strut-and-tie model shows shear forced at the lightly loaded drilled-shaft and the reinforcement proportioned for shear at that location is placed the entire length as good practice.

Figure 2.25 shows the comparison of amounts of reinforcement required by the strut-and-tie model shown in Figure 2.21 in the two orthogonal dimensions of the drilled-shaft cap omitting skin reinforcement, temperature and shrinkage reinforcement, and "feel good reinforcement" as called for by original TxDOT calculations.

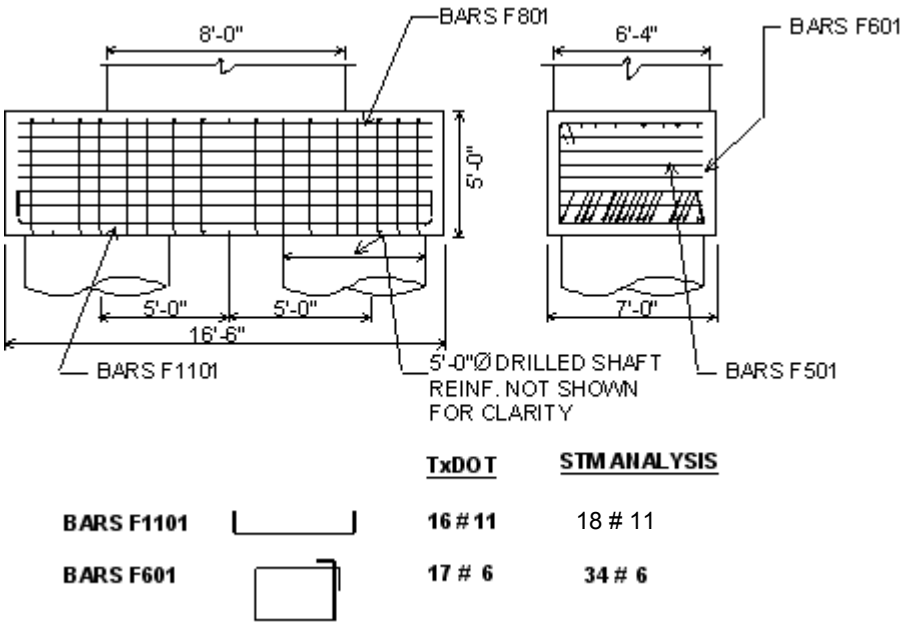

Figure 2.25 Comparison of Drilled-Shaft Cap Reinforcement Resulting from TxDOT and STM Analyses

3.0 EXPERIMENTAL PROGRAM

3.1 GENERAL

The experimental program consisted of a series of laboratory experiments designed to investigate the behavior of bottle-shaped struts. Twenty-eight tests were conducted in three basic series. The design of each series was a progressive process in which data from the first series was analyzed to determine appropriate parameters and to improve the next series in order to isolate the parameters influencing strut behavior.

3.2 TEST SET-UP

The test set-up is analogous to split-cylinder testing in which monotonic load is applied at an increasing rate to a specimen whose geometry and orientation allow for the dispersion of compression and associated transverse tension to develop within the boundary of the specimen. In this case, load was applied by a universal testing machine (UTM) to square or rectangular, unreinforced, and reinforced concrete panels through steel bearing plates. The dimensions of the bearing plates were significantly less than the surface area of concrete at the loaded ends. The basic test set-up is shown in Figure 3.1. To ensure that the force from the loading head of the UTM was applied to the concrete surface uniformly; hydrostone was placed at the concrete-steel plate interface, as well as, a spherical head placed at the plate-loading head interface. The specimens were plumbed before testing to ensure alignment. Strain measurements were collected through series of electric strain gauges applied to the reinforcement within the specimens and the

concrete surface of the specimens. (Instrumentation will be discussed in detail in subsequent sections) The strain measurements were recorded through data-acquisition hardware and software available at the Ferguson Structural Engineering Laboratory at the University of Texas at Austin. Load was recorded through the same data-acquisition systems in parallel with internal load cells within the universal testing machine. Displacement recordings were not taken in light of Sanders' [44] and Wollman's [51] experimentation in which they concluded that isolated specimens such as these failed in a non-ductile manner providing little or no useful load-displacement data.

Figure 3.1 Typical Test Set-Up

3.3 SERIES 1 SPECIMENS

3.3.1 General

The first series of specimens consisted of 6 specimens from two batches of concrete. This series consisted of 3 ft. by 3 ft. by 4 in. thick reinforced and unreinforced concrete panels, and the main foci of this series was to achieve an optimal system of instrumentation, and to substantiate the choice of the overall specimen geometry. Therefore, different arrangements of instrumentation were used. The patterns of reinforcement varied as well. All specimens were tested using 4 in by 12 in. by 2 in. bearing plates defining the nodal area, and reinforced with orthogonal mats of reinforcement consisting of #3 bars. From this point forward specimens will be designated thus: S#-# with S# referring to series 1, 2 or 3, and the last number represents the order tested within the series.

3.3.2 Specimen S1-1

3.3.2.1 Instrumentation

At the outset of the experimental program, it was the original goal of the research team to obtain the principle stresses at points evenly dividing one quadrant of a specimen. For this reason a specimen S1-1 was fabricated to include embedded strain rosettes. These rosettes were fabricated from thin gauge sheet metal having three axes at 0 deg., 45 deg., and 90 deg. The anchoring points were established at the end of each axis by brazing a sheet-metal screw to the rosette through a pre-fabricated hole. The rosettes were then gauged with electronic strain

gauges placed at the center of each leg forming the three axes and debonded from the concrete by placing HVAC foil-tape around each axis leaving only the anchorage points exposed. 6 in. and 2 in. axis lengths were investigated. The rosettes tied to the reinforcing cage are shown in Figure 3.2.

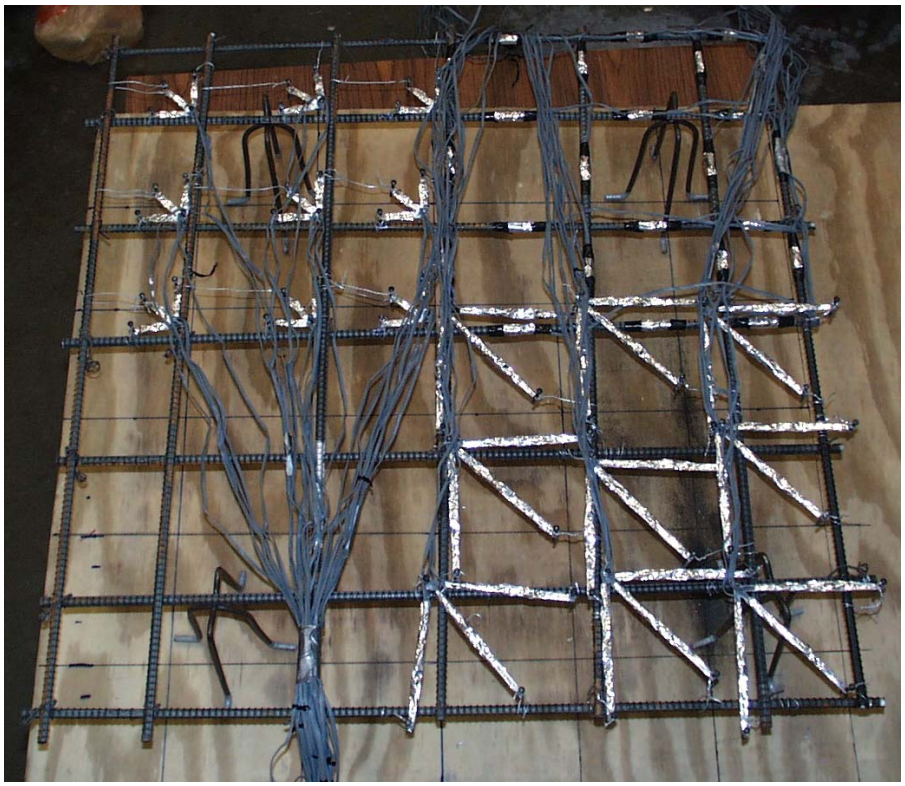

Figure 3.2 Embedded Strain Rosettes.

The reinforcing cage was also instrumented with electronic strain gauges at one quadrant of the specimen on every reinforcing bar at 3 in. from the form face and 6 in. on center until the specimen's centerline was reached.

3.3.2.2 S1-1 Behavior

The specimen behavior is briefly described here and in the following sections, because as stated previously, the experimental program was an evolving process in which each series of specimen were designed based on knowledge compounding from earlier testing.

At first appearance, S1-1 seemed to have failed within the nodal region, such a failure was undesirable since the behavior of bottle-shaped struts was anticipated and thought to have failures typified by large cracks at the specimen centerline. Figure 3.3 shows the failure mode of specimen S1-1 which can be visually described by slight spalling of the nodal region and one hairline crack down the centerline of the specimen.

Figure 3.3 Failure Mode of Specimen S1-1

When the data gathered from the embedded rosettes was analyzed, the accuracy of the results to capture the specimen's behavior was questionable and inconsistent. The research team subsequently abandoned further use of the embedded rosette.

3.3.3 Specimens S1-2, S1-3, S1-4, S1-5, S1-6

3.3.3.1 Specimen S1-2 Instrumentation

Adhering to the idea of obtaining the principle stress at points evenly dividing one quadrant of a specimen; embedded rosettes were replaced with surface rosettes for this specimen. Two styles of surface rosettes were investigated with specimen S1-2: The first style was a prefabricated surface rosette that had no lead wires requiring that wire be soldered to the gauge before testing could take place which proved to be a lengthy and unreliable process. The second style of rosette consisted of 3 – 60mm. long surface gauges (referred hereafter as 2 in. surface gauges) applied directly over each other at three axes of 0 deg., 45 deg., and 90 deg. The two styles of rosettes were oriented on specimens S1-2 as shown in Figure 3.4 with the hope of capturing the 2:1 spread of compression stresses as reported by Burdet [17] and to assess what type of rosette best captured this behavior. Single surface gauges were also placed on the centerline transverse axis in order to integrate the strains over the area of the specimen and compare that calculation with the load applied. If these values agreed reasonably well, an evaluation of the adequacy surface gauges in capturing the behavior of the specimen in compression could be made. Figure 3.4 also demonstrates how surface gauges were applied to each specimen.

3.3.3.2 Specimen S1-2 Behavior

Specimen S1-2 was unreinforced to ensure that reinforcement did not restrain the elastic 2:1 spread of compression and therefore no comparisons could be made from strain readings taken from

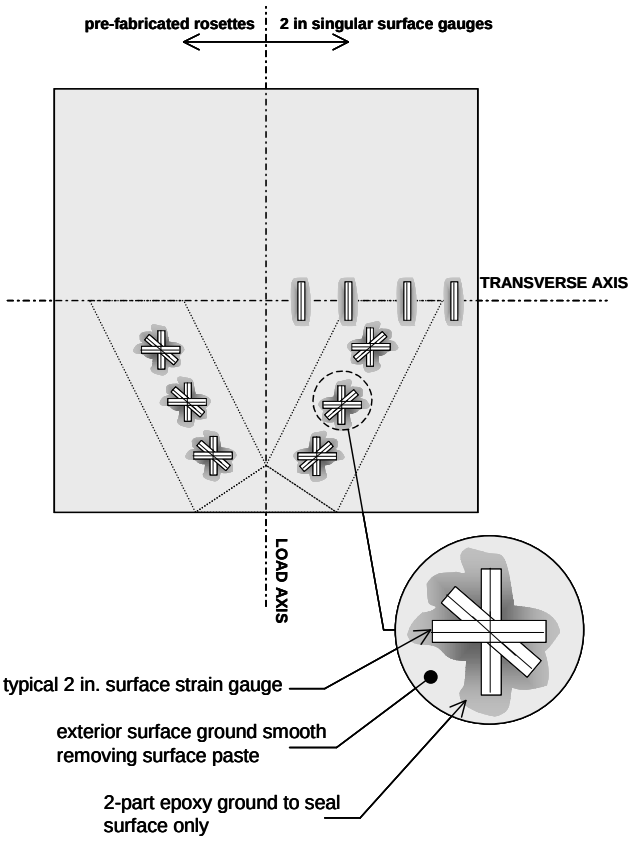

Figure 3.4 Specimen S1-2 Surface Gauge Instrumentation

reinforcement gauges in specimen S1-1. The pre-fabricated and built-up rosettes compared well with each other and did capture the principle strains at angles ranging from 22 deg. to 27 deg. In light of these finding built-up rosettes were chosen for placement on the surface of specimens S2-2, S2-3, S2-4, and S2-5 due to ease of application. Furthermore, the strain gauges placed at the transverse axis captured the load when

stresses were integrated over the area using the constitutive relationship developed by Hognestad. The specimen failed at a lower load than specimen S1-1 as expected with a specimen containing no reinforcement.

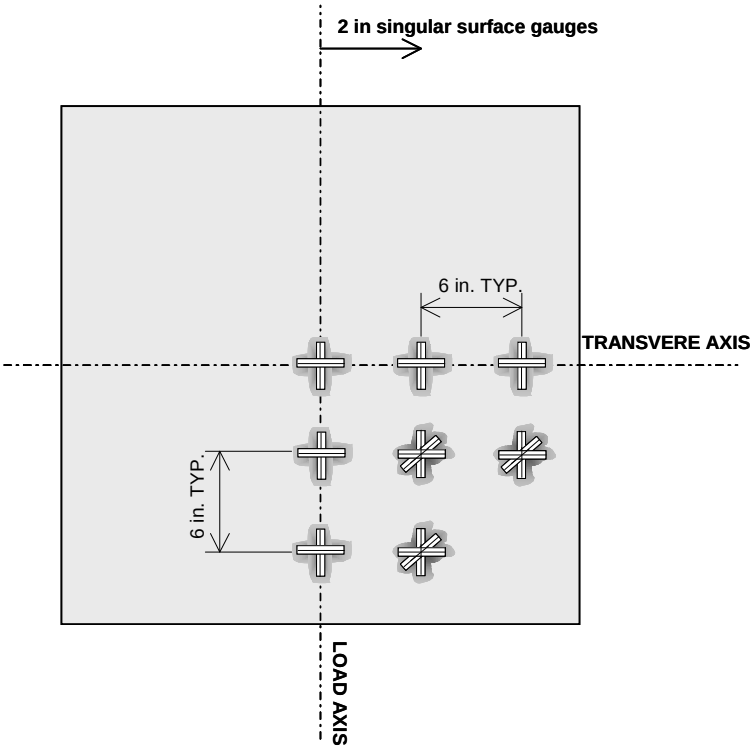

Figure 3.5 Surface Gauge Instrumentation for S1-3 through S1-6

3.3.3.3 Specimens S1-3, S1-4, S1-5, S1-6 Instrumentation

These specimens were cast with the same concrete as specimen S1-2; however, instrumentation of the specimens was restrained until results from testing specimen S1-2 became available. Once data from specimen S1-2 was analyzed, surface instrumentation was chosen and shown in Figure 3.5. Rosettes were not used at the centerline of the specimens, because it was assumed that principle stresses acted in the

orthogonal directions of the specimen at theses locations. All surface gauges were applied as shown in Figure 3.4, and only built-up rosettes consisting of 2 in surface gauges were used.

Specimens S1-3 and S1-4 contained only the instrumentation shown in Figure 3.5. Specimens S1-5 and S1-6 contained orthogonal mats of reinforcement and were instrumented with reinforcement gauges at the locations were the vertical and horizontal bars met in one quadrant of the specimen.

3.3.3.4 Specimens S1-3, S1-4 and S1-5 Special Reinforcing

In order to investigate the role of the node at the point where load was applied in these specimens and to force failure away from the node; special confining reinforcement was placed in specimens S1-3, S1-4, and S1-5. The confining reinforcement consisted of either 2 or 3 closed ties encompassing 6 vertical bars welded to a bearing plate as seen in Figure 3.6 shown in the form before casting.

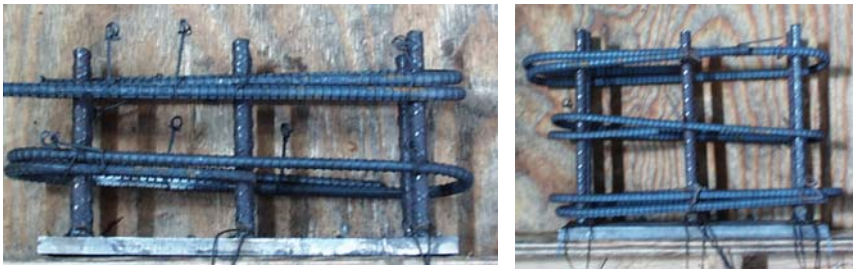

A) Confining Reinforcement at Nodes for Specimens S1-3, S1-6

B) Confining Reinforcement at Nodes for Specimen S1-4

Figure 3.6 Confining Reinforcement for Nodes

3.3.3.5 Specimens S1-3 through S1-6 Behavior

Specimens S1-3 and S1-4 were identical to specimen S-1 having no orthogonal reinforcement; however as stated above S1-3 and S1-4 had different levels of confining reinforcement at the node location. Specimen S1-5 was identical to specimen S1-1 in regard to orthogonal reinforcement, but also had the confining reinforcement at the node locations shown in Figure 3.6 A). The specimens whose nodes were confined displayed no particular behavior in respect to cracking patterns or modes of failure different from specimens whose nodes were unconfined other than the ultimate loads when normalized with respect to the differing concrete strengths were around two times that of the unconfined specimens. Furthermore, when removing crushed concrete around the node of specimens S1-6 a clearly defined area of the node could be seen in which the mode of failure was strut crushing at the node-strut interface. These two observations determined that further confinement of the node was not necessary to achieve the desired behavior of bottle-shaped struts.

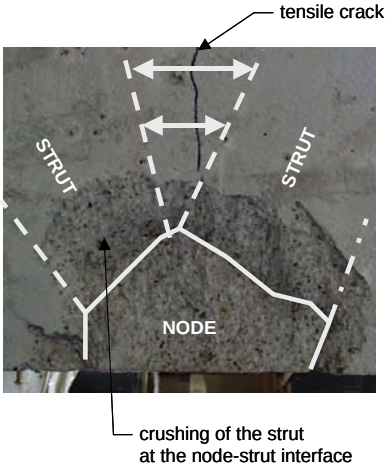

Figure 3.7 Crushing of the Strut at the Node-Strut Interface, S1-6

A detailed description of the specimen dimensions, bearing plate dimensions, amount of reinforcement, atypical loading conditions (if any), and material properties for this series of specimens as well as every other specimen tested within the experimental program can be seen in Figures 3.12 through 3.15 and Tables 3.1 through 3.3 at the end of this chapter.

3.4 SERIES 2 SPECIMENS

3.4.1 General

Confident that the overall specimen geometry was sufficient to study the behavior of bottle-shaped struts based on the observations seen in the first series of specimens; Series 2 specimens were designed as 3 ft. by 3 ft by 6 in thick concrete panels with no nodal confinement with a particular regime of reinforcement and instrumentation. All specimens were cast together, yet 3 cylinders were tested each day testing occurred in order to have specific values of concrete strength for each specimen. All specimens were tested using 6 in. by 12 in. by 2 in. bearing plates defining the nodal area and reinforced with #2 or # 3 reinforcing bars.

3.4.2 Series 2 Instrumentation

The surface rosettes were abandoned in the Series 2 specimens because the data provided from the Series 1 tests was not valuable enough to warrant the time and effort spent in the application of these gauges. Rather, five surface gauges were applied to each specimen at the transverse axis to one side of the specimen shown in Figure 3.8 A. The exception to this pattern occurred wherever a reinforcing bar parallel to the load axis was present, in which case, a surface gauge was located

at the transverse axis at the point of the reinforcing bar beneath as illustrated in Figure 3.8 B. This measure was taken to compare the strain measurements recorded on the concrete surface with the strain measurements taken internally.

Strain gauges were also placed on reinforcement within the specimens at the point in which the reinforcement crossed the load axis or transverse axis. This instrumentation was usually restricted to reinforcement placed to one side of the load axis dividing the specimen in half; however, as with the surface gauges, reinforcement gauges were occasionally placed symmetrically about the load axis to verify the distribution of stress across the specimen.

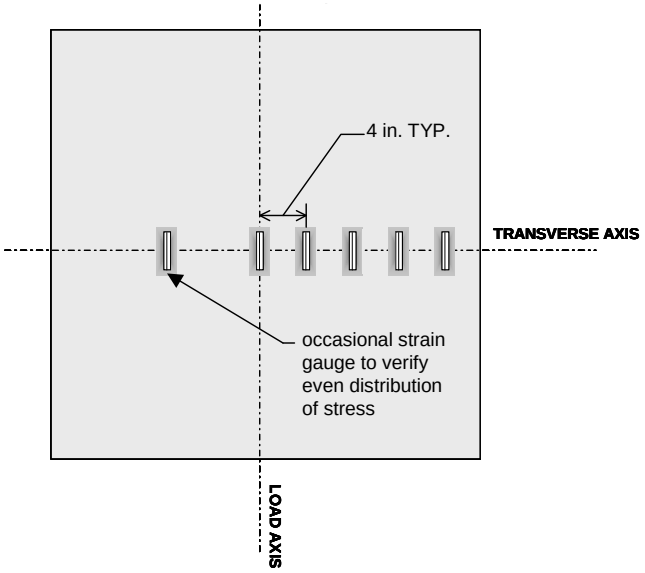

A) Typical Series 2 Specimen Surface Gauge Location

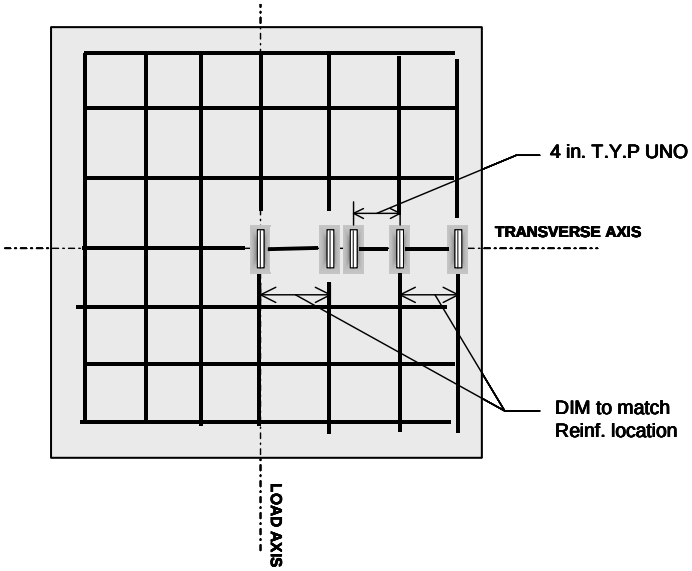

B) Series 2 Specimen Surface Exception

Figure 3.8 Series 2 Surface Gauge Instrumentation

3.4.3 Series 2 Reinforcement

The only provisions available for the reinforcement of bottle-shaped struts is given in ACI 318-02 A.3.3.1 (presented in 1.2.3 of this thesis) or reinforcement proportioned using the 2:1 model (also presented in that section). In order to investigate the adequacy of the relevant ACI provisions, specimens included reinforcement ratios on the order of 0.5, 1.0, and 1.5 times the amount reinforcement given in ACI equation A-4 which is presented as a reinforcement ratio. To satisfy these ratios U.S. #3 bars were used as well as #2 (6mm) bars. These bars were typically placed in orthogonal mats symmetric about the load axis and transverse axis and at mid-depth of the thickness dimension. Other variables regarding the reinforcement of the specimens included the orientation of the orthogonal mats with respect to the load axis of the specimen to simulate struts crossing reinforcement at an angle, as well as, the distribution of reinforcement (lumped versus evenly distributed). The variables involved in the reinforcement of the specimens in Series 2 are shown graphically in Figure 3.9.

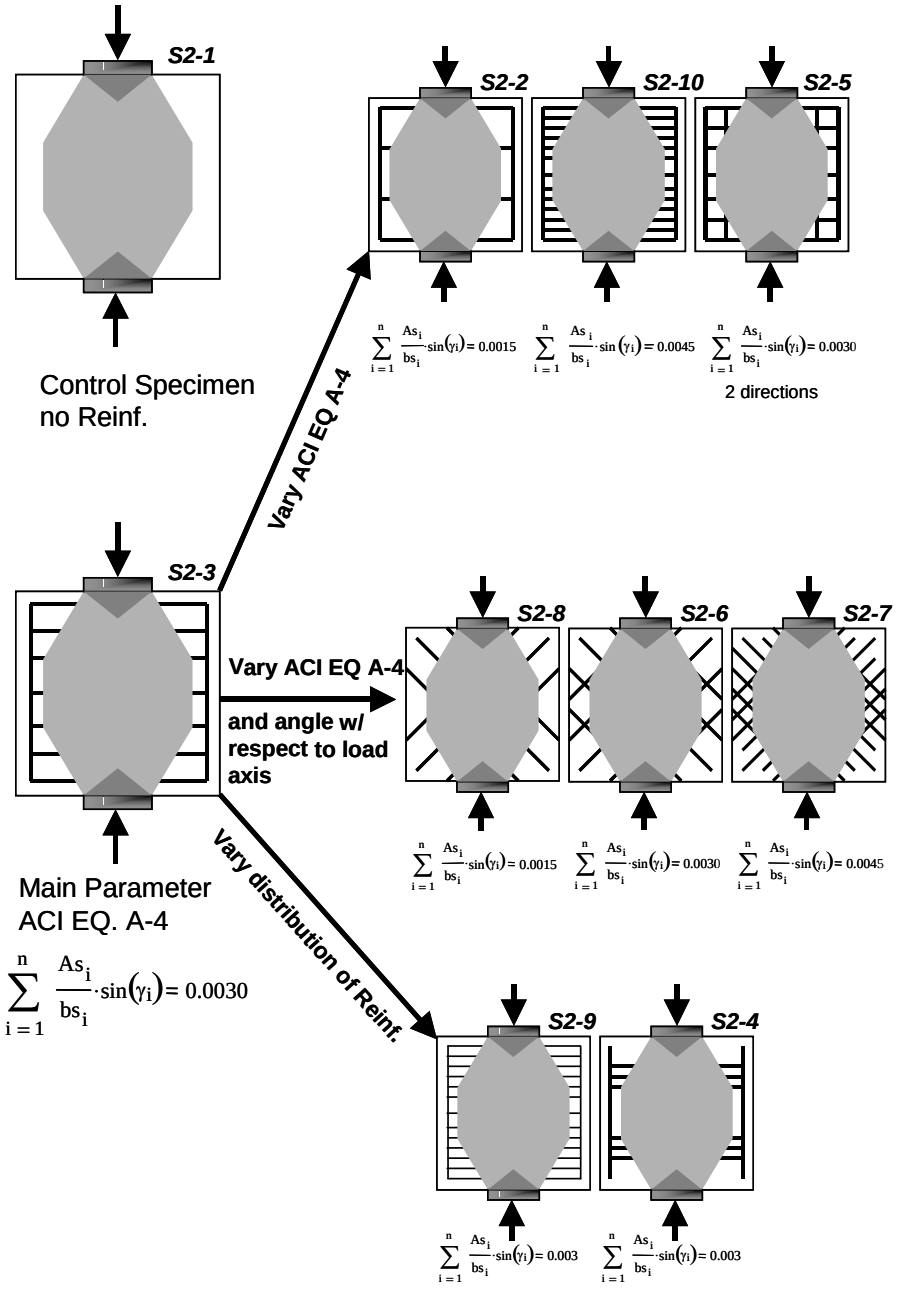

Figure 3.9 Variables Involved in the Reinforcement of Series 2 Specimens

3.4.4 Behavior of Series 2 Specimens

Unfortunately, the data gathered in testing specimens S2-1 and S2-5 were lost and therefore the specimens were repeated in series 3. Adding specimen S1-2 and normalizing the ultimate load carried by that specimen with respect to the concrete strength and bearing plate dimension provided a comparison of the different reinforcing schemes displayed in Figure 3.9. Every specimen tested exhibited relatively similar behaviors with a vertical crack forming at the centerline of the specimen and failing in a brittle manner with concrete crushing at the node-strut interface. A comparison of the ultimate normalized loads carried by the specimens in series 2 along with specimen S1-2, shown in Figure 3.10, proved that the various reinforcing schemes did little to affect the ultimate capacity.

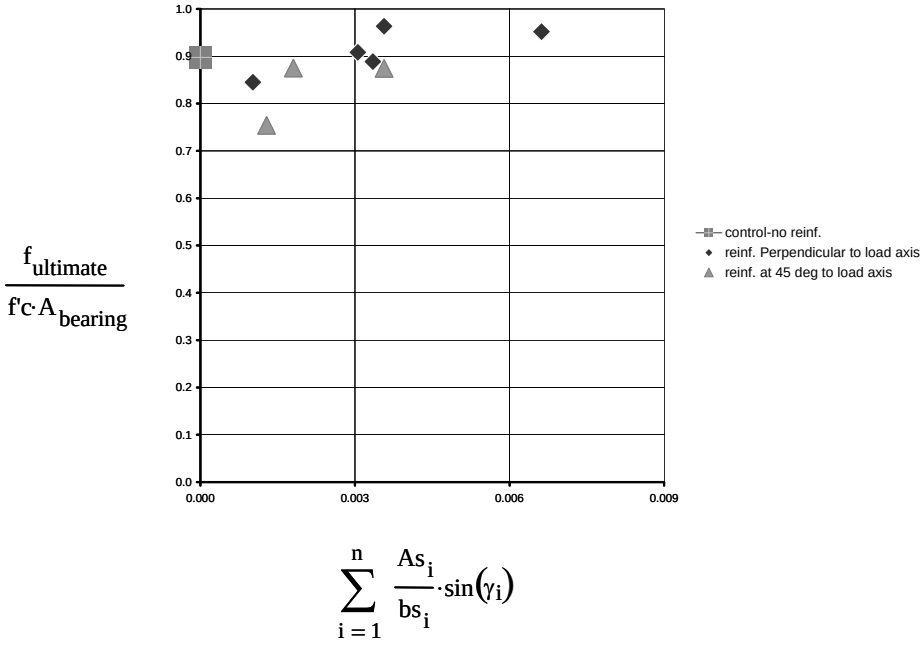

Figure 3.10 Effect of Reinforcing Schemes in Series 2

3.5 SERIES 3 SPECIMENS

3.5.1 General

The effects of various reinforcement distributions shown in Figure 3.10 proved that amount, distribution, and reinforcement angle with respect to the load axis of the specimen had little effect on the overall behavior. For this reason series 3 specimens were designed to vary the boundary conditions of the basic specimen in order to produce more dramatic changes to the overall behavior. Two specimens, S3-1 and S3-5, were replicates of specimens S2-1 and S2-5 because the data gathered in testing these two specimens were lost as mentioned previously.

3.5.2 Series 3 Instrumentation

The instrumentation regime presented in 3.4.2 was used in the Series 3 specimens because it provided the data needed to understand the behavior of specimens and allowed direct comparisons between Series 1 and 2.

3.5.3 Reinforcement Patterns Used in Series 3 Specimens

Generally, the specimens within series 3 were reinforced with an amount of reinforcement stipulated by ACI equation A-4; however specimens S3-2 and S3-6 were reinforced differently with specimen S3-2 testing the practical minimum amount reinforcement for these specimens containing only one #3 bar located at the transverse axis, and specimen S3-6 reinforced with 4 # 3's oriented parallel to the load axis under the bearing surface, and 3 # 3 bars at third points oriented parallel to the transverse axis. Specimen S3-7 contained lumped reinforcement in the

same quantity as S2-4 but spaced farther apart from the specimen's transverse axis. S3-8 reinforcement was placed in an orthogonal mat at angles of 30 deg and 60 deg relative to the load axis of the specimen. The reinforcement of specimens S3-9 and S3-10 was placed near the form face and finished face in two mats (previous specimens all had reinforcement placed at mid-depth of the 4 or 6 in. dimension). The reinforcement of specimens S3-3, S3-4, S3-11, S3-12 all had the same amount of reinforcement as S2-3, but varied in boundary conditions as discussed in the following section. These reinforcing schemes represented variables not investigated in the series 2 specimens. dimension). These reinforcing schemes represented variables not investigated in the series 2 specimens

3.5.4 Series 3 Boundary Conditions

As stated previously, the boundary conditions varied within this series with S3-3, S3-4, and S3-7 through S3-12 having different boundary conditions than the typical specimen of series 2. The standard bearing plate dimensions of 6 in. by 12 in. by 2 in. in series 2 was changed to 6 in by 6 in by 2 in is testing specimens S3-4, S3-7, and S3-8. The standard bearing plate configuration of the series 2 specimen was changed to allow shear deformations and eliminate horizontal friction in specimen S3-3 as shown in Figure 3.11. Specimens S3-9 and S3-10 were formed to have a thickness of 10 in. rather than the standard 6 in. and were tested using 4 in by 12 in. by 2 in. bearing plates placed at the center of the plan area of the specimens. Specimens S3-11 and S3-12 were cast having the standard height of 36 in. and depth of 6 in. but the width of these

specimens was changed to 60 in, and S3-11 was tested using the standard bearing plate dimensions while specimenS3-12 was tested using a larger bearing plate having the dimensions of 6 in. by 16 in. by 3 in. The specific details of these specimens along with every specimen tested will be summarized in 3.6.

3.5.5 Behavior of Series 3 Specimens

The qualitative behavior of the specimens tested in series 3 was similar to all other specimens tested with the failure mode beginning as a hairline crack parallel to the load axis of the specimen and gradually widening until an ultimate non-ductile failure categorized by crushing of the concrete at the node-strut interface prevented any further load being sustained by the specimen.

The data gathered from the electronic instrumentation placed within this series as well as all other data gathered from all the previous specimens, when analyzed, proved that no further testing was required and ended the experimental program after series 3 testing. The complete data gathered from all specimens will be presented in Chapter 4 and analyzed with commentary in Chapter 5.

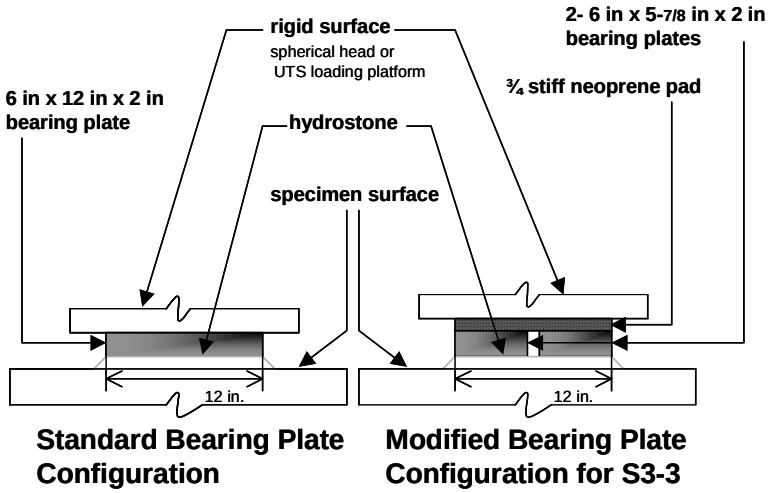

Figure 3.11 Modified Bearing Plate Configuration

3.6 SPECIMEN SUMMARY

A complete summary of the contents and configuration of every specimen tested is described in Table 3.1. Figure 3.12 illustrates a typical specimen elevation for use with Table 3.1. Figure 3.13, Figure 3.14, and Figure 3.15 following Table 3.1 further illustrate specific reinforcement placement, non-standard conditions, or further explanation of the material presented in that table. The material properties used in the fabrication of each specimen include the yield strain and the modulus of elasticity for the reinforcing steel listed in Table 3.2, the tensile strength of concrete listed in Table 3.3, and the compressive strength of concrete is listed in Table 3.1. The compressive strength of concrete was tested each day a specimen was tested while the tensile strength of concrete was tested after the complete testing of one series of specimen.

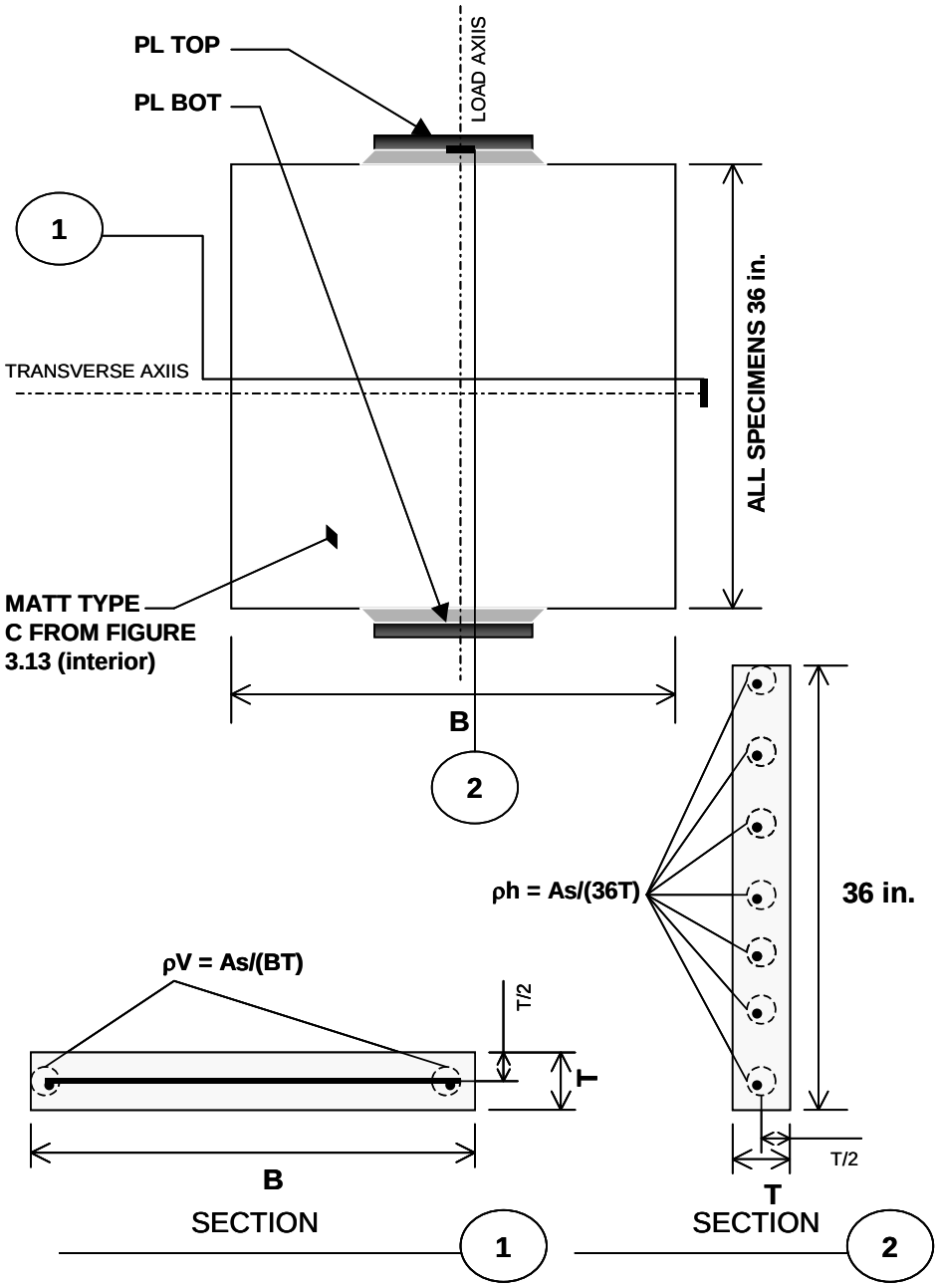

Figure 3.12 Typical Specimen Elevation for Use with Table 3.1

Table 3.1 Summary of Specimens

Designation	B (in)	T (in)	PL Top (in)	PL Bot. (in)	f`c (ksi)	reinforcement		ρh_{10^3}	ρv_{10^3}	mat type[2]	node confined[3]
						Size (#)	Yield[1] (ksi)				
S1-1	36	4	4x12x2	4x12x2	3.23	3	63	5.35	5.35	A	-
S1-2	36	4	4x12x2	4x12x2	3.83	-	-	0	0	-	-
S1-3	36	4	4x12x2	4x12x2	3.91	-	63	0	0	-	A
S1-4	36	4	4x12x2	4x12x2	3.91	-	-	0	0	-	B
S1-5	36	4	4x12x2	4x12x2	3.91	3	-	5.35	5.35	A	A
S1-6	36	4	4x12x2	4x12x2	3.91	3	63	3.06	3.06	B	-
S2-1[4]	36	6	6x12x2	6x12x2	5.29	-	-	0	0	-	-
S2-2	36	6	-	-	5.29	-	-	2.04	1.02	B	-
S2-3	36	6	6x12x2	6x12x2	5.29	3	63	2.04	1.02	C	-
S2-4	36	6	6x12x2	6x12x2	5.29	3	63	3.06	1.02	D	-
S2-5[4]	36	6	-	-	5.29	3	63	3.56	3.56	A	-
S2-6	36	6	6x12x2	6x12x2	5.29	3	63	2.52	2.52	E	-
S2-7	36	6	6x12x2	6x12x2	5.49	2[5]	80	2.01	2.01	E	-
S2-8	36	6	6x12x2	6x12x2	5.49	2[5]	80	1.43	1.43	F	-
S2-9	36	6	6x12x2	6x12x2	5.50	2[5]	80	2.64	0.40	G	-

Table 3.1 Continued Summary of Specimens

Designation	B (in)	T (in)	PL Top (in)	PL Bot. (in)	f`c (ksi)	reinforcement		ρh_{10^3}	ρv_{10^3}	mat type[2]	node confined[3]
						Size (#)	Yield[1] (ksi)				
S2-10	36	6	6x12x2	6x12x2	5.50	3	63	6.62	1.02	G	-
S3-1	36	6	6x12x2	6x12x2	4.20	-	-	0	0	-	-
S3-2	36	6	6x12x2	6x12x2	4.20	3	63	0.51	0	H	-
S3-3	36	6	2-6x6x2[6]	2-6x6x2[6]	4.30	3	63	3.56	1.02	C	-
S3-4[7]	36	6	6x6x2	2-6x6x2	4.30	3	63	3.56	1.02	C	-
S3-5	36	6	6x12x2	6x12x2	4.30	3	63	3.56	3.56	A	-
S3-6	36	6	6x12x2	6x12x2	4.35	3	63	1.53	2.04	I	-
S3-7	36	6	6x6x2	6x12x2	4.35	3	63	3.06	1.02	J	-
S3-8	36	6	6x6x2	6x6x2	4.35	3	63	3.48	3.48		-
S3-9[8]	36	10	4x12x2	4x12x2	4.35	3	63	3.06	1.22	-	X
S3-10[8]	36	10	4x12x2	4x12x2	4.35	2[5]/3	80/63	3.06	1.22	-	X
S3-11	60	6	6x16x2	6x16x2	4.35	3	63	3.56	0.61	L	-
S3-12	60	6	6x12x3	6x12x3	4.35	3	63	3.56	0.61	L	-

[1] Nominal yield stress
[2] Letter corresponds to mat types in Figure 3.13
[3] A or B corresponds to Figure 3.6 X indicates node confined by surrounding concrete
[4] Data lost during testing
[5] #2 bars are 6mm diameter Mexican manufactured bars
[6] Modified bearing plate configuration seen in Figure 3.11
[7] Refer to Figure 3.14for testing conditions
[8] Refer to Figure 3.15for complete details of specimen

Table 3.2 Reinforcing Steel Properties

Bar Size	E_s (ksi)[1]	ε_y[1]
#2	25.8×10^3	0.0031
#3	23.7×10^3	0.0027

[1] Average of 3 tests

Table 3.3 Tensile Strength of Concrete

Series	Compressive Force (k)[1]	f_{sp} (ksi)[1]
1	39.8	0.352
2	79	0.700
3	53	0.470

[1] Average of 3 tests

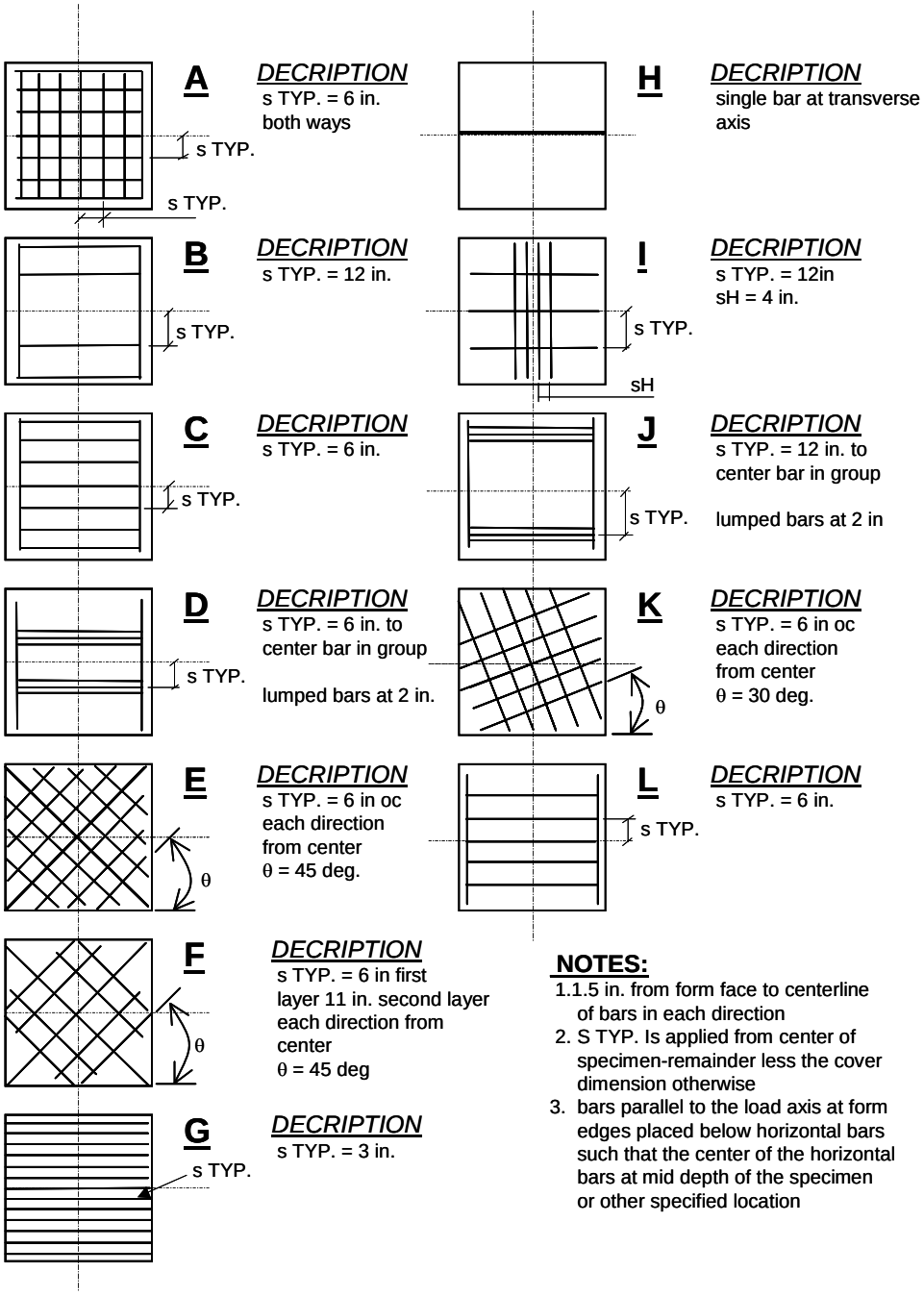

Figure 3.13 Details of Reinforcing Bar Placement

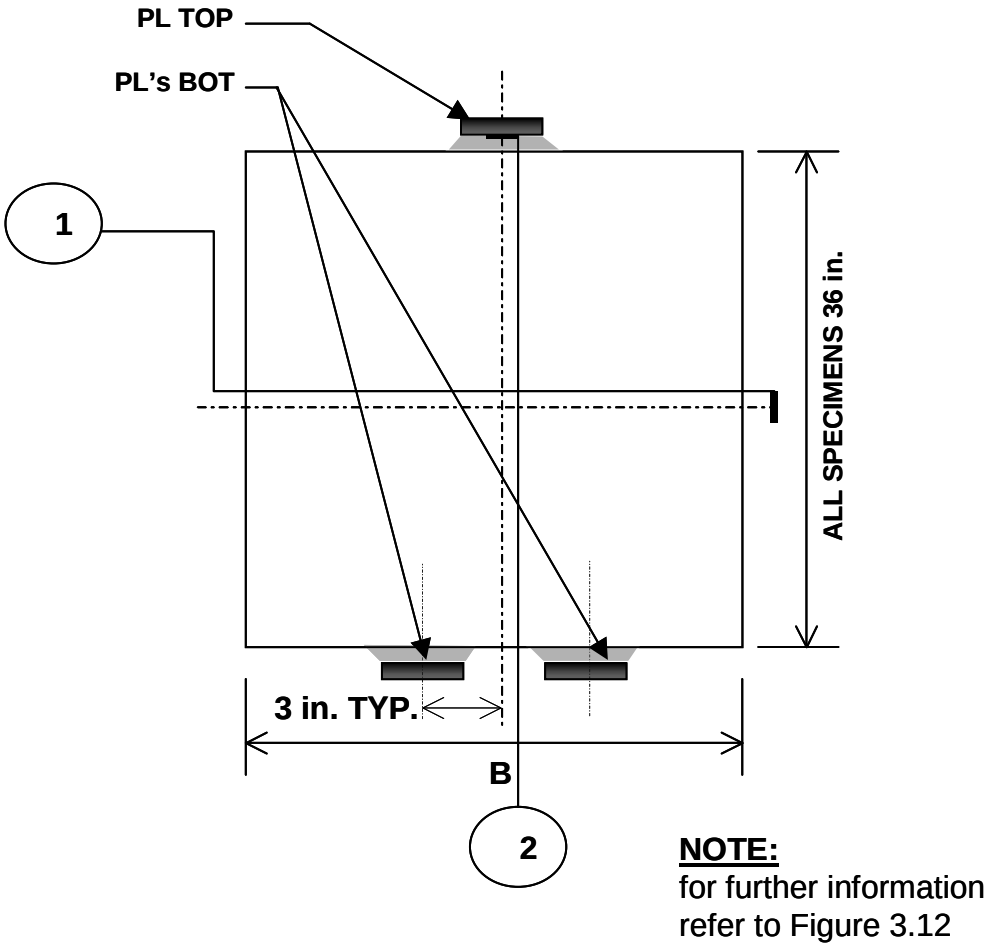

Figure 3.14 Specimen S3-4 Elevation at Testing

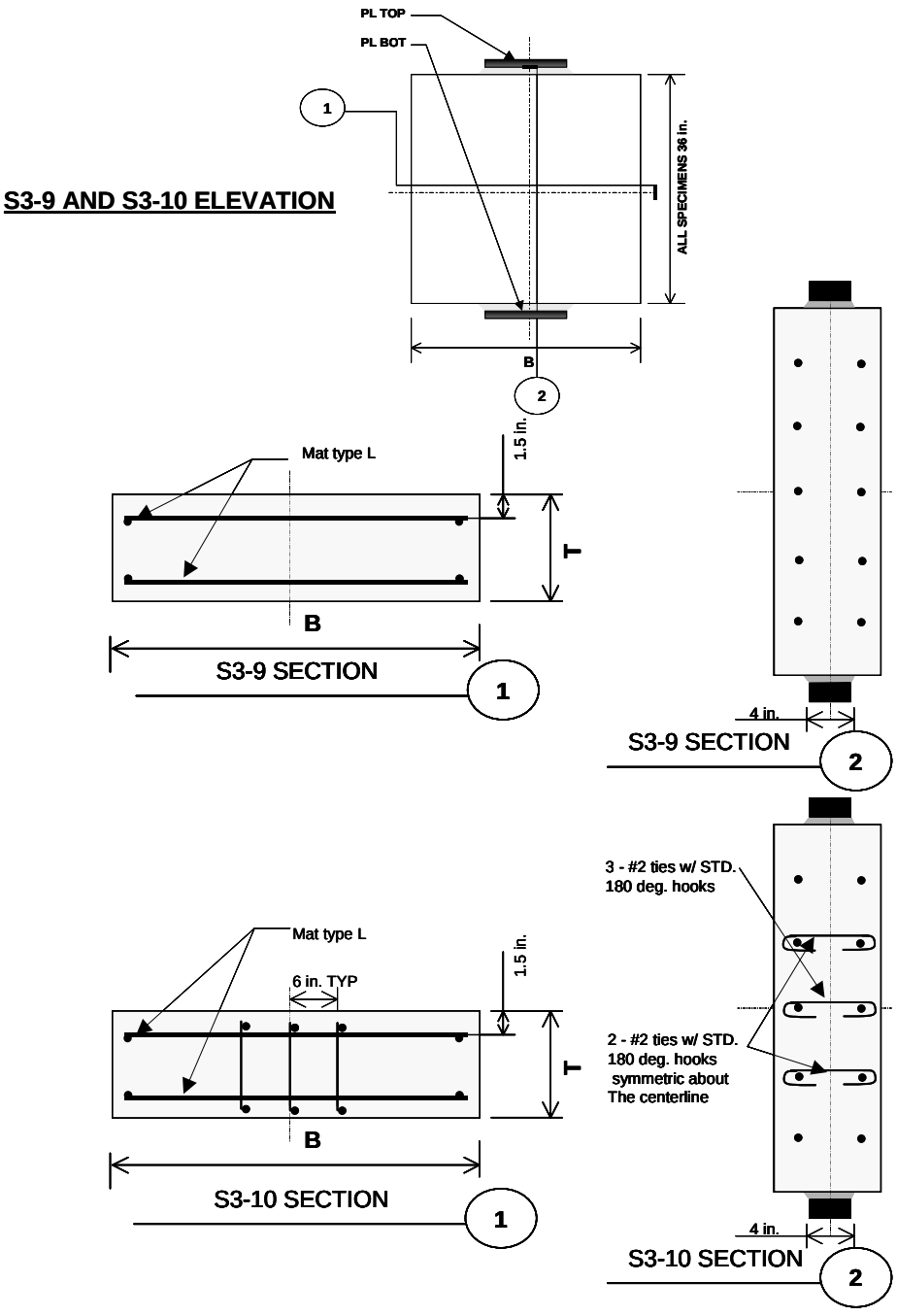

Figure 3.15 Specimens S3-9 and S3-10 Non-Standard Details

4.0 PRESENTATION OF THE TEST RESULTS

4.1 INTRODUCTION

The experimental program described in Chapter 3 is congruent with similar experimental investigations by many researchers ([11], [13], [21], [34], [39], [44]) in which specimens were loaded on a surface smaller than that of the supporting surface of the specimen. In these tests, compressive stresses spread away from their local introduction to a uniform stress distribution across the section. Most of these experimental investigations, with the exception of Sanders [44], concentrated on finding the ultimate bearing capacity of these specimens by using fracture mechanics or empirical relationships. Sanders [44] showed that the stress fields created from the local introduction of a bearing stress may also be modeled with the strut-and-tie method as bottle-shaped struts. This type of analysis provided a conservative estimate of the bearing capacity of the specimen provided that equilibrium and the chosen yield criteria were satisfied within the model.

The purpose of the experimental investigation reported herein was to build on the strut-and-tie method of modeling the behavior of specimens of this type which originated with the work done on NCHRP 10-29 [17], [39], [44], [51], which were described in Chapter 2.

The remaining experimental investigations that did not model the behavior of this type of specimens with the strut-and-tie method still provide some insight into the behavior of bottle-shaped struts and therefore will be mentioned briefly in the following paragraphs to provide

the reader with some basic background information on methods of previous analyses.

Experimental investigations that resulted in empirical relationships to describe the behavior of bottle-shaped struts include work done by Adebar and Zhou [11] in which specimens were tested in a manner similar to that of a double-punch-tested specimen as shown in Figure 4.1 A. The specimens were instrumented to capture the cracking load while the ratios of D/d and H/d were varied. The cracking load is a direct measure of the tensile strength of concrete in the double-punch configuration. In the Adebar and Zhou tests the cracking load was a function of both these ratios. An empirical relationship was produced that limited the compressive stress to that of the cracking stress for unreinforced specimens with the assumption that stress redistribution would be limited without reinforcement. Previous to Adebar and Zhou, Marti [27] provided a relationship based on fracture mechanics that accounted for the size effect of the specimens in determining a limiting tensile stress for concrete using double-punch tests which was substantiated by the work of Adebahr and Zhou.

More investigations that resulted in empirical relationships to describe the behavior of bottle-shaped struts are those of Niyogi [34], [35], [36], and Rigden et. al [13], [14]. The specimens fabricated in theses investigations were lightly instrumented when reinforcement was present, and only the ultimate load and failure mechanism was recorded when reinforcement was not present. Niyogi, presented empirical relationships based on the plate dimensions relative to the dimension of the loaded

surface; while, Rigden et.al presented a relationship based on linear regression of data to account for type and amount of reinforcement for a given loading condition.

Hawkins [21], [21] described the behavior of bottle shaped-struts using fracture mechanics, to model the conical failure cones observed under the bearing plate for various loading configurations.

In all previous investigations, the experimental data collected consisted of visual observations, ultimate bearing stresses under the loading plate, and steel strain gauges when reinforcing bars were present in the specimens. The current experimental investigation described in Chapter 3 supplied experimental results of 4 types:

- visual observations
- ultimate stress under the loaded area
- reinforcement strains
- concrete strains on the surface of the specimens

The results in these four series are presented sequentially in the following sections.

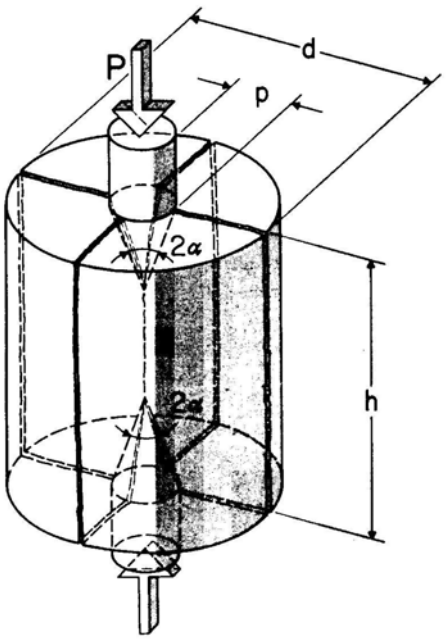

A) Double Punch Test

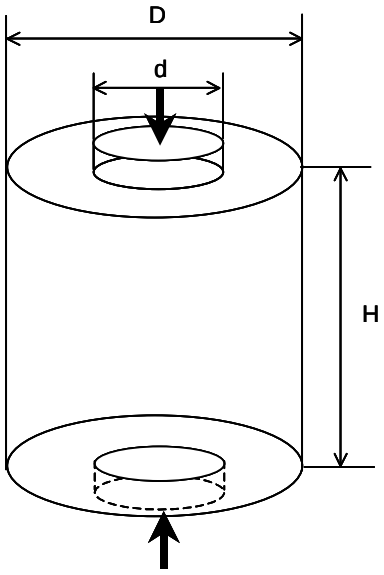

B) Adebar and Zhou [11]

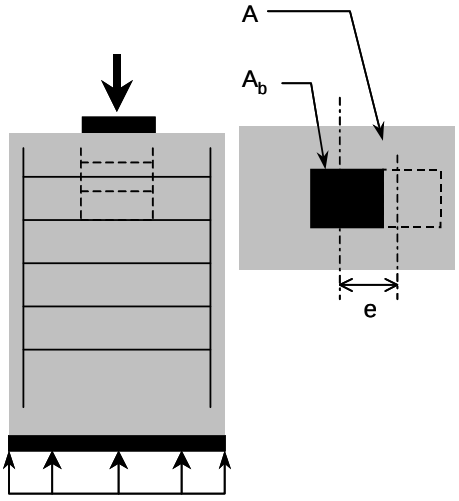

C) Sanders [44], Roberts [39]
Rigden et. Al. [13]

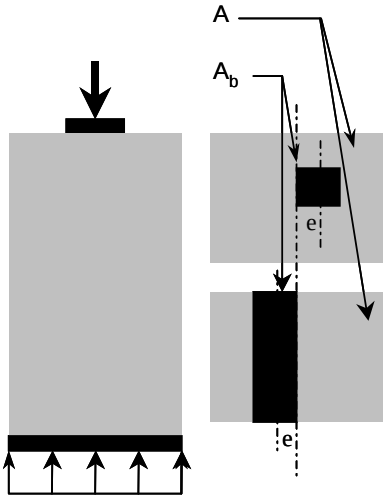

D) Hawkins [21], Niyogi [34]

Figure 4.1 Specimens Used in Investigating Bottle-Shaped-Struts

4.2 VISUAL OBSERVATIONS

The failure mechanism initiated in the same manner for all specimens in that a hairline crack formed at the specimen centerline parallel to the loading axis as shown in Figure 3.4 and propagated toward the bearing plate in either direction. The crack did not extend into the nodal zone, defined as an isosceles triangle with a height equal to half the bearing plate width, until the specimen was near failure. The next stage of the failure mechanism followed a trend as the percentage of reinforcement transverse to this crack increased in the specimens.

At ultimate failure, mechanisms ranged from a tensile failure (Figure 4.2) resulting in the failure of a plane bi-axially stressed tending to the crushing of the concrete at or around the nodal area (Figure 4.3) as the relative percentage of reinforcement increased. In every specimen tested concrete located directly under the bearing plate developed a wedge in the basic proportions of an isosceles triangle. In specimens with higher quantities of transverse reinforcement wedge concrete forming the node became smaller and more pronounced. Figure 4.2 displays the ultimate failure mechanisms for some “lightly” reinforced specimens while figure 4.3 displays the ultimate failure mechanisms for a number of specimens with higher percentages of transverse reinforcement. Figure 4.2 also shows the wedge of nodal concrete for specimen S3-10 which, with specimen S3-9, are the only specimens tested in which the bearing plate dimension was less than that of the thickness of the specimen

resulting in the three-dimensional confinement of the node by the surrounding concrete. Specimens S3-9 and S3-10 exhibited the tensile failure mechanism. In one case, specimen S2-8 (Figure 4-2) the failure plane is slightly inclined at the nodal region, as an extension of the tensile crack initiating at the specimen centerline. S2-8 contained #2 bars at 8 inches on center placed at 45 degrees to the load axis in two layers (Figure 3.13 F).

Figure 4.3 displays specimens with reinforcement percentages that force the failure mechanism from the tensile failures away from the node to crushing of the concrete at the node face. In these specimens the nodal area of concrete is apparent when extraneous crushed concrete is removed.

Figure 4.4 displays a basic comparison of two specimens with same reinforcement regime. The reinforcement for specimen S2-8 is as described above. S2-6 contained #3 bars at 6 inches on center oriented at 45 degrees relative to the load axis (Figure 3.13 E), placed in two orthogonal layers. The reinforcement percentage given in this figure is the component of total amount of reinforcement on plane parallel with the transverse axis. The ν_e value shown in this figure is the ultimate bearing stress normalized to the concrete strength. Comparing the failure mechanisms in this manner the specimens can be classified as “confined” since they exhibited the crushing failure and pronounced nodal wedge or “unconfined” which exhibit the tensile failure mechanism.

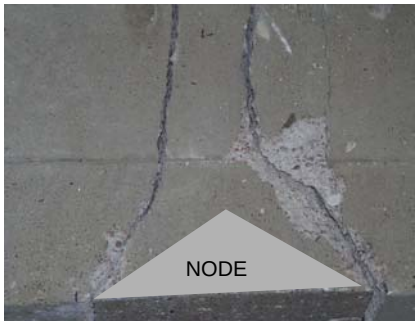

S1-2

S1-4

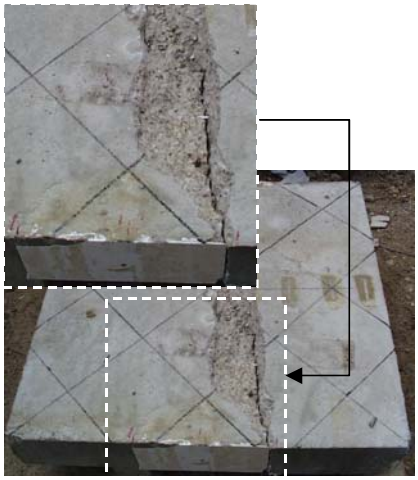

S2-8

S3-10

Figure 4.2 Tensile Failure Mechanism

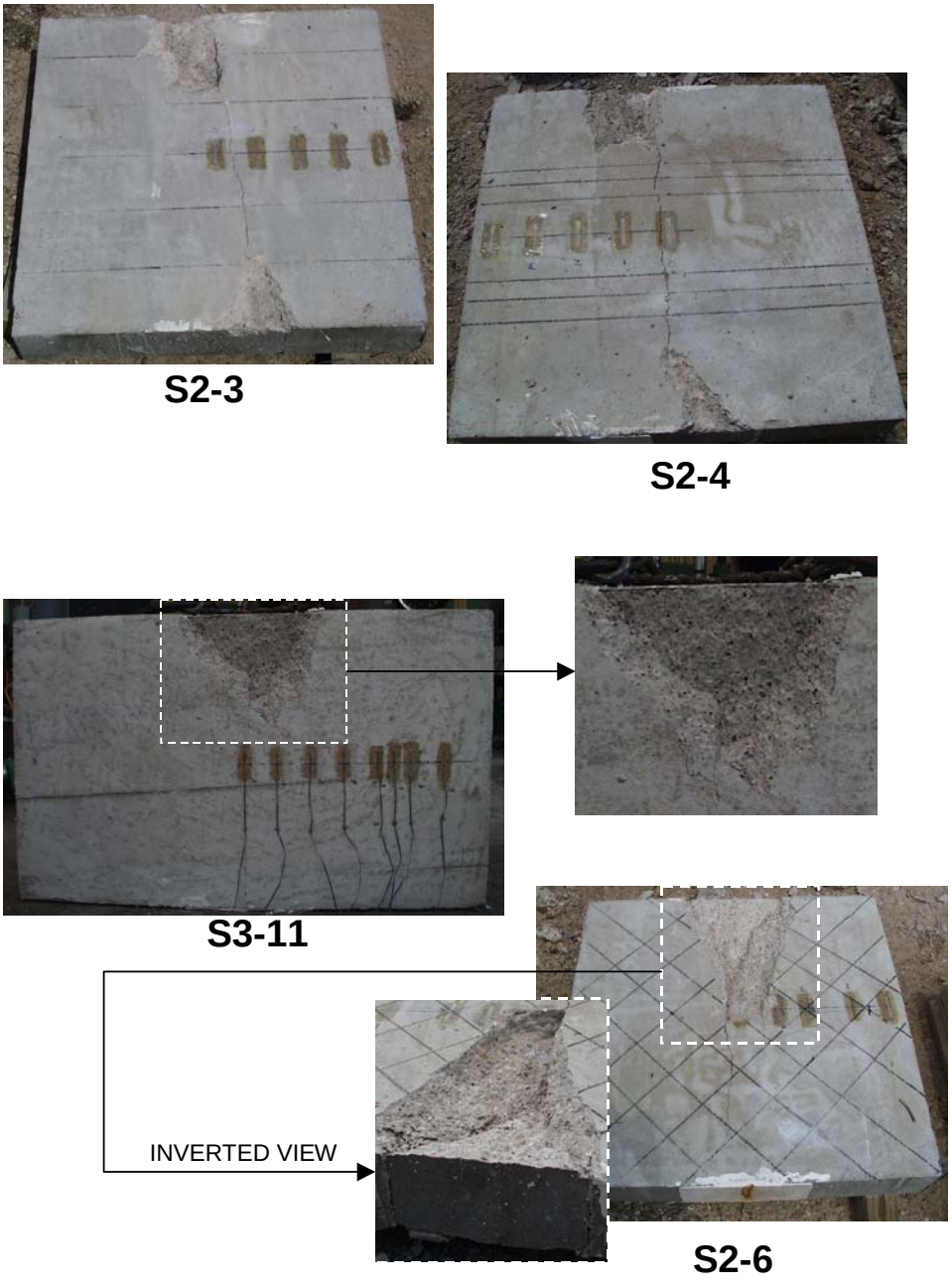

Figure 4.3 Concrete Crushing at Node Failure Mechanism

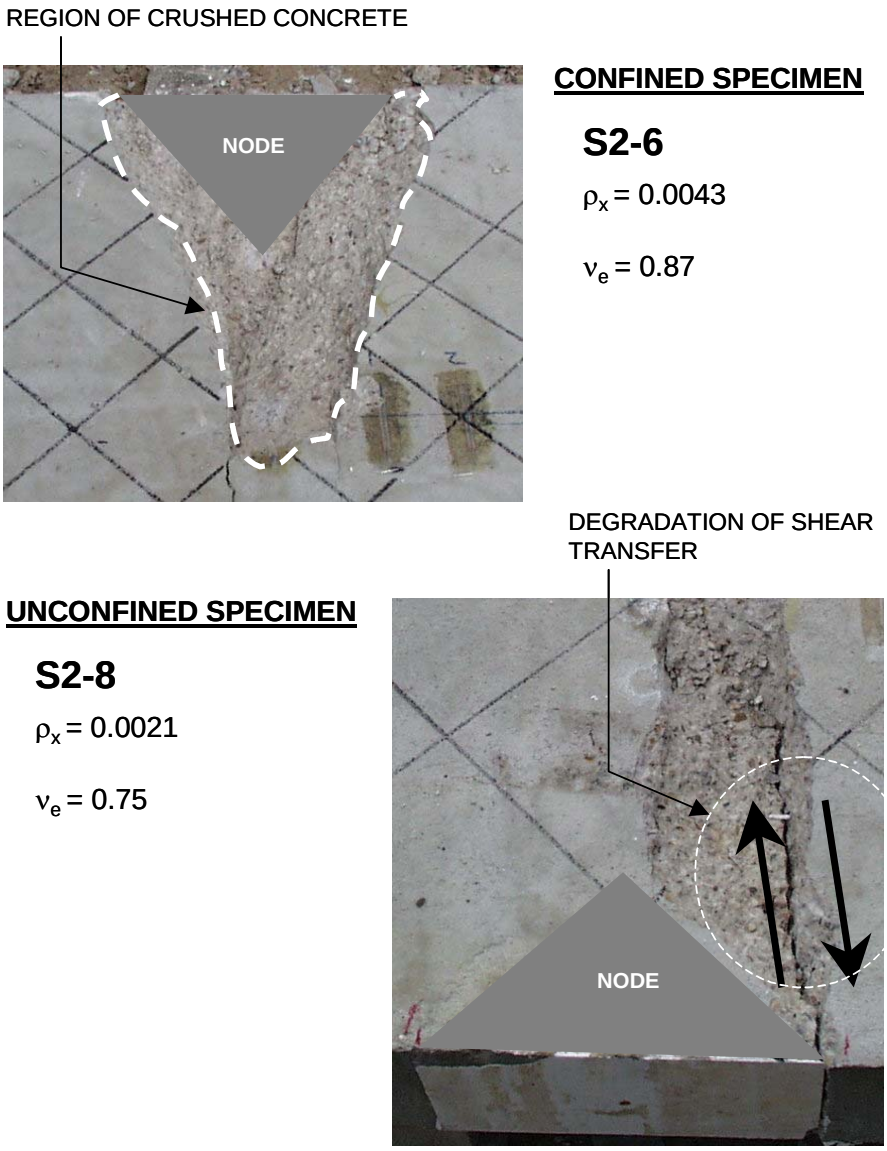

Figure 4.4 Comparison of Failure Mechanisms for Confined and Unconfined Specimens

The degradation of shear transfer reported by Wollman [51] is shown in specimen S2-8 in Figure 4.4. Figure 4.5 presents a similar degradation as the point where the internal angle of friction of the concrete is less than that of the coefficient of static friction between to rough concrete surface areas. The concrete in confined specimens crushes before significant shear degradation occurs.

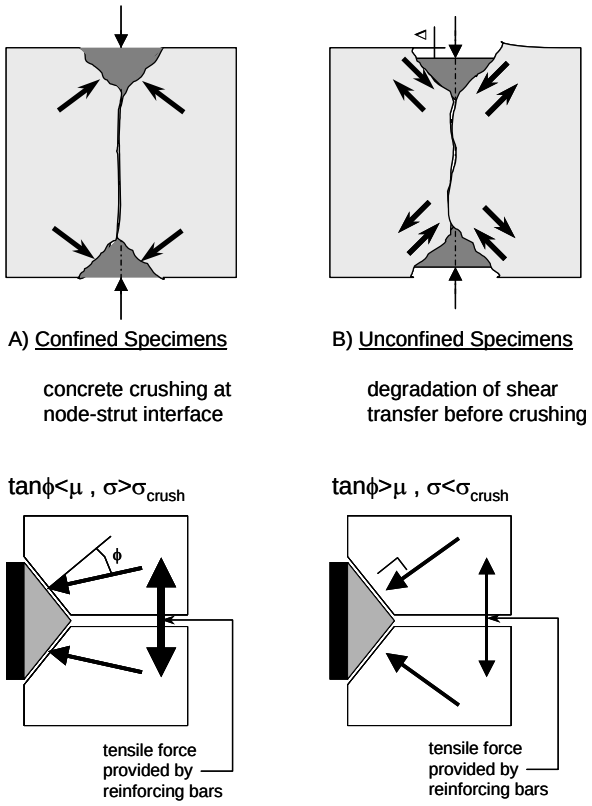

Figure 4.5 Degradation of Shear-Transfer for Unconfined Specimens

In the case of confined specimens a secondary failure mechanism was observed at or immediately after the crushed concrete at the node as shown in Figure 4.6. This mechanism can be described as splitting tensile failure initiating at the bearing plate and propagating down the loaded surface of the specimen. In some cases the tensile crack propagated down the outer edge of the specimen parallel to the load axis. It is likely that this mechanism began to form as the node was forced toward the transverse axis generating a cleaving action in the specimen. For specimen S2-10, the most heavily reinforced specimen, this failure occurred simultaneously with concrete crushing around the node resulting in an extremely explosive and brittle failure. It is also interesting to note that crack on the loaded surface only appeared to the side of the node in which concrete has crushed, which is an indication that these failure mechanism are linked.

4.2.1 Summary of the Results Obtained from Visual Observations

It is clear from the observation of the failure mechanism of these specimens that, as the percentage of transverse reinforcement increased, the failure mechanism changed from a tensile failure on planes away from the nodal area to compressive failures at or near the nodal face. A secondary tensile failure along the loaded surface associated with the compressive failure of “heavily” reinforced specimens is also apparent. The observed failure mechanism can be used to classify the specimen as either “confined” exhibiting the crushing failure or “unconfined” exhibiting the tensile failure.

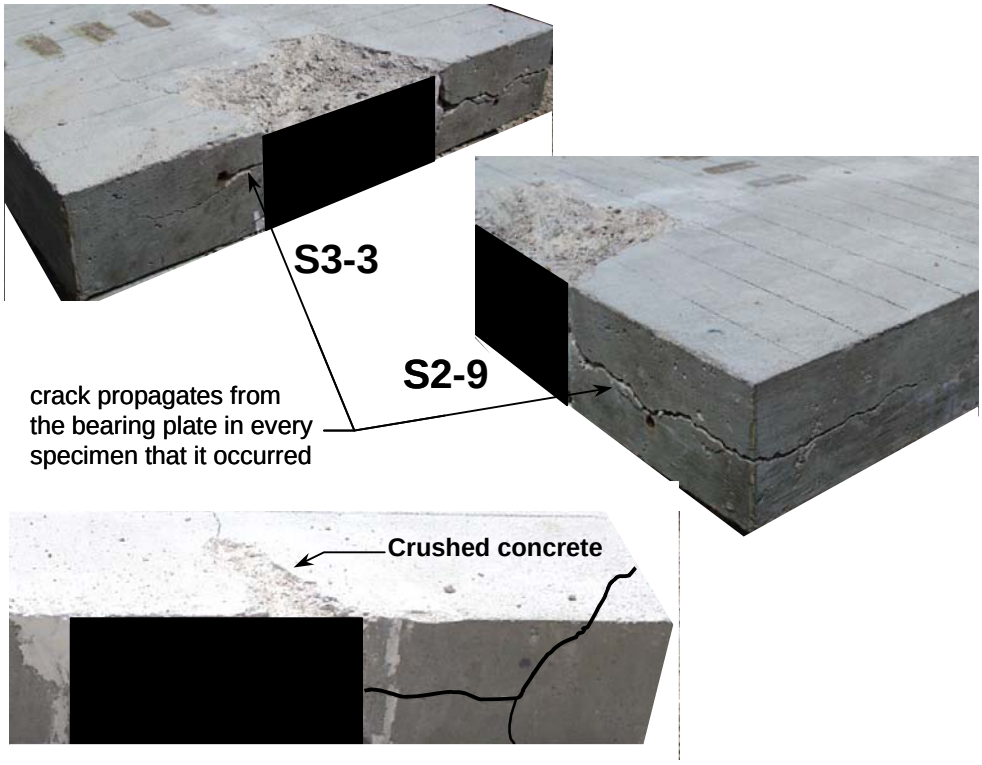

S2-4 crack on bearing surface to the same side as crushed concrete

S2-9 maximum transverse reinforcement within experimental investigation

Figure 4.6 Secondary Failure Mechanism Associated with "Heavily" Reinforced Specimens

4.3 ULTIMATE STRESS UNDER LOADED AREA

After cracking and ultimate stresses under the bearing plate area were normalized with respect to f`$_c$ (ν_e - ultimate efficiency factor, ν_c - cracking efficiency factor) to allow comparisons, a distinct categorization was apparent. The ultimate load carried by the specimens was a function of reinforcement provided, the ratio of cross-sectional area to that of the bearing plate area ($A=bt/A_b$), as well as, the ratio of the height of the specimen to the thickness of the specimen.

Furthermore, the three specimens in series 1 (S1-3, S1-4, S1-5) which had nodal confinement in the form of closed ties had high bearing capacities relative to those which contained similar reinforcement and A/A_b ratios. The ultimate capacities of specimens S1-3, S1-4, and S1-5 however, were less than those specimens with higher A/A_b rations with no confinement of the node.

Specimens S3-9, and 3-10, which also had the largest bt/Ab ratios and similar reinforcement ratios as specimens S2-3, S2-4, S2-7, S3-4 and S3-7, exhibited the largest capacity. The ultimate bearing capacities are shown in increasing order in Figure 4.7, and grouped according to their geometric ratios (A/A_b, h/2b).

The term $\nu_e - \nu_c$ or the normalized ultimate stress less the normalized cracking stress is an indicator of the level of redistribution in the specimens. This term is plotted in Figure 4.8, and it is apparent that the level of redistribution is proportional to A/A_b ratio. This behavior is similar to that observed by Adebar and Zhou [11]. The first group of

specimens is plotted in Figure 4.9, in which there is the most drastic variation of transverse reinforcement; it is apparent that the amount of stress redistribution is directly proportional to the amount of reinforcement provided.

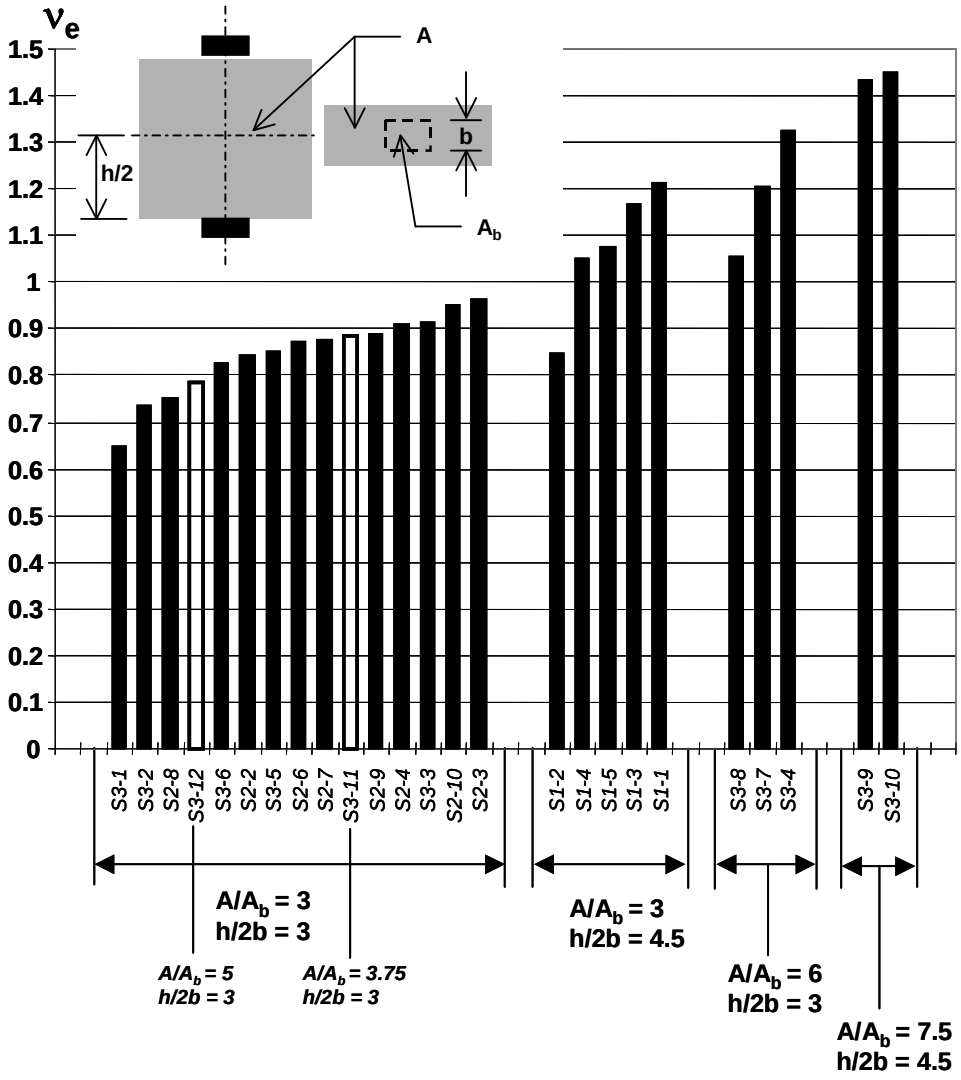

Figure 4.7 Ultimate Capacities

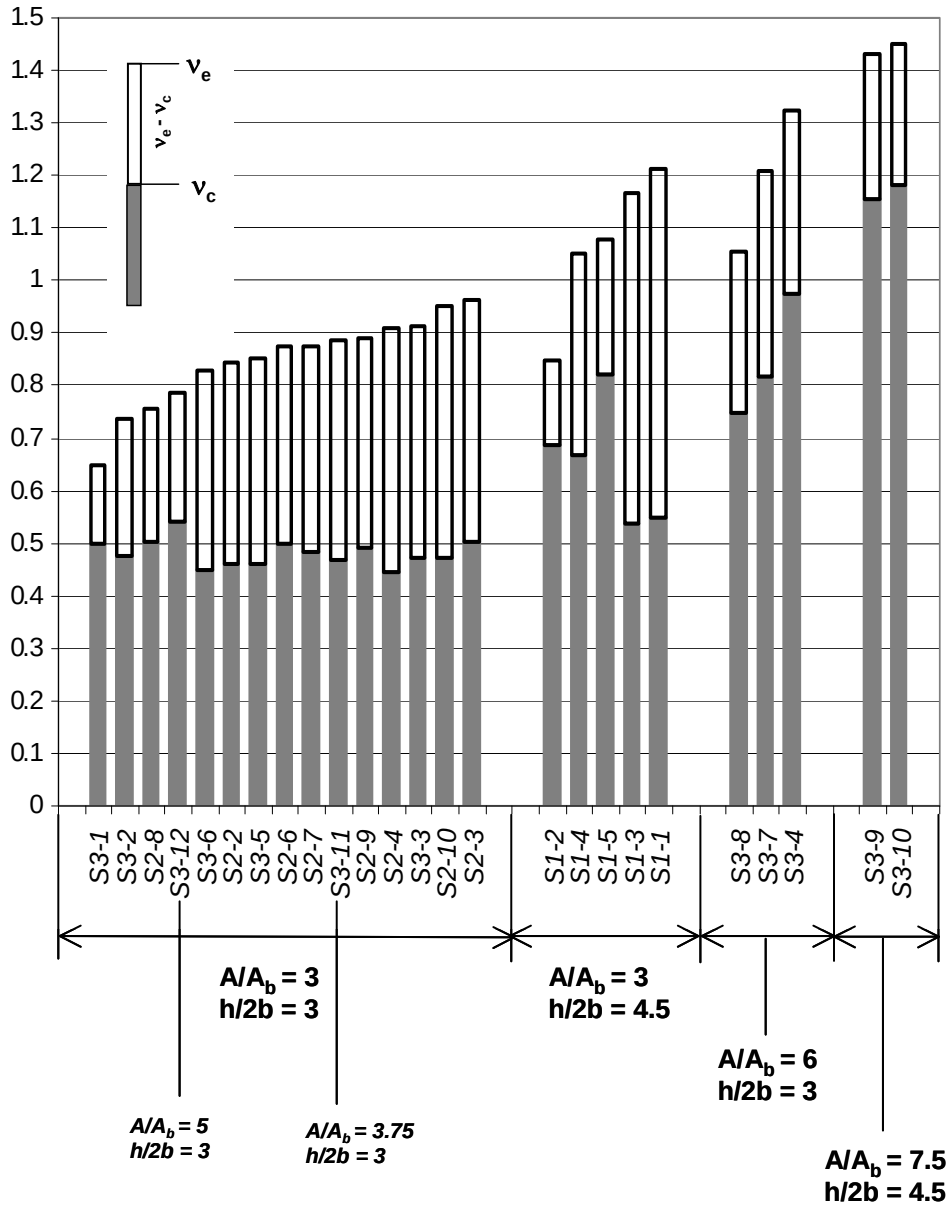

Figure 4.8 Stress Redistribution

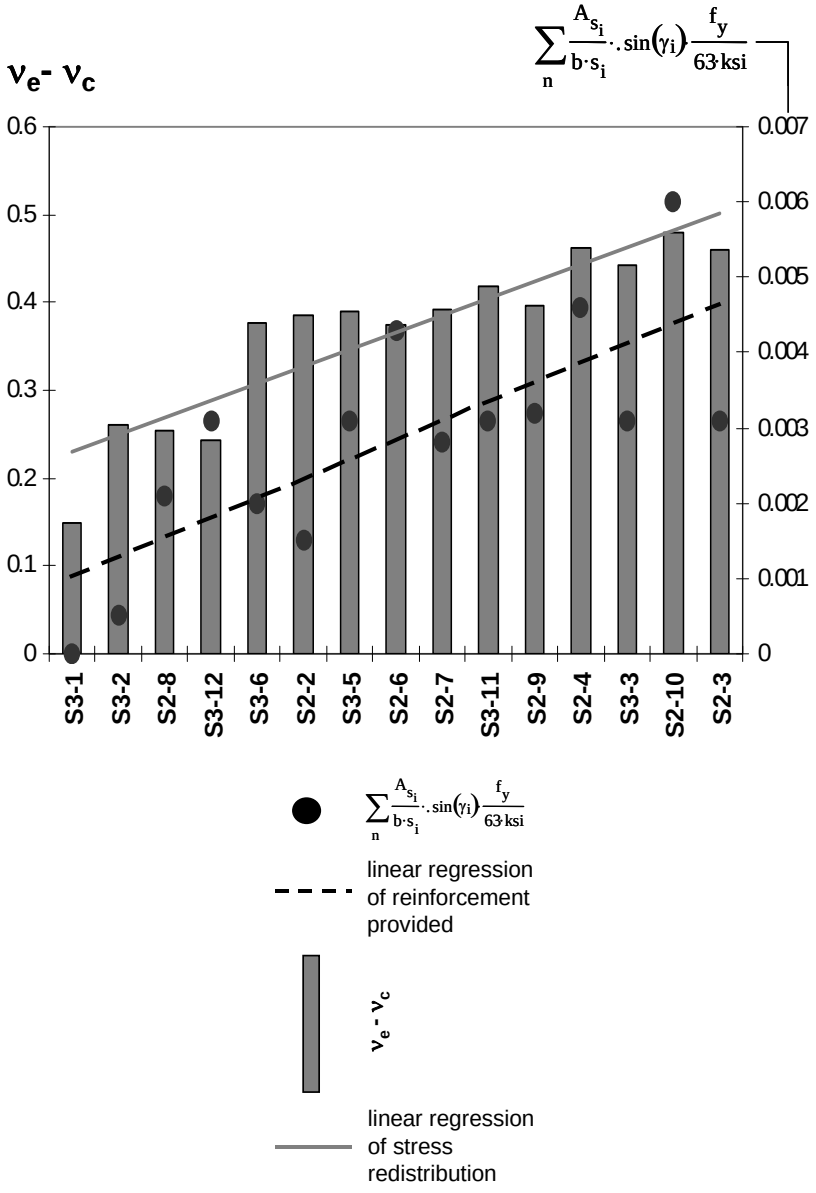

Figure 4.9 Dependence of Stress Redistribution on Reinforcement Provided

The amount of reinforcement provided in each specimen enhanced the ultimate capacity of the specimens also as shown by Figure 4.10.

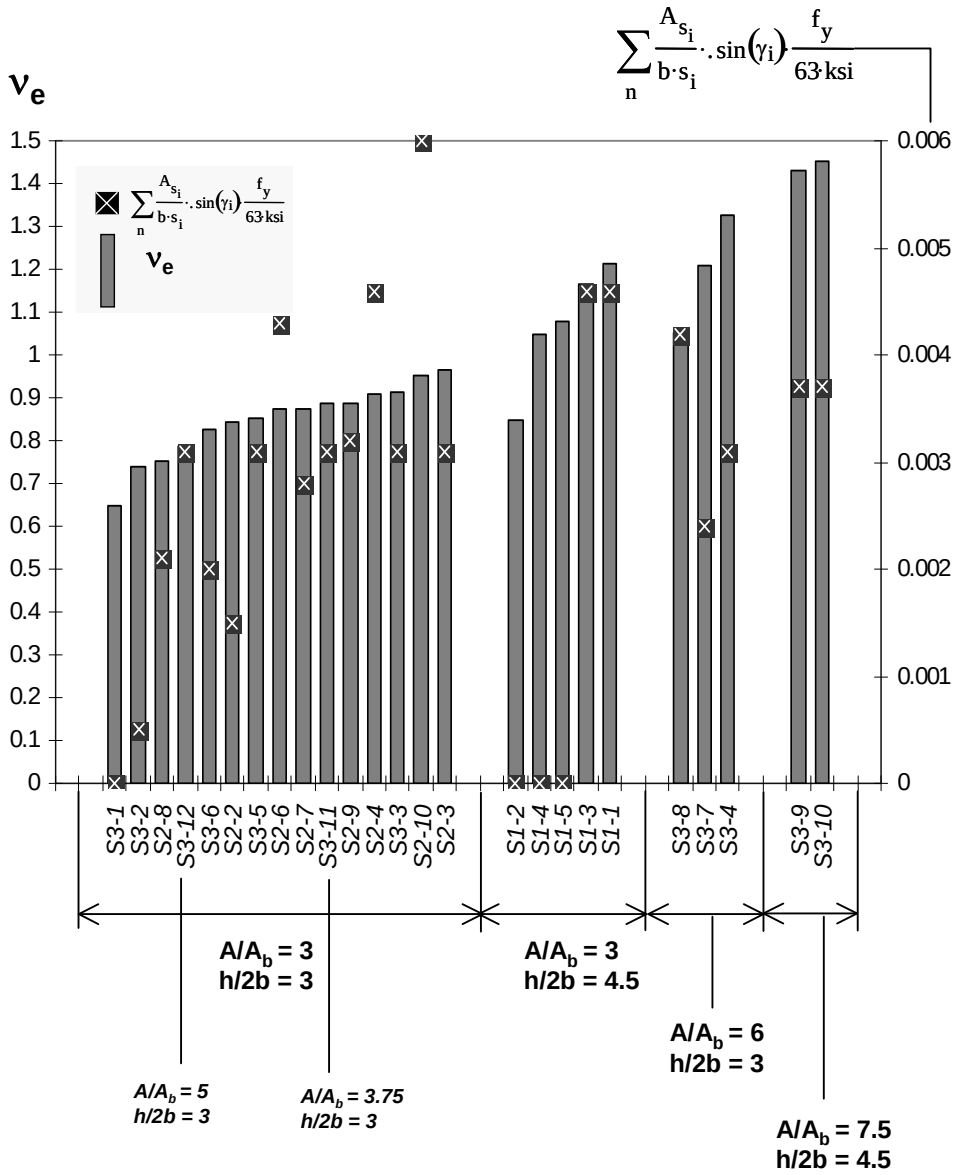

Figure 4.10 Effect of Reinforcement on Ultimate Capacity

It is apparent from Figure 4.10 that there is an upper limit on the increase in the ultimate capacity attributable to the reinforcement provided. Specimen S2-10 had a relative reinforcement ratio twice that of specimen S2-3 yet the capacities were similar. For A/A_b ratios equal to 6, it appears that the reinforcement provided had little or no effect on the capacity. Specimen S3-8 had the greatest amount of reinforcement yet the lowest capacity within the group. This specimen was reinforced with #3 bars at 6 inches on center placed in an orthogonal mat that was rotated at an angle of 30 degrees relative to the load axis resulting in half the reinforcement at an angle of 30 degrees relative to the load axis and half the reinforcement at an angle of 60 degrees relative to the load axis (Figure 3.13 K). The configuration of the reinforcement was not efficient in confining the specimen and therefore the ultimate capacity is lower than those specimens in the group with less reinforcement placed perpendicular to the load axis of the specimen. The reinforcement provided in specimen S3-9 was placed in two mats near the outer surfaces of the specimen (Figure 3.15). The reinforcement provided in S3-10 was identical to S3-9 with an additional 35 % of transvere reinforcement placed as ties between the two layers of steel placed near the form and finished faces (Figure 3.15). Both configurations of reinforcement were inefficient in further enhancing the ultimate capacity of the specimen and are consistent with the findings of Rigden et al [13].

4.3.1 Summary of the Results Obtained from the Ultimate Stress under the Loaded Area

The ultimate stress under the loaded area or the ultimate capacity of each specimen is influenced by the geometric conditions of loading which provide different levels of confinement for the nodal area, as well as, the amount of confining reinforcement placed at the nodal area. The ultimate capacity was also enhanced by the amount and orientation of reinforcement provided with respect to the load axis of the specimen. The enhancement of the ultimate capacity by reinforcement reaches a saturation point at which the specimen will fail in compression regardless of the amount of reinforcement provided.

4.4 RESULTS OBTAINED FROM REINFORCEMENT STRAINS

The readings taken from the strain gauges placed on the reinforcement, when plotted against the normalized ultimate capacity, further help identify the failure mechanism for each specimen. Figure 4.11 shows the strain recordings for bars placed at three-quarter height of four specimens that typify the behavior for the two categories of “confined specimens” and “unconfined specimens”. The initiation of the shear degradation (Figure 4.5) resulting from a tensile failure can be seen in the unconfined specimens S3-6 and S2-2 at points X and Y where the slope of the stress-strain curves reduces and becomes nearly horizontal. The relatively flat slope is an indication of the large deformation resulting from the node cleaving the specimen. Point X and Point Y, which are the

points at which the shear degradation begins, are dependent on the amount of reinforcement provided within the specimen,

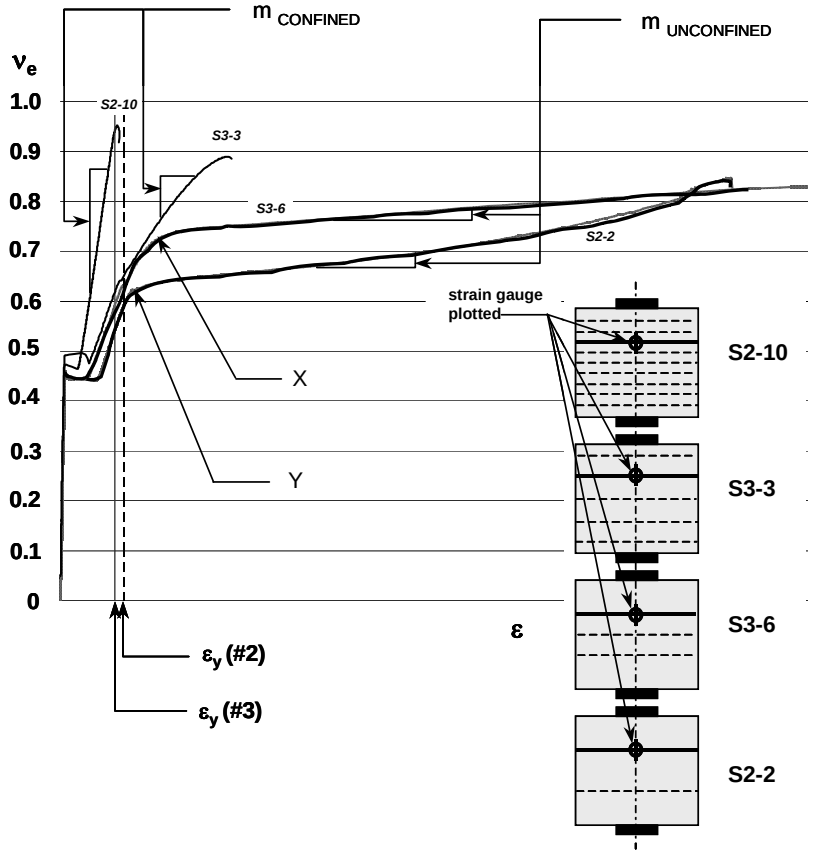

Figure 4.11 Strain Recordings Indicating the Type of Failure Mechanism

The strain recordings normalized to the bearing stress for confined specimens have a steeper slope leading to failure by crushing of the concrete at and around the nodal area. The slope of these lines is dependent on the total amount of reinforcement provided within each specimen and not on the yield strength of the reinforcing bars used.

To estimate the stresses in the reinforcement at various load stages the strain recordings were converted to stresses using the elastic-plastic relationship shown in Figure 4.12 and into forces by multiplying the stress by the area of the reinforcing bar. The elastic-plastic relationship was chosen because the strain-hardening range of a typical stress-strain curve for reinforcing bars was reached only in specimens with minimal transverse reinforcement (S2-2, S3-2, and S3-6).

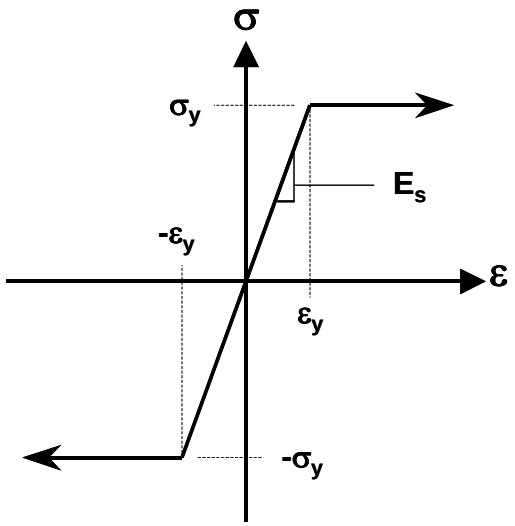

Figure 4.12 Constitutive Relationship for Reinforcing Steel

The stress in the reinforcing bars at various heights, separated according to confined and unconfined condition, are plotted in Figure 4.13 at a load equal to 90% of the cracking load to estimate the tensile stress in the specimen before cracking. Regression analyses of the data points provide an average stress in the elastic range of confined and unconfined specimens. The order of regression was chosen based on the least cumulative error between the regression line and the data points.

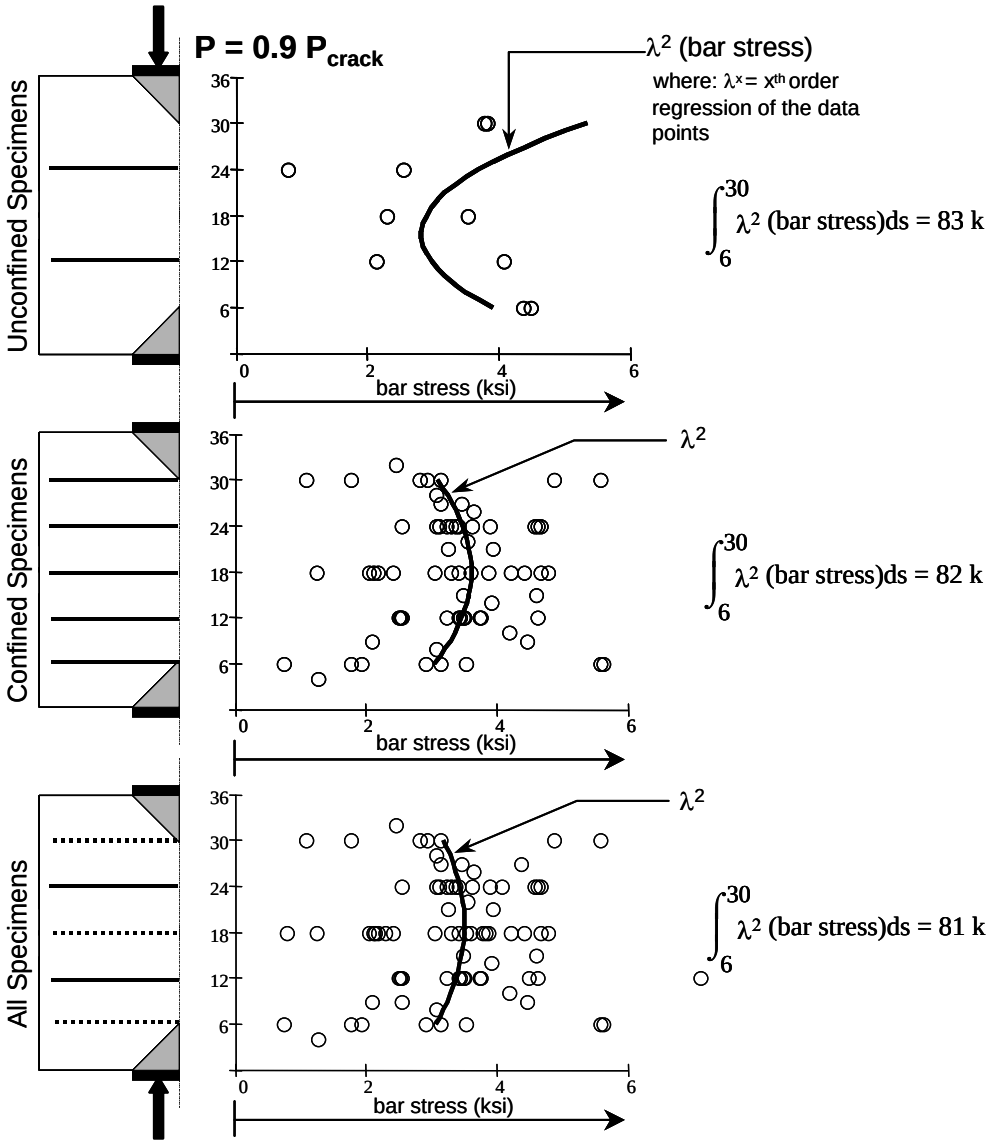

Figure 4.13 Average Reinforcement Stress in the Elastic Range for Confined and Unconfined Specimens

An integration of the average stress over the height of the specimen excluding the nodal area (assumed 6” at either end) yields similar values of the tensile force at the centerline of a specimen for confined and unconfined specimens even though the regression is quite different in either case. Integrating the reinforcing steel stress over the area of the specimen clearly implies a cross-section made of steel. To convert the area of steel to an area of concrete the geometric mean of the modular ratio for all specimens was computed, and after the conversion an average concrete tensile stress 0.09 f’c was computed. This value is consistent with tensile strengths obtained from split-cylinder tests which range from 0.07 f`c to 0.12 f`c, as well as, the average split-cylinder tensile strengths obtained for these specimens which was equal to 0.11f`c.

It is apparent from Figure 4.13 that the reinforcement is strained little in the elastic range and the stresses developed in the reinforcing bars of confined and unconfined specimens are of similar magnitude. Once the initial crack at the centerline of the specimen forms the strains and stresses of the reinforcing steel began to deviate according to the geometric conditions of loading. The deviation is shown in Figure 4.14 in which the regression of the bar forces along the height of the specimen is different for three main geometric conditions of loading. For the four inch thick specimens tested in Series 1, the regression of the bar force tends to pinch toward the center, while the six inch thick specimens have a more robust distribution of bar force along the height. The regression line for the specimens loaded with six inch by six inch bearing plates is misleading by showing a curve that tends to decrease over the height. This decrease

results from the testing conditions of three specimens tested with six inch by six inch bearing plates. In two of these specimens the upper bearing plate was a six inch by six inch bearing plate while the lower bearing area was either two six inch by six inch bearing plates spaced at a distance of six inches apart or a single six inch by twelve inch bearing plate; only one of the three specimens (S3-8) was tested with two six inch by six inch bearing plates at both ends. There was only two strain gauges at midheight in this specimen, one of which was functional. The direct comparison of the group with the A/A_b ratio equal to six is not exactly fair or valid because only one of three specimens in the group was tested using typical bearing plate configuartions, but is included to display the effect of the size of bearing plate on the reinforcement strains.

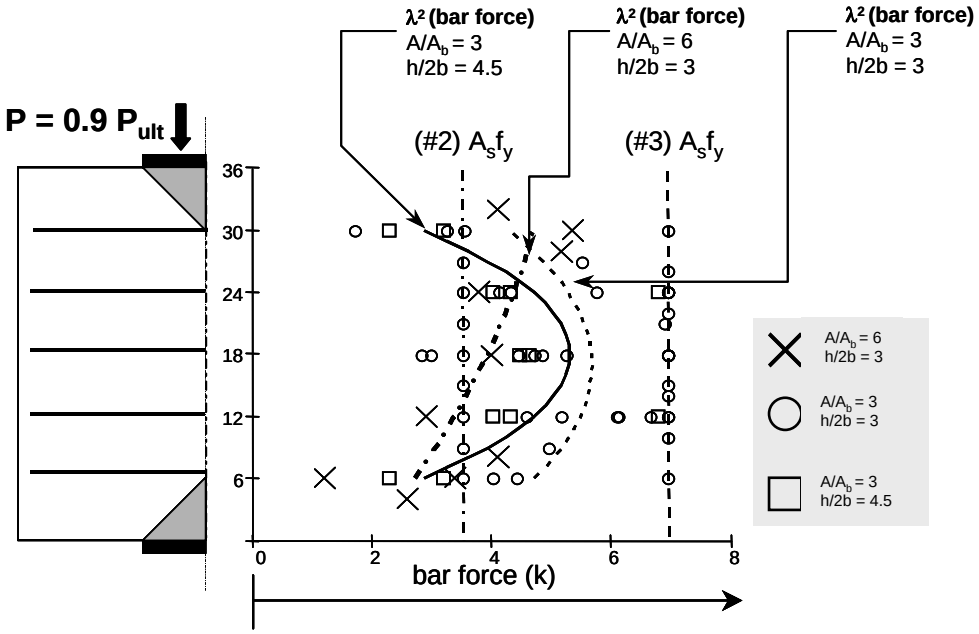

Figure 4.14 Reinforcing Bar Forces of Confined Specimens of Different Geometric Loading Conditions

A direct comparison of the regression of bar forces along the height of the specimen of confined and unconfined specimens was made, and is shown in Figure 4.15. From this figure, the average bar force is higher at the loaded surfaces of the specimen for unconfined behavior opposed to confined behavior which shows a robust distribution of bar force along the height of the specimen with maximum force was reached at mid-height.

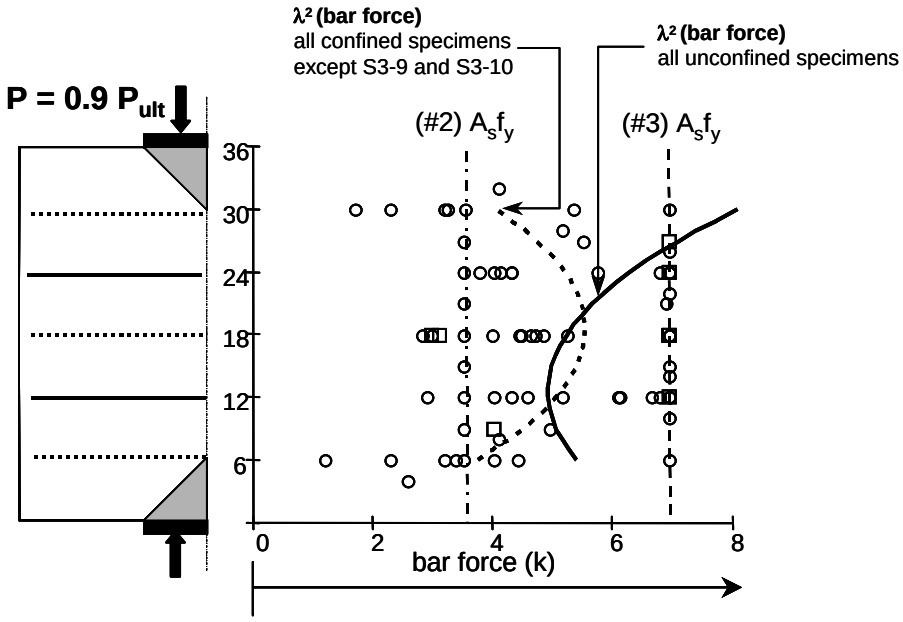

Figure 4.15 Reinforcing Bar Forces of Confined and Unconfined Specimens

For the two three-dimensional specimens tested (S3-9, S3-10) the bar stresses parallel to failure plane are stressed to 60-70% of their yield stress values. In Specimen S3-10, reinforcement was placed perpendicular to the failure plane, and Figure 4.16 shows that the stresses in these bars were around 3% of the forces in the bars parallel to the failure plane. From Figure 4.16, it would appear that the reinforcement

which directly crossed the failure plane was highly inefficient in redistributing the stresses after cracking, more so than reinforcement placed at the outer edges parallel to the failure plane. This could also be an indication that reinforcement of this type does little to enhance the capacity of three-dimensional specimens. A more suitable type of reinforcing arrangement would be closed ties around the perimeter of the specimens as suggested by Rigden et al [11].

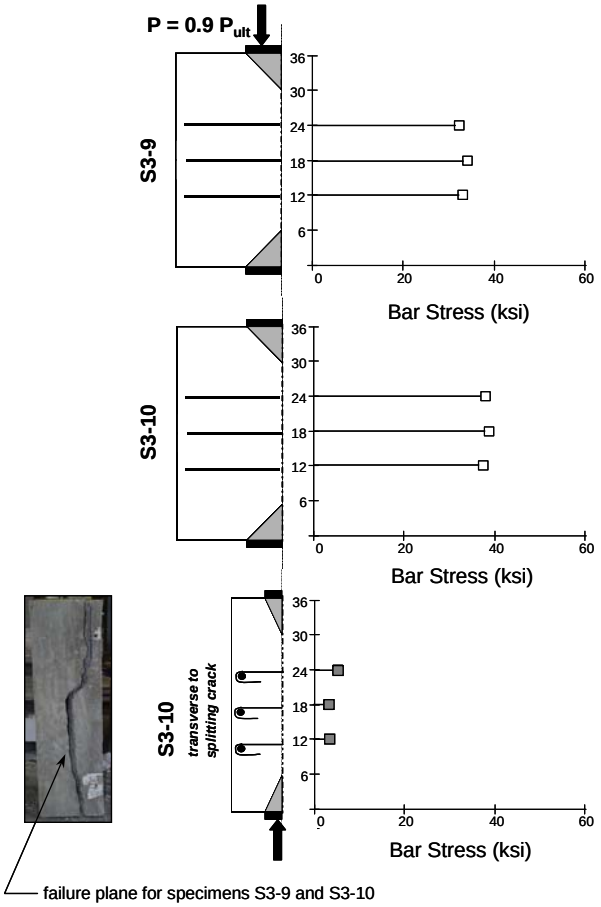

Figure 4.16 Reinforcing Bar Forces for Three-Dimensional Specimens

The reinforcement pattern in five specimens (S1-1, S1-3, S1-6, S3-5, and S3-6) contained reinforcing bars parallel to the load axis as well as perpendicular to the load axis of the specimen. In order to define the effect of the reinforcing bars parallel to the load axis, these bar forces at the ultimate load were computed and subtracted from the ultimate capacity as shown in Figure 4.17. On average the bar forces parallel to the load axis were stressed to a level of 63% of that of the reinforcing bars perpendicular to the load axis. The net effect of reinforcing parallel to the load axis was minor.

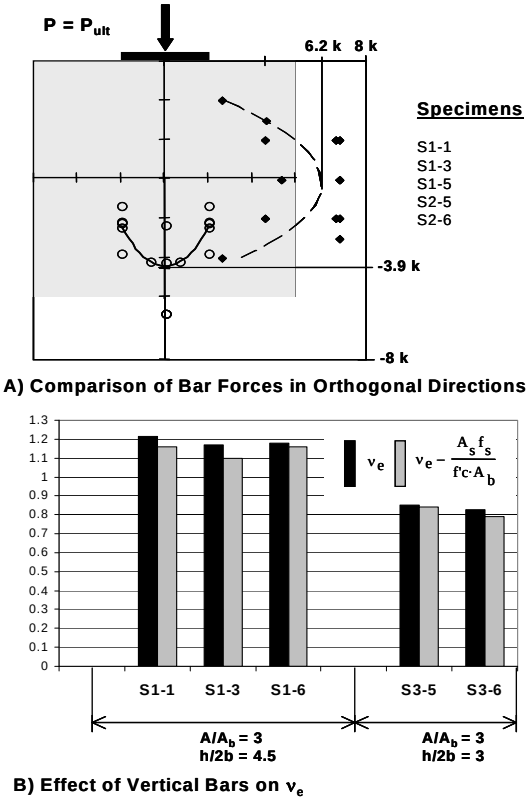

Figure 4.17 Effect of Reinforcing Bars Parallel to the Load Axis of the Specimen

While keeping the percentage of reinforcement relatively constant as well as the geometric conditions of loading (A/A_b = constant, h/2b = constant), the orientation, size, and distribution of the reinforcement varied in several specimens. The effect of the orientation, size, and distribution of reinforcement had little effect on the ultimate capacity of the specimens as shown in Figure 4.18.

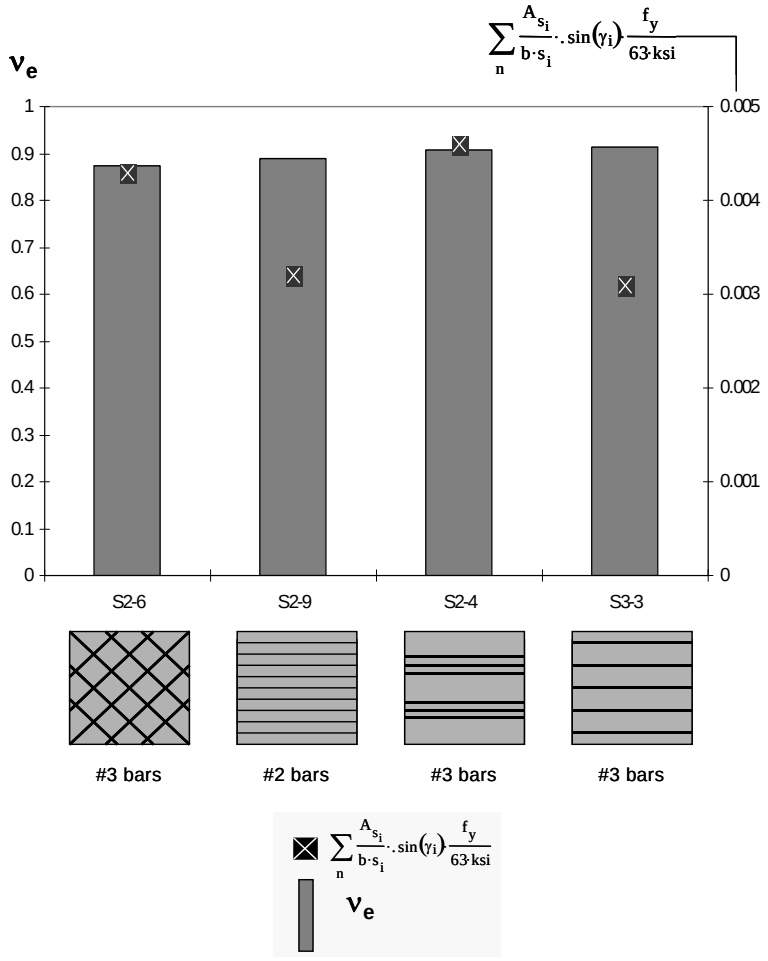

Figure 4.18 Effect of Variations of Reinforcement on the Ultimate Capacity of the Specimen

4.4.1 Summary of the Results Obtained from Reinforcement Strains

For planar specimens the amount of reinforcement provided enhanced the ultimate load carrying capacity of the specimen, with a stress redistribution occurring past the initial cracking and in some cases pass the yield point of the reinforcing bars. For confined behavior a saturation level is apparent by comparing specimens S2-3 and S2-10 which had similar capacities yet specimen S2-10 had twice the percentage of reinforcement as S2-3. For the same percentage of reinforcing steel provided, the orientation of reinforcing bars either perpendicular to the load axis or at angles of 45 degrees produced the same level of enhancement and a confined failure while reinforcing bars placed at angle less than 45 degrees relative to the load axis produced an unconfined failure of specimen S3-8. Furthermore lumped reinforcing and distributed reinforcing of the same amount produced similar effects either providing a confined or unconfined failure of the specimen depending on the amount of reinforcement provided. Reinforcing bars parallel to the load axis of the specimen provided little enhancement to the ultimate capacity or influenced the type of failure.

An interesting result obtained from the reinforcing strains is that the tensile forces in the reinforcing bars of specimens exhibiting the unconfined failure were, on average, greater at the loaded surface of the specimen while the tensile forces of reinforcing bars of specimens exhibiting the confined failure were, on average, maximum at the center of the specimen.

4.5 RESULTS OBTAINED FROM CONCRETE STRAIN ON THE SURFACE OF THE SPECIMENS

The most significant result from concrete strains on the surface of the specimen was that, in almost every specimen tested, tensile strains were developed at the outer edge of the specimen. The magnitude of the tensile strains was dependent on the amount of reinforcement provided within the specimen. Specimens exhibiting unconfined failure exhibited large tensile strains at the outer edge while specimens exhibiting the confined failure had smaller magnitudes of tensile strains at the outer edge.

When small or no tensile strains were present in the specimen reasonable values of concrete stress were attainable by using a slightly modified version of Hognestad's parabola as a constitutive relationship, and the stresses (assumed constant over the thickness) integrated over the area matched well with the load applied as seen in Figure 4.19.

In some instances as with specimen S2-2 recorded tensile strains were higher than 0.001 with no visible cracking at the location of this strain. It is impossible that the concrete could achieve a stress 0.9f'c using a linear E_c - ε relationship for tensile stress. Figure 4.20 shows the post testing conditions of specimen S2-2 and the strain recording for the concrete surface gauge and a reinforcing bar directly beneath it. The two gauges match quite well, however the stress in concrete and the stress in the steel are significantly different.

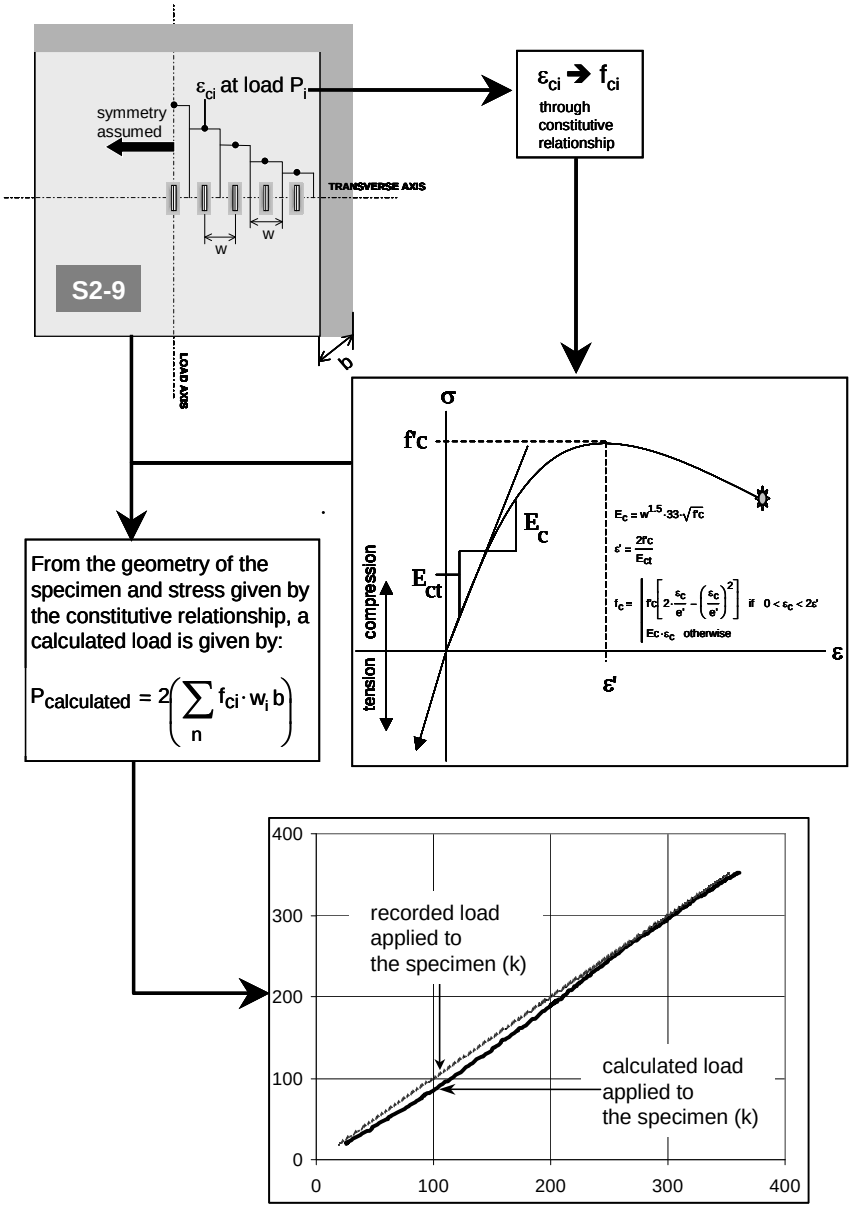

Figure 4.19 Verification of Constitutive Relationship for Compressive Strains

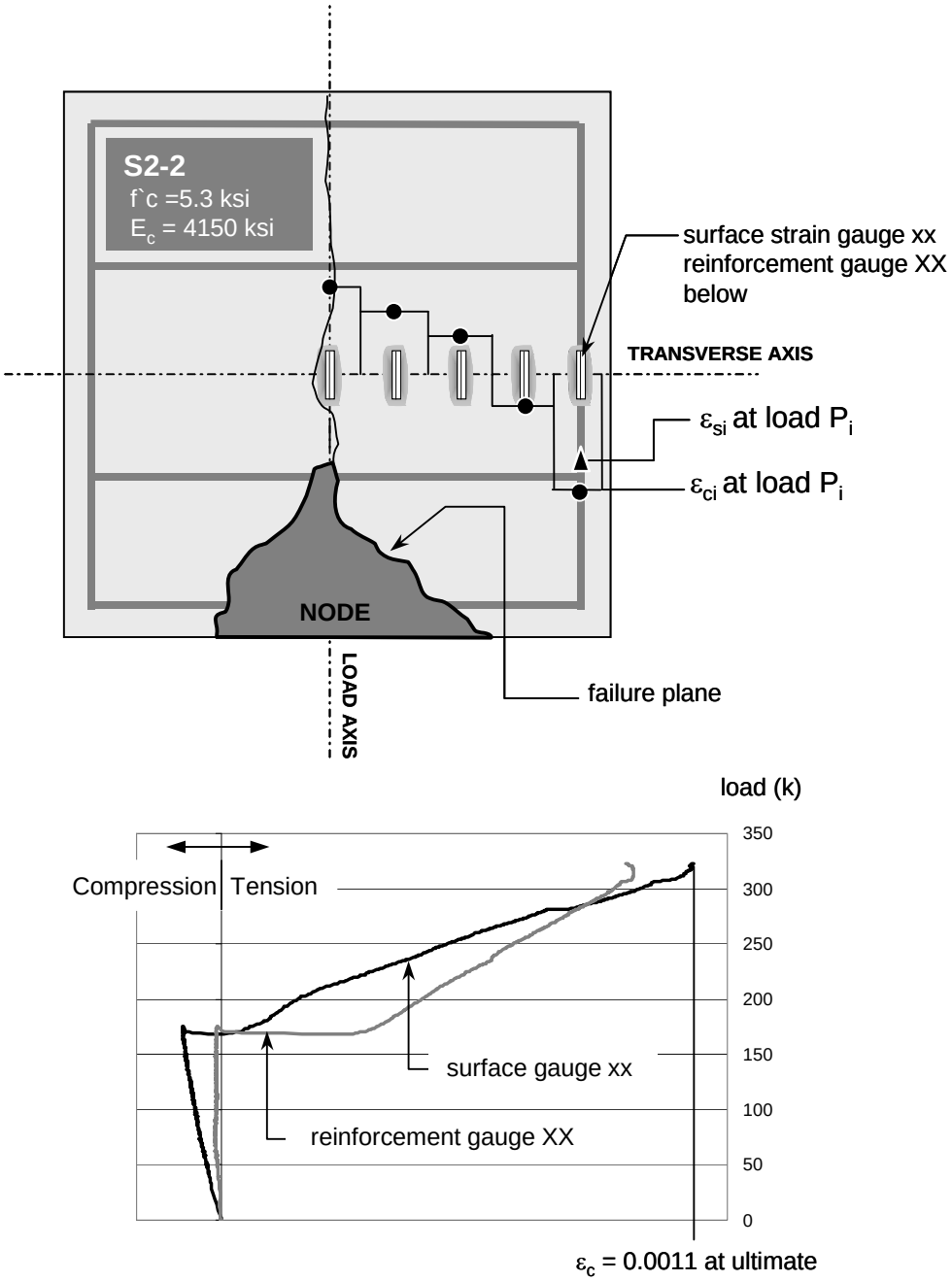

Figure 4.20 Tensile Strain Developed In Specimen S2-2

The constitutive relationship chosen to convert strain into concrete stress needed to account for these large tensile strains developed at the outer edge of unconfined specimens.

Three distinct constitutive relationships were considered for the tensile stains developed in the concrete specimen; the first assumed that no tensile stress could develop after cracking; the second assumed that a reduced tensile stress could develop after cracking but would significantly decrease with increasing crack width; the third assumed a modification of the first, in that, tensile strains could develop in the section based on the tension stiffening effect due to the vertical fabrication bar shown in Figure 4.20, if present.

The constitutive relationship shown in Figure 4.21 C was deemed most suitable for the purpose of approximating the stress distribution across the centerline of the specimen. In order to employ the tensile side of the constitutive relationship a value of $f`_t$ must be considered that models the tensile stress field at the outer edge of the specimen. Since there is a definite strain gradient form the centerline to the edge of the specimen a value closer to the modulus of rupture is more pertinent than the uni-axial tensile strength. No modulus of rupture tests were performed; however, split-cylinder tests were used to find the tensile strength of the concrete used in the specimens. The average split-cylinder strength from the three batches of concrete averaged 0.11f'c. The average compressive strength of the four batches of concrete was 4.5 ksi. 7.5 times the square root of the average compressive strength equals

0.11f`c (code value for tensile strength). A value of f`t = 0.10f`c was chosen for the limiting tensile stress.

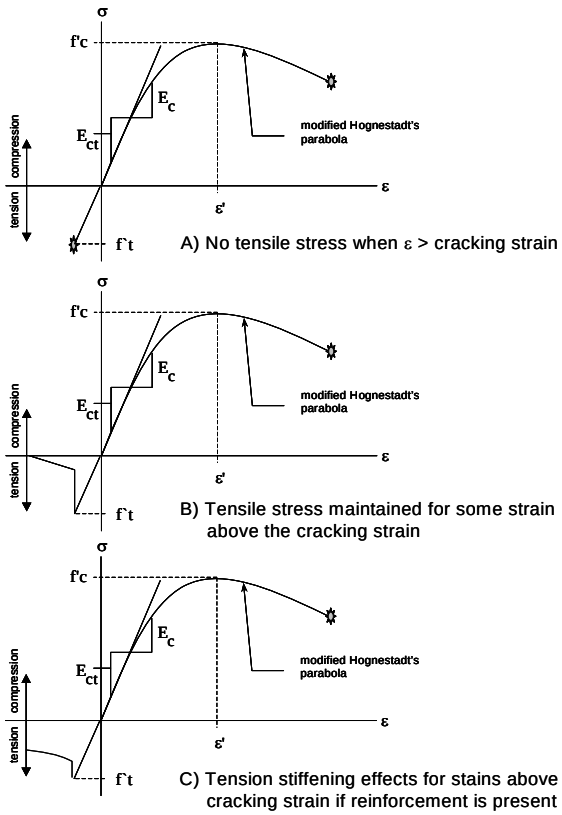

Figure 4.21 Constitutive Relationships Considered for Concrete

Once the parameters of the constitutive model were chosen, the data recording from the strain gauges on the concrete surface were converted to stresses, normalized with respect to the stress under the bearing plate, and plotted against the distance at which they occur from the centerline of the specimen normalized with respect to half the bearing plate dimensions. This normalization of both axes allows for direct

comparison of the stress fields at the centerline of the panel at different load stages under different geometric loading conditions. The stress fields at the centerline of the panel at a load equal to 90% of the cracking load of each specimen is shown in Figure 4.22 and Figure 4.23 as a second order regression of the data points separated by geometric loading conditions.

The normalized stress integrated over the normalized distance form centerline should theoretically equal 1.0 for planar specimens. Figure 4.22 and Figure 4.23 show the integration for each geometric category. The deviation of the integration from 1.0 is a measure of accuracy of the constitutive model in the elastic range. The constitutive model over predicts the stress at the centerline for Group III, and this may be due to the limited amount of data for that group. Group IV specimens include S3-9 and S3-10 whose behavior is three dimensional, and it is likely that the stress does not remain constant over the thickness. For the three dimensional nature of these specimens the integration of surface stresses is an ambiguous figure but should be less than the integration of surface stresses for planar specimens as the intensity of compressive stress diminishes through the thickness of the specimen toward the surface.

The same process for normalizing stresses was carried out for a load equal to 90% of the ultimate load and shown in Figure 4.24 and Figure 4.25. A regression analysis of the data was provided to reflect an “average value” within the group. The order of the polynomial that describes the regression line was chosen that best fits the trend of the data. In some cases the trend was linear and parabolic in others.

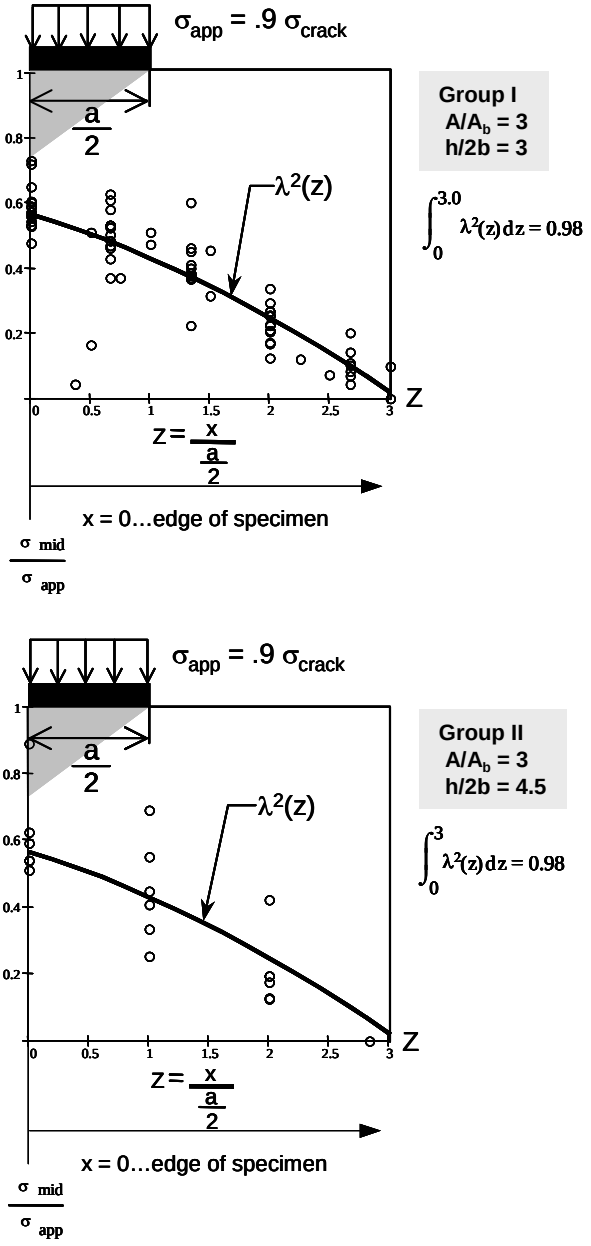

Figure 4.22 Normalized Stress at Mid-height of the Specimen in the Elastic Range

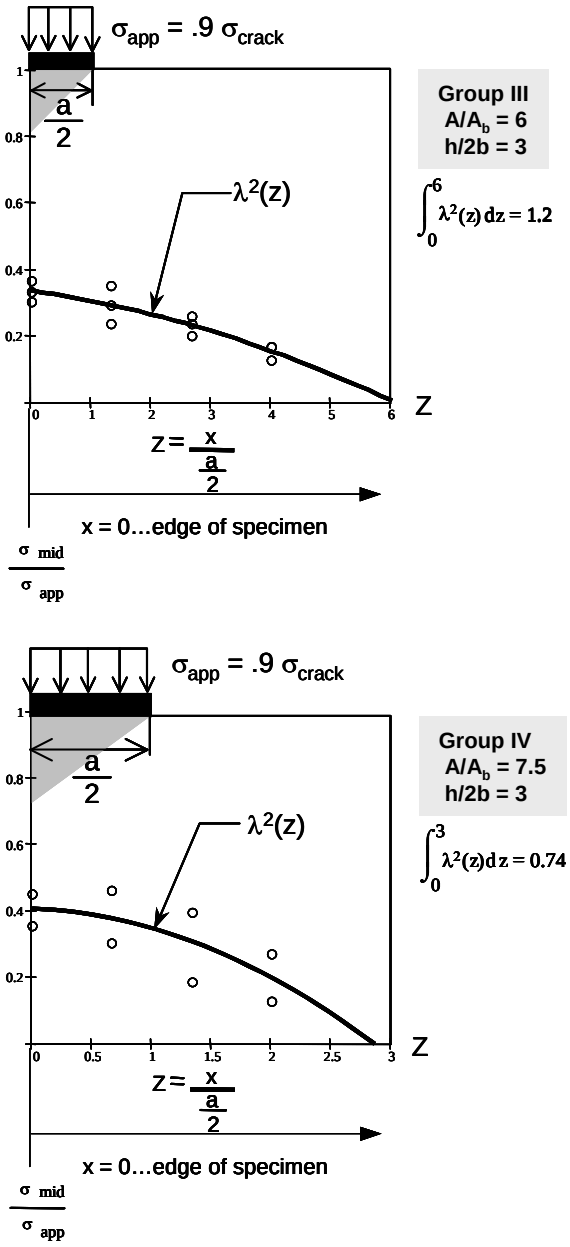

Figure 4.23 Normalized Stress at Mid-height of the Specimen in the Elastic Range Cont.

The integrated stresses over the normalized distance from centerline ranged from 0.74 to 1.3 with an under prediction occurring for unconfined specimens and over predictions for the Group III specimens. This would indicate that the constitutive model did not capture the behavior of the stress field after redistribution as well as in the elastic range. This should be expected, because the exact tensile stress is difficult to capture past cracking. Figure 4.24 and Figure 4.25 also display the difference in the stress distributions at the centerline for confined and unconfined specimens.

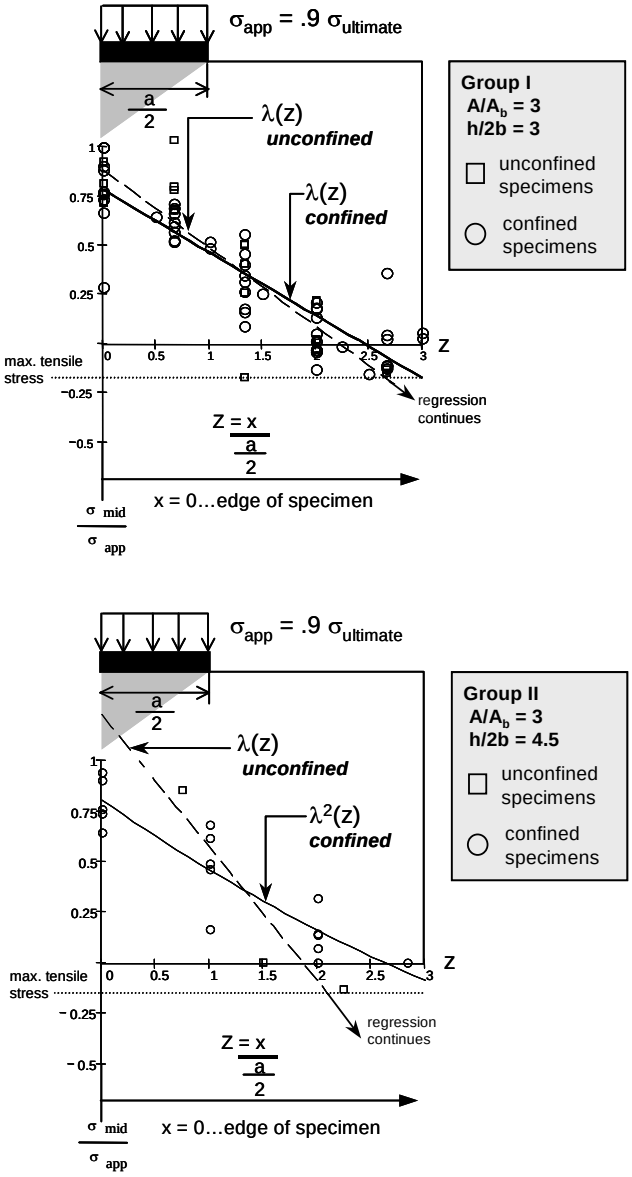

Figure 4.24 Normalized Stress at Mid-height of the Specimen after Redistribution

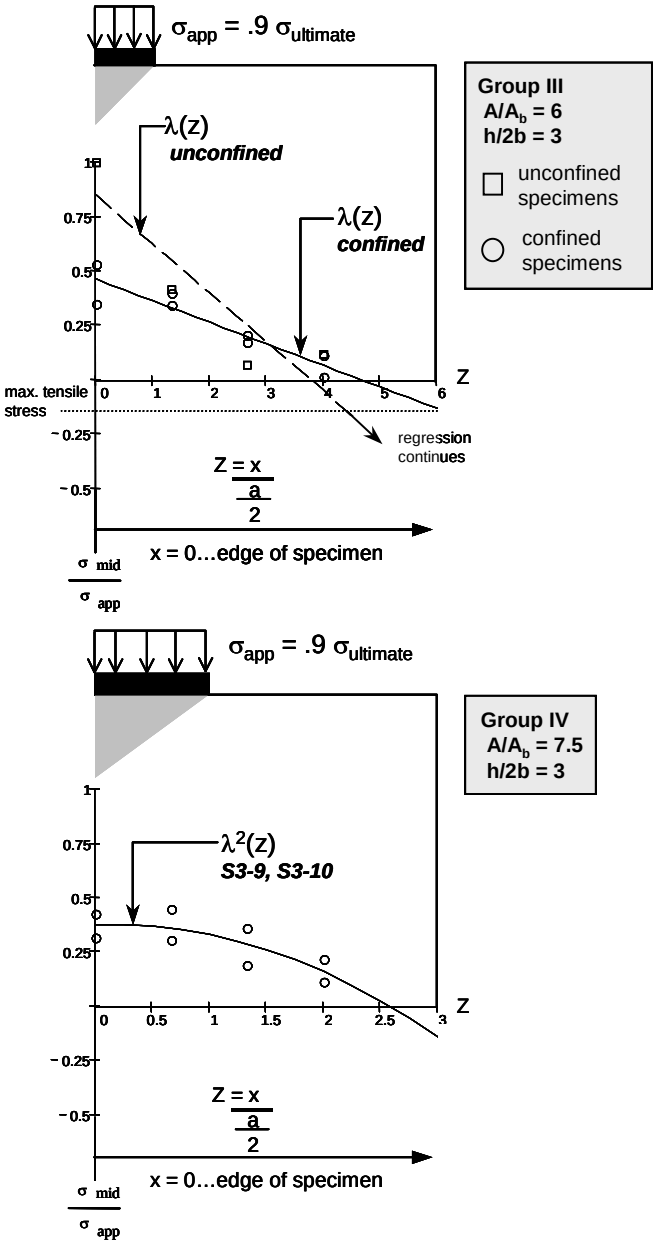

Figure 4.25 Normalized Stress at the Centerline of the Specimen after Redistribution Cont.

The gradient of the stress distribution of confined specimens is less then the gradient of the stress distribution of unconfined specimens ultimately contributing to larger tensile stress at the edge of the specimen. The spread of compressive stresses can be taken as the ratio of the distance from the edge of the bearing plate (1) to the point where the regression line crosses the distance axis divided by the half the height of the specimen normalized with respect to the half the bearing plate dimension. These ratios are displayed in Table 4.1.

Table 4.1 Spread of Compressive Stress

Group	Failure mechanism		Angle
	confined	unconfined	
GROUP I	X		1:2
GROUP I		X	5:12
GROUP II	X		7:12
GROUP II		X	4:15
GROUP III	X		5:8
GROUP III		X	11:24
GROUP IV		X	8:15

The ratios shown in Table 4.1 convert to angle between 14 degrees and 32 degrees. The steepest angle is that of the Group II unconfined specimens of which there were three specimens that exhibited an unconfined failure mechanism, two of which had confining reinforcing at the node which altered the stress distribution at the centerline of the

specimen and therefore were not included. The exclusion of specimens S2-4 and S1-5 left only specimen S1-2 which contained no reinforcing. The steep angle is consistent with amount of reinforcement present in that the angle tends toward zero with respect to vertical as the amount of reinforcing steel provided decreases. In general, specimens with sufficient reinforcement to produce a confined failure of crushing at or around the nodal area had a characteristic spread of compression at a rate of 1 horizontal unit to 2 vertical units or larger. Unconfined specimens exhibited a slightly smaller spread of compressive stresses leading to greater tensile stress at the outer edge of the specimen. This variation between confined and unconfined specimens stayed constant between geometric groups; however, as the ratio of the loaded surface to bearing plate increased in Group III the spread of compression also increased.

4.5.1 Summary of Results Obtained from Strain on the Concrete Surface of the Specimens

The stress distribution across the centerline of a specimen was reasonably attainable with limited amounts of concrete surface gauges placed at regular intervals along the centerline of the specimen. The stress distribution across the centerline depended on the load stage considered, the amount of reinforcement provided and the geometric conditions of loading. At load stages after cracking, tensile stresses developed at the edge of the specimen and the stresses were greater in specimens that exhibited an unconfined failure mechanism of a tensile failure at a plane further away from the node than the confined failure of

crushing of concrete at and around the nodal area. The spreading of the compressive stress varies by the geometric conditions of loading and the reinforcement provided; however the spread may reasonably be assumed at a rate of 1 horizontal unit to 2 vertical units as depicted in Appendix A of the ACI 318-02.

5.0 Analysis of the Results and Conclusions

5.1 Describing the Behavior with Empirical Methods

As mentioned in Chapter 4, specimens analogous to those fabricated in the experimental program described in Chapter 3 have been investigated by many researchers [11], [13], [14], [21], [22], [34], [35], [36], [39], [44], [50]. The result of many of these investigations has been the development of empirical relations based on regression analyses of the parameters considered in each investigation. For example Niyogi [34] presented an equation for the bearing capacity as a function of the ratios of bearing plate dimensions to that of the adjacent dimensions of the loaded surface. Roberts [39] used a semi-empirical equation to describe the behavior of specimens in which the loaded area was smaller than that of the supporting surface and included an empirical term as well as a term describing the behavior of confined concrete in the presence of rectangular ties or spirals. An empirical relationship for the bearing capacity of the specimens tested in the experimental program reported here is also reported in this chapter.

The main parameters affecting the behavior of the specimens tested were: the amount of reinforcement provided, the ratio of the cross-sectional area to that of the bearing plate area (A/A_b), and the height of the specimen to that of thickness of the specimen (h/2b). As seen from Figure 4.7, the width of the compression field at the centerline of the specimen was a function of the amount of reinforcement provided. Relating the width of the compression field at midheight of the specimen (which is dependent on the amount of reinforcement provided) to the area

of the loaded surface indirectly combines two parameters. An empirical equation was produced from regression analyses of the parameters mentioned previously and a comparison of the regression analyses to the test results is illustrated in Figure 5.1. Figures 5.2 and 5.3 compare the empirical equation presented by Niyogi [34] and semi-empirical equation presented by Roberts [39] to the test results. The efficiency factor of concrete defined as the ultimate stress under the bearing plate normalized to the compressive strength of concrete (ν_e) is the parameter by which the comparison of empirical equations to test results was made.

It can be seen by Figures 5.1, 5.2, and 5.3 that empirical equations correlate quite well in some instances and rather poorly in others. The variation is due to the fact that the empirical relations are modeled after a specific set of specimens and geometric loading conditions beyond which the parameters used in developing the empirical relations may not be directly applicable.

It was not the intent of this research project to develop empirical relations for the bearing capacity of concrete specimens loaded over a limited surface area; however, empirical relations and comparisons with the test data are presented here to illustrate an important point: strut-and-tie models can be used to describe the behavior of concrete elements that have previously been unexplainable by classical methods of analysis.

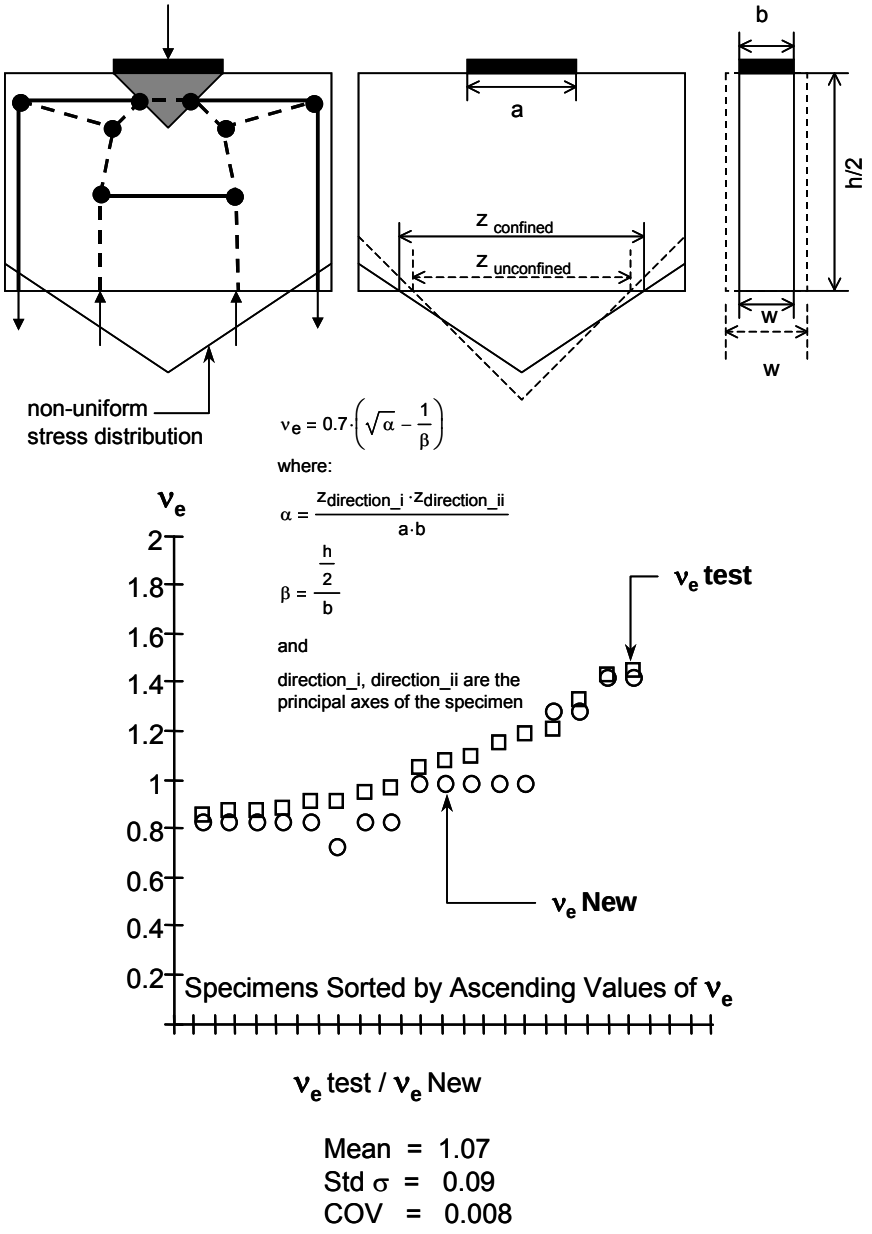

Figure 5.1 Empirical Relationship Developed for the Test Specimens in This Investigation

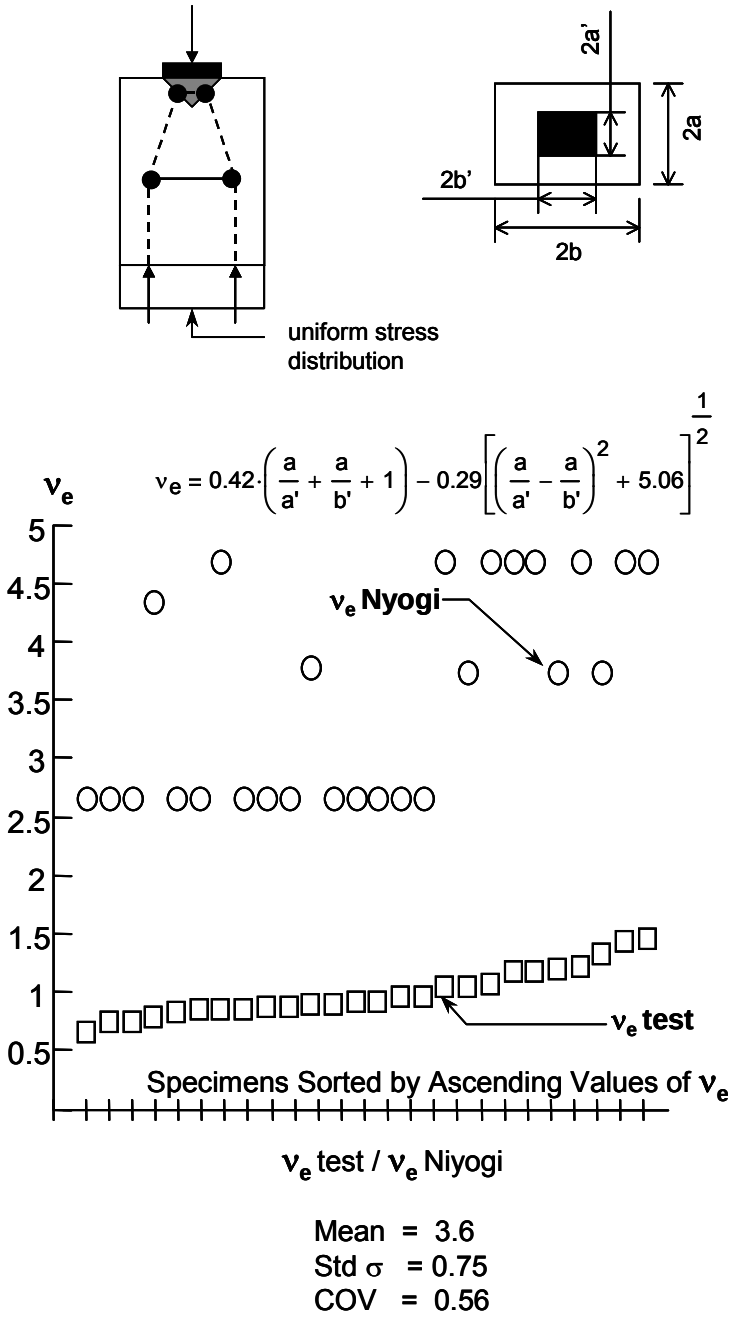

Figure 5.2 Empirical Relationship from [34] and Comparison to Test Data

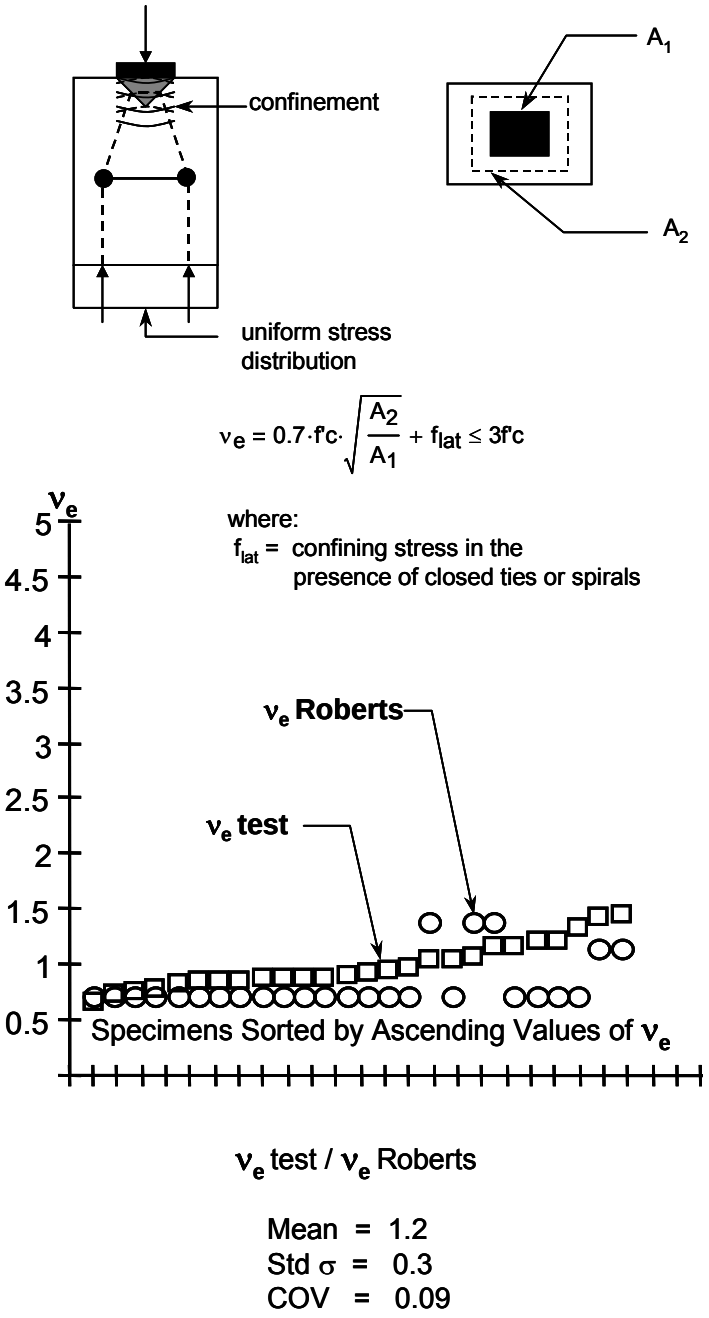

Figure 5.3 Semi-Empirical Relationship from [39] and Comparison to Test Data

5.2 DESCRIBING THE BEHAVIOR WITH STRUT-AND-TIE MODELS

Strut-and-tie models were used to describe the stress fields created within the specimen at various load stages. These models provided insight into the redistribution of stresses and the mechanics of failure for these simple specimens. Typical models at various load stages are illustrated in Figure 5.4. The introduction of applied stress creates

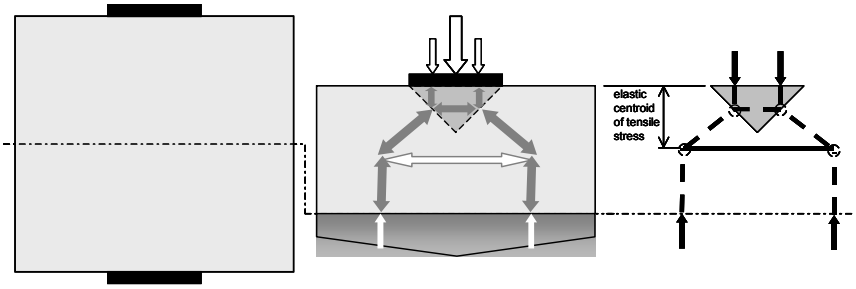

A) Elastic Range $P < P_{crack}$

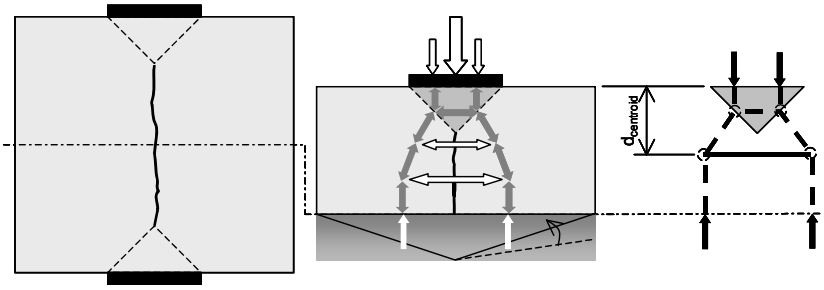

B) Immediately after Cracking; Reinforcement Engaged

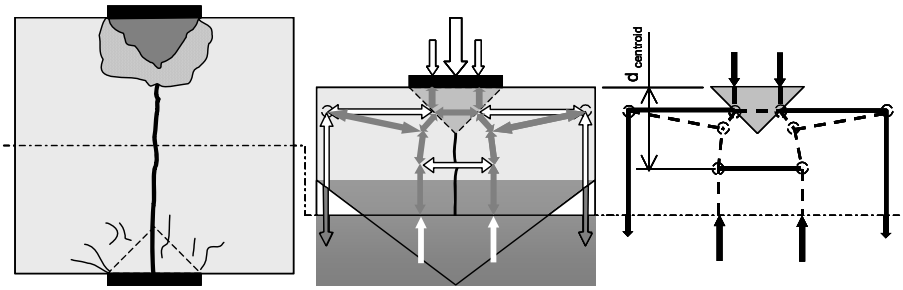

C) Increasing Stress Until Failure at the Node

Figure 5.4 Typical Strut-and-Tie Models at Various Load Stages

a region of biaxial compression in planar elements and tri-axial compression in three-dimensional elements directly under the bearing plate. In reality no structural concrete members are truly planar and have some finite thickness in the third dimension leading to a tri-axial state of compression at the midpoint of the thickness of the element, which gradually reduces to a state of biaxial compression at the surface of the element. Such nodal regions are commonly referred to as hydrostatic nodes and to satisfy equilibrium, stresses perpendicular to the applied stress must equal the applied stress. The equilibrium of sresses geometrically forms an isosceles triangle with a height equal to half the width, of which, the stresses are equal on all sides. The geometry of these nodes was continually substantiated by the geometry of the intact concrete under the bearing plate of the specimens within the experimental program. As a result of the stress state within the nodal region, compressive stresses propagate from the node initially at 45 degrees. To satisfy equilibrium, elements at the interior of the specimen, defined as the region enclosed by a line drawn at 45 degrees from the edge of the bearing area to the edge of the specimen, are subjected to some degree of transverse tensile stress as shown in Figure 5.5.

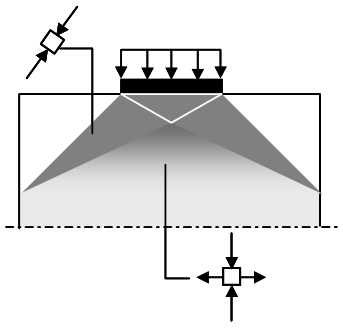

Figure 5.5 Stress Fields for a Typical Specimen Adapted from [33]

Once the specimen cracks, the transverse stiffness provided by the uncracked concrete in tension disappears, and a significantly reduced stiffness provided by the reinforcement replaces the initial concrete stiffness. The net effect is the movement of the centroid of compressive stresses to the centerline of the section.

Consider a free-body diagram composed of one symmetrical quadrant of an uncracked specimen (Figure 5.6 A). The stress present at the vertical face of the hydrostatic node is equal to the bearing stress and is also equal to the tensile stress developed within the concrete plus a negligible amount of tensile stress provided by the reinforcement. The struts anchoring the tension in the concrete and the tension in the reinforcement must provide a force equal the resultant of the compressive stresses at the horizontal and vertical faces of the node. Summing the moments about point X in Figure 5.6 A yields a system of nonlinear equations with two unknowns which are the angles θ and ϕ. There is no unique solution to this system of equations. Each solution will result in the same stress distribution across the mid-height of the panel depending on the tension force assigned to the reinforcement. However, some solutions are more suitable than others. Solutions that result in angles of ϕ that deviate strongly from the elastic stress distribution, as well as, solutions that that result in the concrete tension component being much larger than the tension capacity of concrete calculated by the area of concrete extending from the node to the midheight of the section should also be avoided. The elastic strut-and-tie model shown in Figure 5.6 A) is the culmination of two sub-models that divides the load carried by each sub-model based on the angle θ chosen from the range of possible solutions.

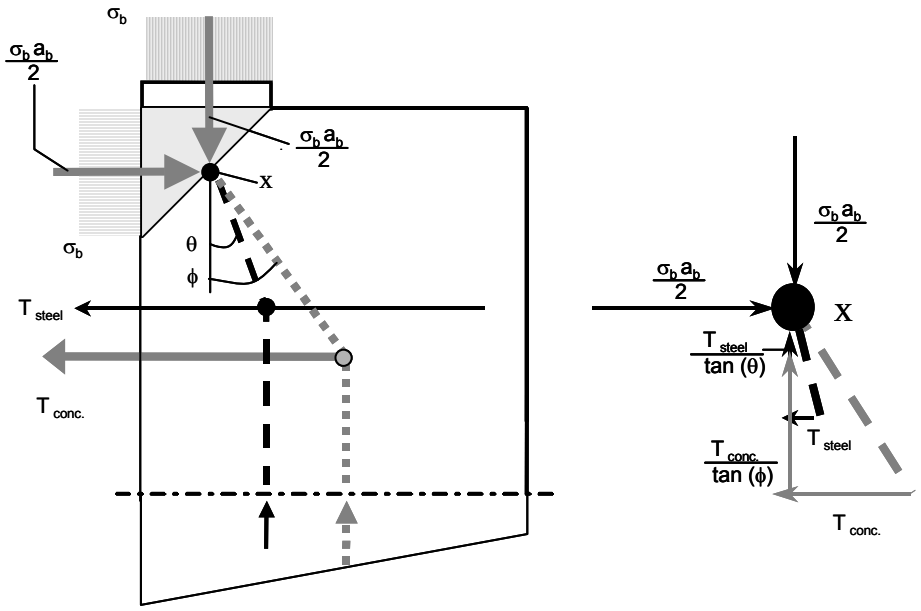

A) Strut-and-Tie Model for an Uncracked Section

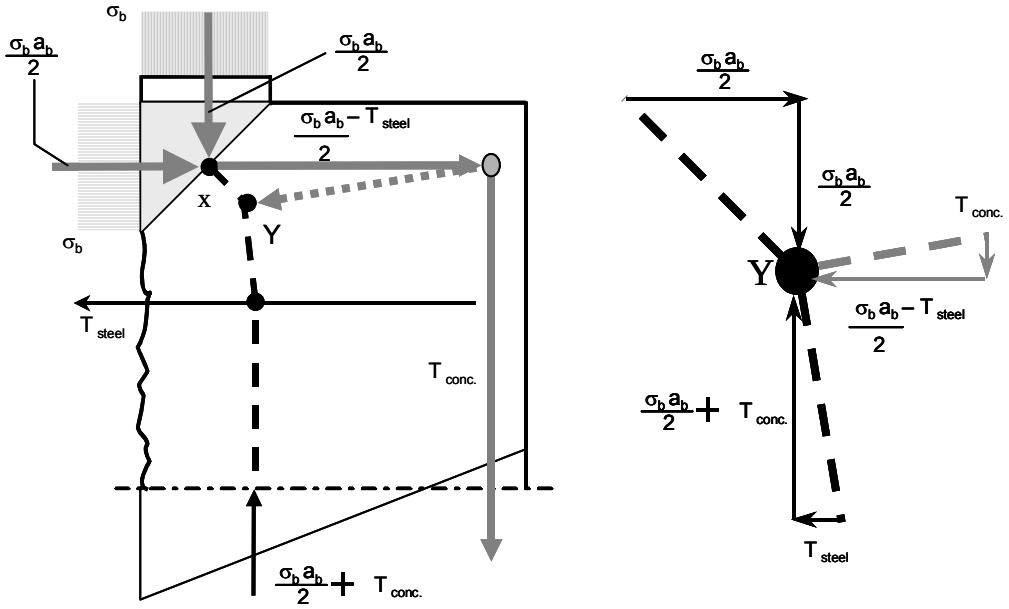

B) Strut-and-Tie Model for an Cracked Section

Figure 5.6 Strut-and-Tie Models for Cracked and Uncracked Sections

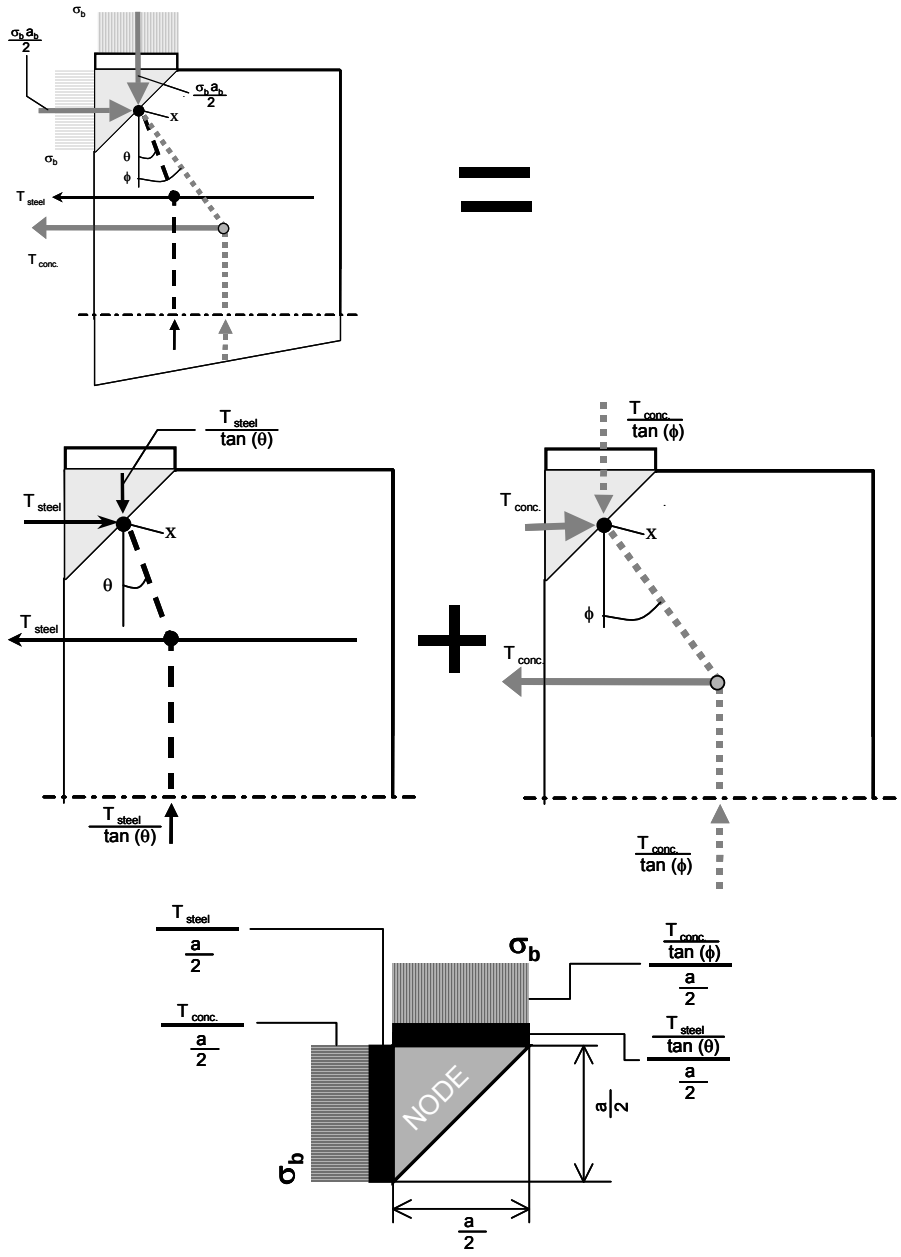

Figure 5.7 Separation of Sub-Models in the Elastic Range

The strut-and-tie model for the elastic range as stated previously will produce different stress distributions across the midheight of the specimen dependent on the tensile force assigned to the reinforcing bars crossing the vertical crack. The difference in stress distribution at midheight of the specimen dependent on the amount of reinforcement provided is substantiated by comparing specimens with relatively large amounts of reinforcement (confined specimens) to unconfined specimens under the same geometric conditions of loading as shown in Figure 5.8.

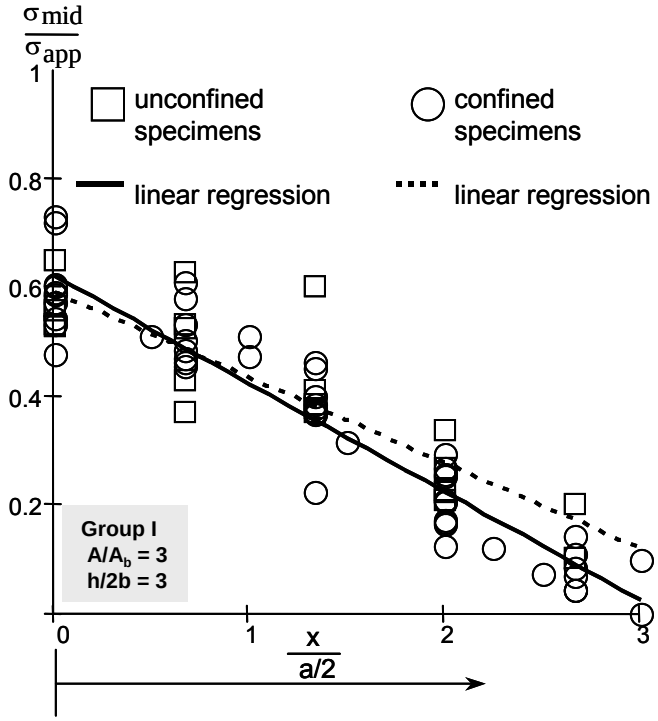

Figure 5.8 Stress Distribution of Group I Specimens in the Elastic Range

Furthermore, specimens tested with smaller bearing plates cracked at higher loads compared to specimens with the same amount of reinforcement and larger bearing plates. The increase in capacity is due

to the increase of the concrete tensile component created from reducing the size of the node.

Once the section cracks, the strut-and-tie model changes significantly as displayed in Figure 5.6 B. The concrete tensile component disappears yet the compressive stresses at the vertical face of the node are still present. The loss of the concrete tensile capacity results in large tensile stress fields at the edges of the specimen which are modeled as tensile forces parallel and perpendicular to the load applied. The tensile stresses at the edge of the specimen act normal to the plane of the model shown in Figure 5.6 B within the thickness of the specimen causing splitting failures as seen in the specimens tested and shown in Figure 4.6. Anchoring the splitting forces is a strut whose magnitude is determined by the tensile forces at the top face and side face of the specimen. A numerical example of producing a typical strut and tie model including the tensile forces at top edge and side edge of the specimen is presented in Figure 5.9. The splitting forces developed within the specimens are analogous to other structural elements where a force couple is not present to restrain the compressive stresses of the vertical face of a singular node. Two examples of the splitting force being restrained by force couples are the uncracked specimen in Figure 5.6 A where the compressive force is resisted by the tensile force in the concrete and a node in the compression zone a beam where the stress at the vertical face of the node is resisted by the force couple due to bending.

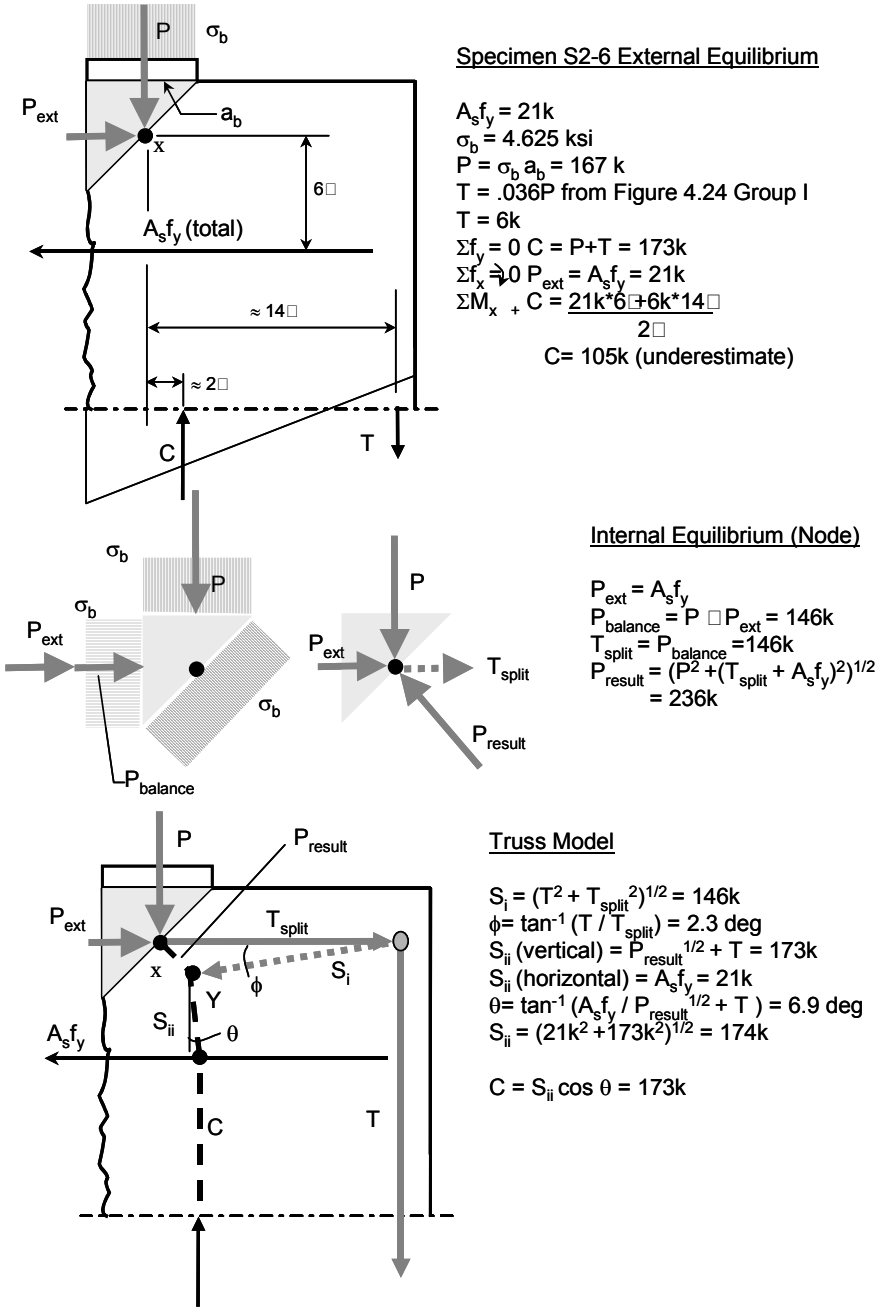

Figure 5.9 Numerical Example of a Typical Strut-and-Tie Model

Muttoni [33] shows one such example of splitting forces in the case of a pre-tensioned beam shown in Figure 5.9.

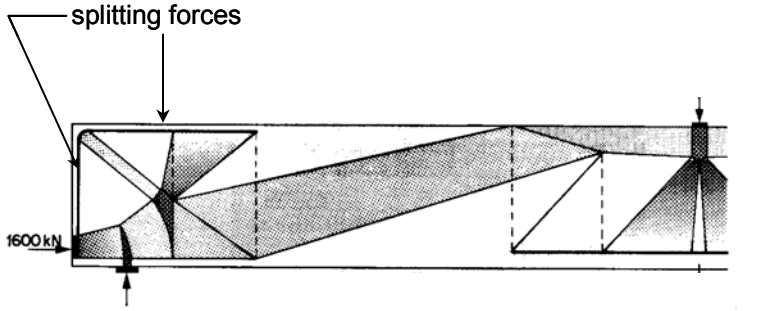

Figure 5.10 Splitting Forces within a Pre-Tensioned Beam from [33]

Sanders [44] did not include the splitting forces shown in Figure 5.9 in the models he proposed for his anchorage specimens which were present in the specimens in which a crack propagated to the base negating the uniform stress distribution assumed within the models, instead, he based his models solely on the reinforcement within the section as shown in Figure 5.11. Sanders' models were conservative and provided good correlation with the test data gathered within his experimental program; however, his models did not reflect the behavior of unreinforced specimens.

The strut-and-tie models presented followed Schlaich's [46] approach which assumed that sub-models could be created that divided the load in any manner desired by the designer with the caveat that equilibrium most be satisfied. The strut-and-tie model presented for the cracked section split the force applied to the vertical face of the node into two components; one consisted of the force couple of the tension steel, while the other component was the remainder of the force at the node transferred into a splitting tension as shown Figure 5.12.

$$\tan(\alpha) = \frac{\frac{h}{4} - \frac{a}{4}}{d_{centroid} - \frac{a}{4}}$$

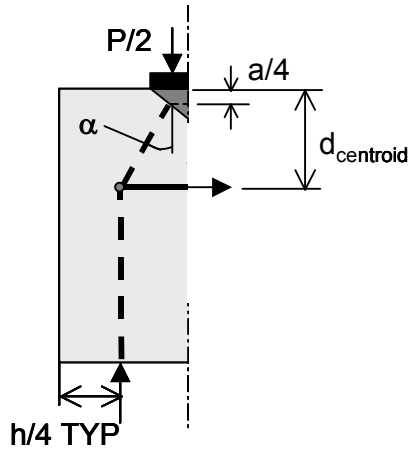

A) Sanders' Strut-and Tie Models Used for End Anchorage Specimens

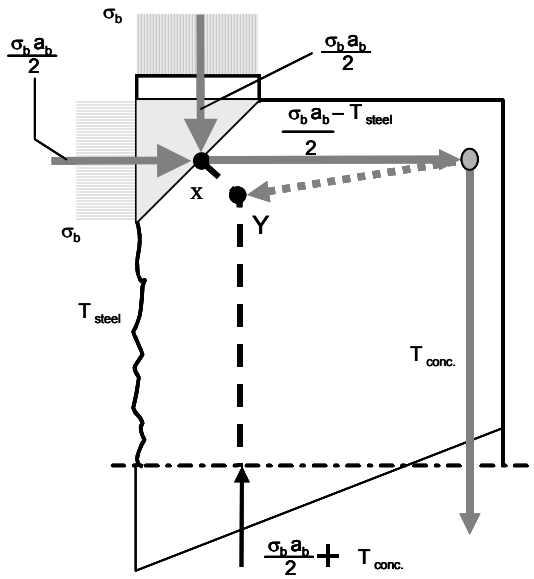

B) Strut-and-Tie Model for an Unreinforced Specimen

Figure 5.11 Comparison of Strut-and-Tie Models with [44]

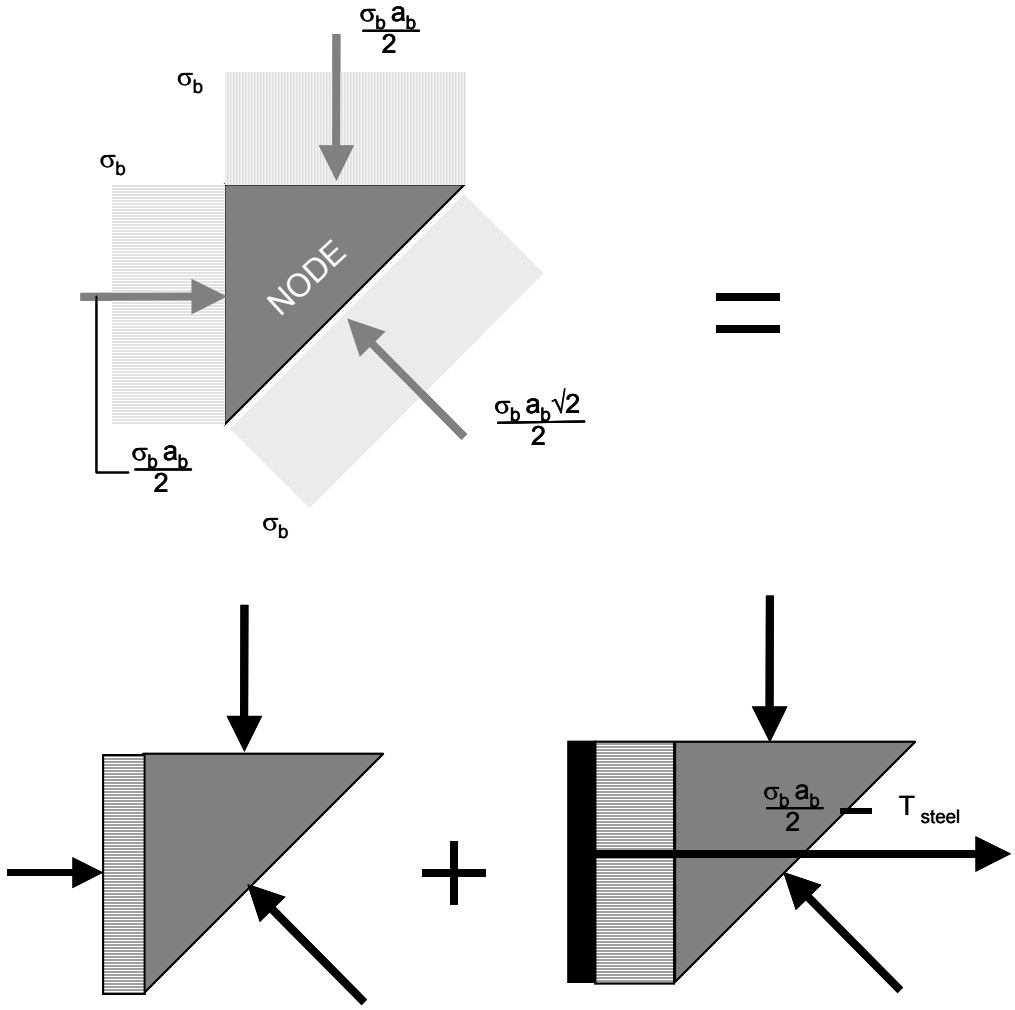

Figure 5.12 Force at the Vertical Face of the Node Split into Two Components

The strut-and-tie model for the uncracked specimen showed a similar sub-division of the load by separate models. Schlaich's [46] idea was experimentally substantiated by Maxwell [29] and again by Chen et al [18]. The elegancy of strut-and-tie models resides in the ability to subdivide the load a any manner possible as long as equilibrium is satisfied. The fault of

STM is not in the modeling itself but in the subjective choice of failure criteria for the elements within the strut-and-tie model to ensure plastic behavior.

5.3 ANALYSIS OF THE STRUT-AND-TIE MODELS

In order to distinguish between different types of behaviors and to make comparisons, a strut-and tie model was created and analyzed for each specimen. To accomplish this task the stress distribution across the midheight of each specimen at the ultimate conditions was obtained from the data collected from the surface gauges in the experimental program. The strains were converted to stresses using the constitutive relationship described in Chapter 4. Plots similar to those in section 4.4 were produced excluding the regression analyses. Interpolated values of the stresses calculated were used to predict the stresses across the midheight of the section where no data was available. The interpolation consisted of splines between known points containing parabolic endpoints. The tensile stresses were integrated across the midheight of the specimen dictated by the constitutive relationship on the tensile side. The portion of the entire load that was assigned as a tension value, the average force in the reinforcement at ultimate, and the ultimate load placed on the specimen were then used to create the strut-and-tie models. This process is shown in Figure 5.13 A and B. A measure of the accuracy of the tensile force at the edge of the specimen, and hence the entire model, was made by comparing the location of the compressive stresses calculated by the model to the centroid of the compressive stresses given by the parabolic spline interpolation. The comparison is shown in Figure 5.13 C.

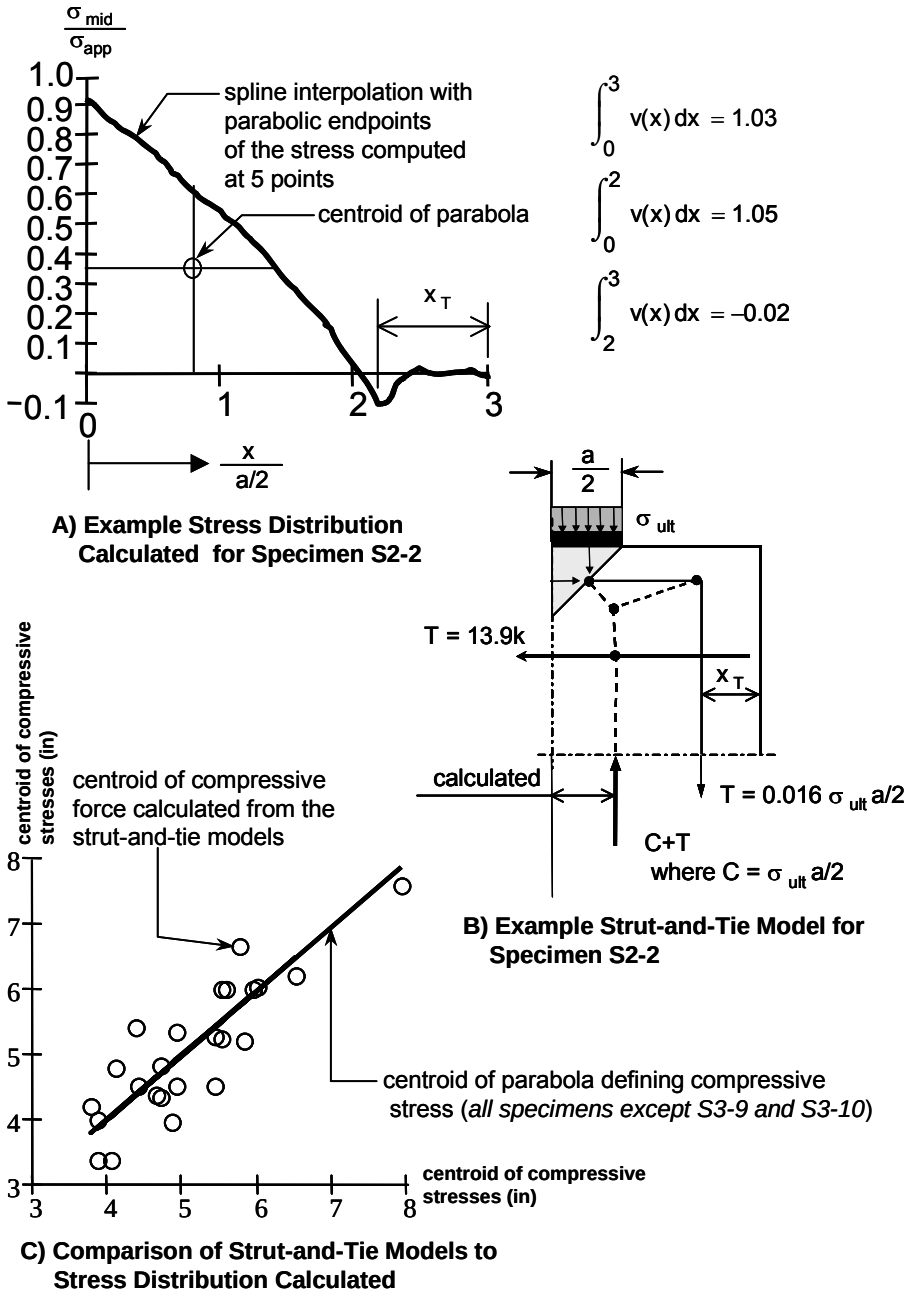

Figure 5.13 Production of the Strut-and-Tie Models for Each Specimen

The mean difference between the centroid of the compressive stresses calculated by the model and the centroid of compressive stresses given by the stress distribution was .44 inches with a standard deviation of 0.3 inches. These values indicate that the tensile forces at the edge of the specimens were calculated fairly well in light of the fact that capturing the tensile stress in concrete is extremely difficult due to factors mentioned in section 4.6.

The result of the analysis shows that the type of failure mechanism associated with each specimen has a strong correlation with the location of point Y in Figure 5.6 B. Unconfined failures are typified by larger distances of point Y from the singular node, or in other terms, a longer strut length S_{iii} as shown in Figure 5.14. As the percentage of steel increased, the length of strut S_{iii} steadily decreased edging closer and closer to the singular node. The length of the critical strut S_{iii} was dependent on the angle of the strut that anchors the deviation of the splitting force around the corner of the specimen as shown in Figure 5.9, and the relative distance from the node to the anchoring point of the tensile forces (d_T/a_b in Figure 5.14). As the steel yields the steel force remains nearly constant; however the horizontal splitting force increases linearly with the stress applied due to the modeling assumptions shown in Figure 5.12; the tensile force along the vertical edge of the specimen to increases with the load applied, but at a smaller rate than the horizontal tensile force. The difference in the increase of tensile forces at the edges of the specimen result in smaller values of the tangent of ϕ shown in Figure 5.14. The splitting failure observed in the heavily reinforced

specimen could be a result of a compatibility failure as the strut begins to orient itself on top of the horizontal tensile tie.

The comparison of strut-and-tie models between specimens that were loaded through different sizes of bearing plates, yet had the same percentage of reinforcement shows the same trend as the comparison between specimens of differing reinforcement percentages as shown in Figure 5.14. The length of S_{iii} in specimen S3-4, and S3-7, which were loaded with 6 inch by 6 inch bearing plates, was considerably smaller than the lengths of S_{iii} of the strut-and-tie models for specimens S2-3 and S3-3 which had exactly the same reinforcement percentages but were loaded with 6 inch by 12 inch bearing plates.

The overall analysis of the strut-and-tie models showed trends only with out incorporating particular failure criteria. In other words, the strut-and-tie models shown in Figures 5.6 B, 5.9, 5.11 B, 5.13 B, and 5.14 were not used to predict the ultimate load for the specimen; instead these models were used to understand the behavior of the specimens throughout the loading process. The strut-and-tie models showed the distinct difference between specimens that exhibited the unconfined failure and those that exhibited the confined failure. The difference was the length of strut S_{iii} in Figure 5.14. The specimens that failed at higher values of ν_e had the shortest lengths of the strut S_{iii}. The length of this strut was dependent on the amount of reinforcement provided and the geometric conditions of loading. It can be inferred from the analysis that either the geometric conditions of loading or the amount reinforcement dictated the location of the failure plane. The failure always consisted of a strut failure substantiated by the fact that the concrete directly under the

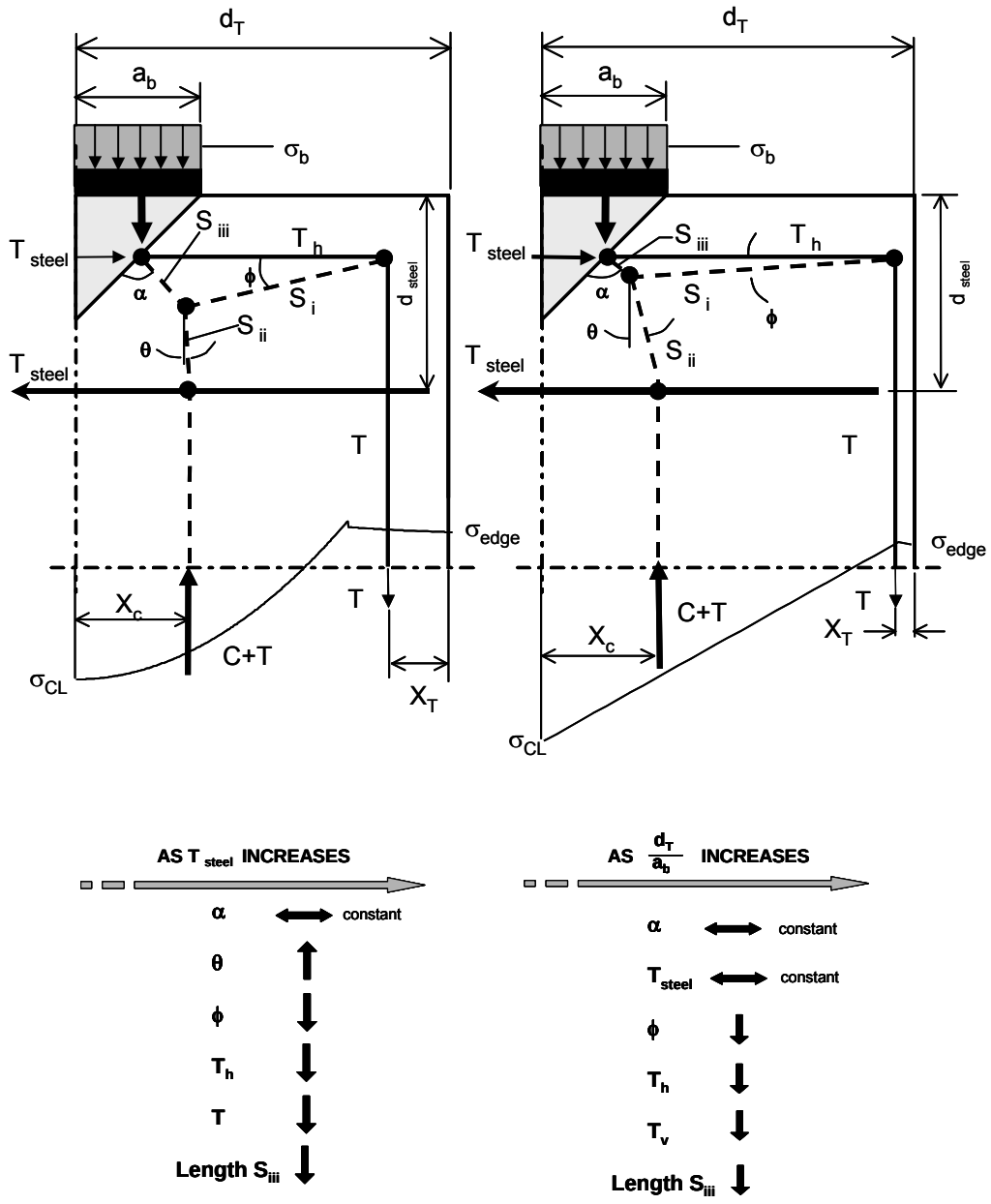

Figure 5.14 Comparison of Strut-and-Tie Models

bearing plate defining the node remained intact in every specimen tested. Based on the observations of the strut failures, in which unconfined failures consisted of cracked concrete and confined failures consisted of crushed concrete, it can be surmised that unconfined struts failed due to higher levels of bi-axial tension while confined struts failed in the presence of direct compression. For this reason the multi-axial state of stress within the concrete under the loading conditions of the specimens needed to be explored further.

5.4 Multi-Axial States of Stress and Strut-and-Tie Models

It is evident form the observations of the location and condition of the failure planes of the specimens tested coupled with the analyses of the strut-and-tie models described in the previous section that the failure mechanism associated with each specimen is a function of the state of multi-axial stress at the node-strut interface.

Figure 5.15 illustrates the state of stress of concrete elements at various distances from the loaded surface in the specimens tested. Concrete elements within the specimen are subjected to greater tensile stresses further away from the node. As the tensile stress increases on the concrete elements, the ability to sustain compressive stresses decreases. The increase of tensile stress at greater distances from the node is a plausible explanation to the observed failure mechanisms of the specimens. For unconfined failure, the failure mechanism was initiated by a ***tensile*** crack resulting in a wedge of concrete in the shape of an isosceles triangle under the bearing plate. The wedge was pushed into

the body of the specimen as further load was applied until aggregate interlock was degraded between the wedge of concrete under the node and the remaining body of the specimen. On the other hand, confined failure mechanisms consisted of a region of crushed concrete closer to the wedge of concrete in the form of an isosceles triangle under the bearing plate. Specimens that contained small amounts of reinforcement exhibited the unconfined failure while specimens with larger amounts of reinforcement exhibited the confined failure. The amount of steel provided in the specimen dictated the distance of the failure plane and the failure mechanism by restraining tensile stresses in the concrete around the node area providing the concrete the ability to fail in pure compression at the node-strut interface. Without sufficient reinforcement, the concrete would fail in tension as bi-axial states of stress controlled the failure mechanism, which occurred at planes farther away from the node. The strut-and-tie models developed in the previous section described the mechanical behavior behind the distance at which either failure plane occurred (strut length Siii in Figure 5.14) which was dependent on the amount of steel provided and/or the d_T/a_b ratio shown in Figure 5.14.

The current provisions for STM within ACI 318-02 Appendix A contain no direct provisions for biaxial stress states, and therefore will overestimate or underestimate the failure criterion for struts dependent upon the state of stress at the node-strut interface. To illustrate this point Thompson's [47] CCT node specimens are considered in Figure 5.16. The tri-axial stress state in front of the rectangular head of the headed bar is apparent form the average compressive stress in the concrete which was around 3.8 times the compressive strength at failure.

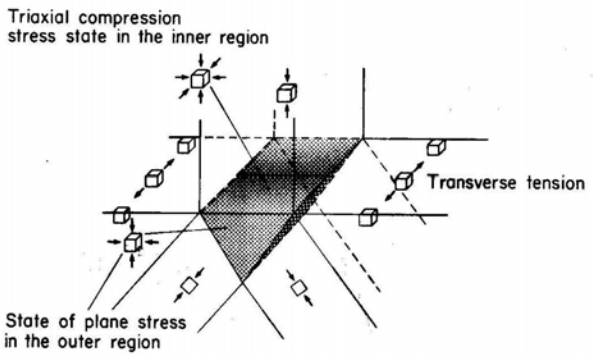

A) States of Stress for Nodal Regions from Muttoni

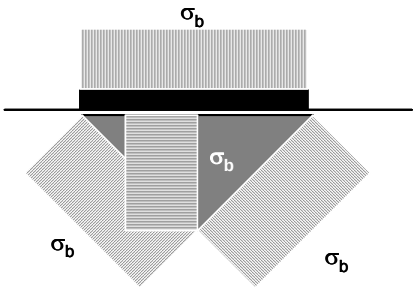

B) Planar Node

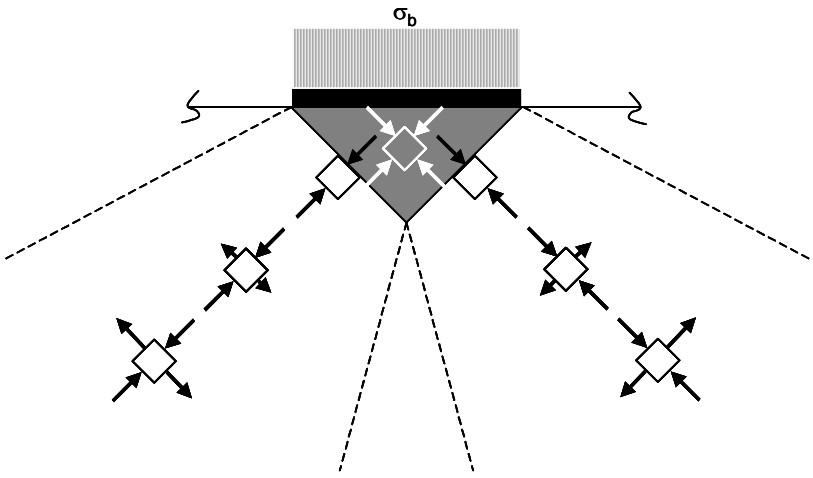

C) States of Stress in a Planar Nodal Region

Figure 5.15 State of Stress for Elements at the Nodal Region

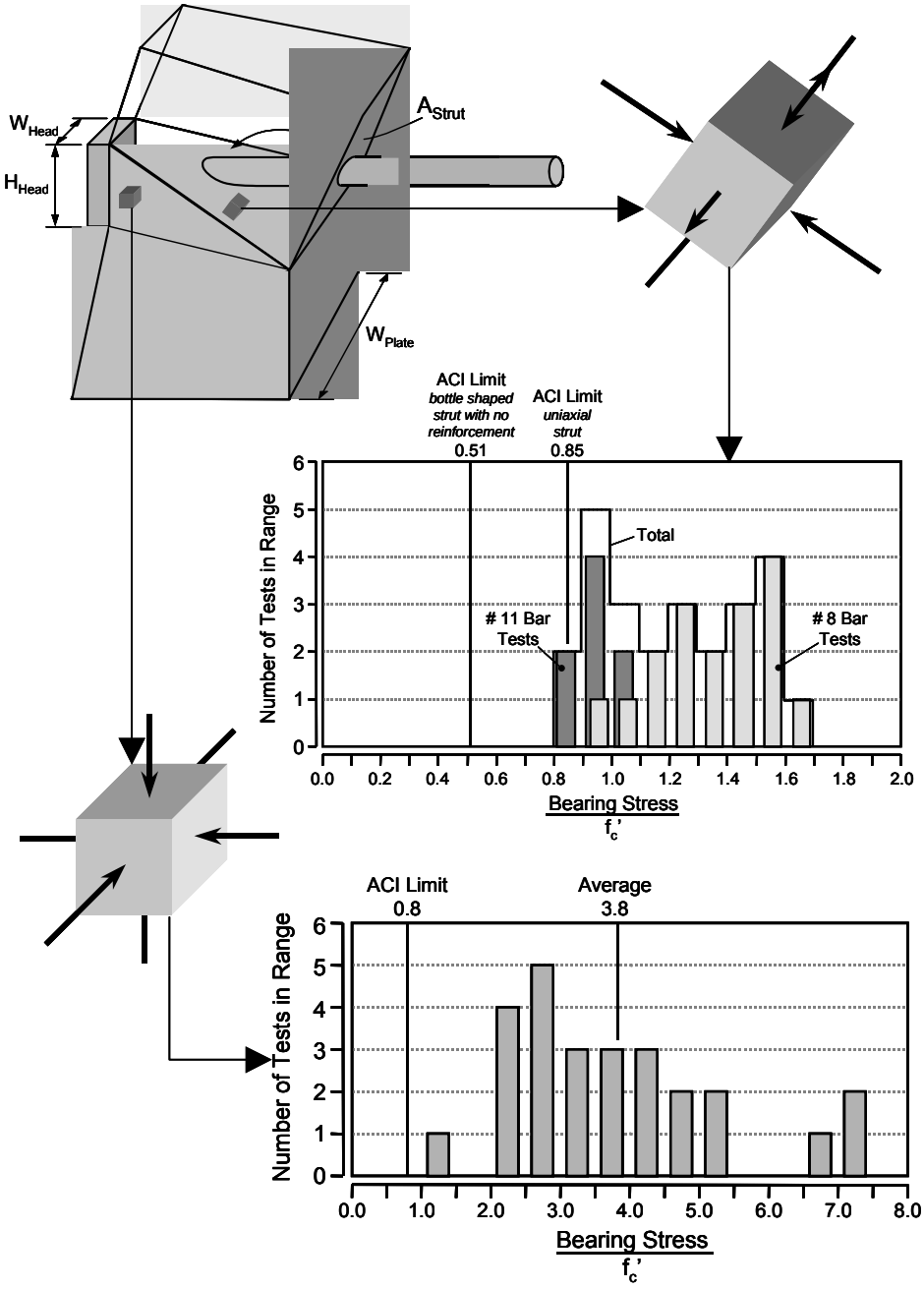

Figure 5.16 Stresses at Node Face and Node-Strut Interface from [47]

Thompson [47] shows a difference in the stresses acting at the node-strut interface for the # 8 bar specimens and the #11 bar specimens. For either bar size the areas of the heads anchoring the bars are similar, and therefore, the nodes should be of similar dimensions for either case. The similarity is due to the fact that a hydrostatic node will develop based on the most highly stressed plane which is behind the head of the headed bar. The other two planar dimensions of the node assumed by Thompson were too large to equilibrate the stresses acting behind the head of the headed bar. Figure 9 shows the actual node developed in Thompson's tests.

Figure 5.17 Node Developed in Thompon's [47] Headed Bar Tests

Even though the node-strut interfaces assumed by Thompson are larger than the actual planes of a hydrostatic node, calculated stresses for the #8 bar specimens averaged over 1.5 times the uni-axial compressive strength of the concrete used in fabrication of the specimens. The large value indicates that there were some bi-axial compressive stresses acting on these planes.

The AASHTO 5.6.3 provisions for STM include a term for a reduced compressive capacity for cracked concrete as lateral strains imposed by reinforcement increase as shown in Figure 5.18.

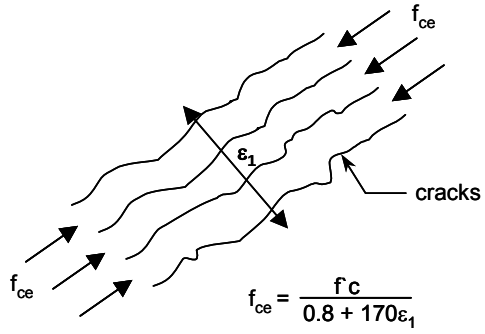

Figure 5.18 AASHTO Provision for Reduced Concrete Capacity as a Function of Lateral Strain from [41]

The expression developed by Collins et al. [30] shown here as equation 5-1

$$f_{ce} = \frac{f'c}{0.8 + 170\varepsilon_1} \qquad (5\text{-}1)$$

is not suitable as a biaxial failure criterion for bottle-shaped struts loaded through rigid plates. If sufficient reinforcement and adequate detailing is

provided that ensures ample plastic deformations, it is unlikely that an ultimate failure will occur in a cracked region such as the one depicted in Figure 5.18. Stress redistribution will continue until the stiffest element has failed in compression at the point of highest stress, which typically occurs at singular nodes. Collins' expression (5-1) was developed through testing of specimens in which the transverse strain was active, in that, transverse reinforcement within specimens was tensioned while compressive force was applied. The transverse reinforcement in the specimens tested in this investigation was strained only through deformation (passive) of the specimen after a crack through the centerline had formed and further load was applied. The transverse reinforcement in some specimens that exhibited the unconfined tensile failure mechanism was strained well beyond yield, yet the ultimate load was much greater than that predicted by equation 5-1 indicating that the role of the reinforcement was only to change the bi-axial stress condition at or around the nodal area. This point is proven by Figure 5.18 which the efficiency of concrete to sustain compressive stresses in the presence of transverse tensile strain normalized to the concrete strength predicted by equation 5-1 is compared with the failure stress of the specimens normalized to the compressive strength of the concrete of the specimens within the experimental program.

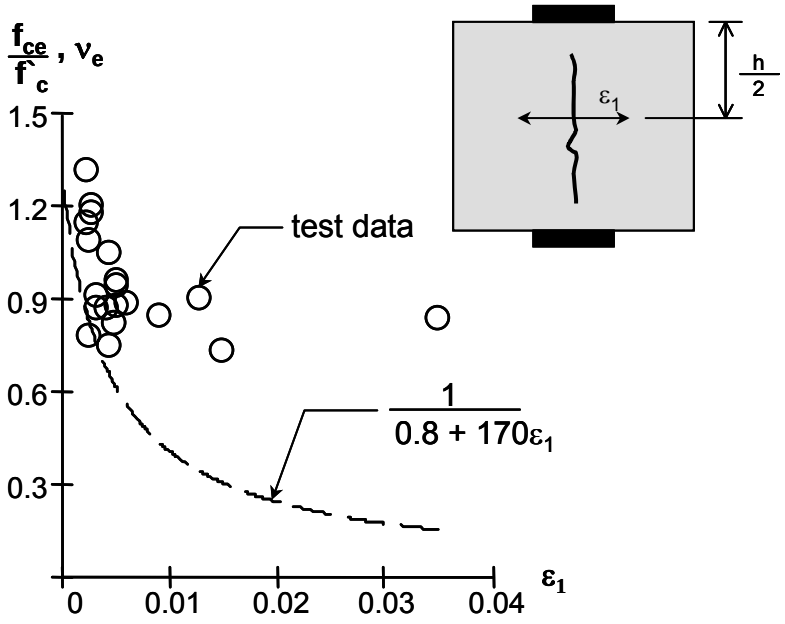

Figure 5.19 Failure Stress as a Function of Transverse Strain

5.5 THE TRANSITION STRESS FIELD

A stress field developed by M. Schlaich [46] was proposed in a brief paper in 1990 that exploits the tensile strength of concrete to create a statically admissible transition stress field between two adjacent one-dimensional stress fields of differing intensity. The transition stress field is used to satisfy equilibrium at hydrostatic nodes in the cases where one-dimensional stress fields are either larger or smaller than the design strength of the node. Figure 5.20 shows example of either case. Figure 5.20 A shows the case where the one dimensional stress field has an intensity smaller than the design strength of the node such was the case with the specimens tested in the experimental program. In order to satisfy

equilibrium at the hydrostatic node, the stress field with a smaller intensity must taper to the node. Figure 5.20 B shows the case where the incoming one-dimensional stress field must enlarge to the node. This case might occur at nodes whose design strength is reduced in the presence of tensile stresses induced by reinforcement anchored at the node.

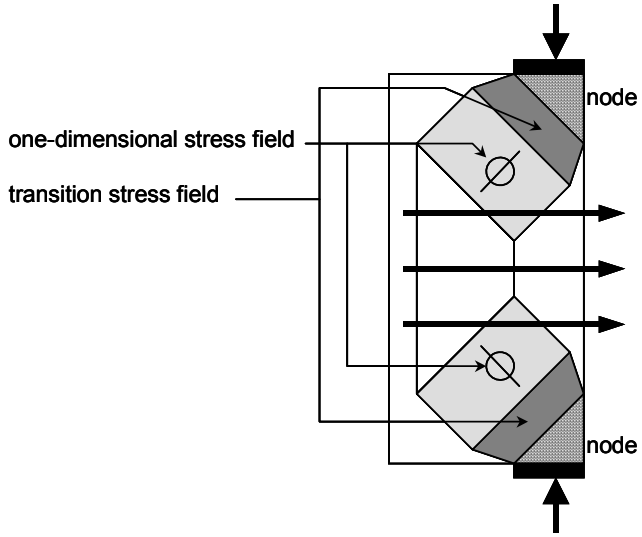

A) Transition Stress Field Tapering to the Node

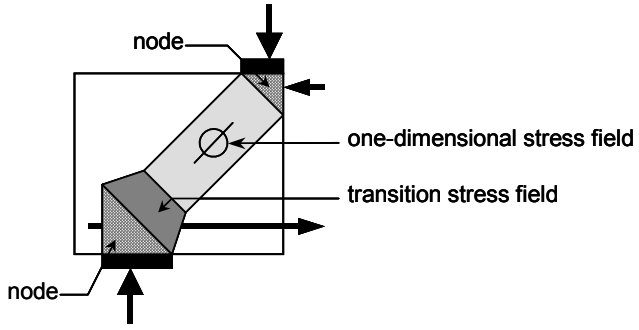

B) Transition Stress Field Enlarging to the Node

Figure 5.20 Examples Of the Transition Stress Field

The trapezoidal transition stress field is composed of four triangular stress fields that are in equilibrium with each other and the one-dimensional stress fields on either end of the transition length.
The trapezoidal stress field separated by each triangular stress field is shown in Figure 5.21. At the external boundaries of the trapezoid the normal stresses due to the adjoining one-dimensional stress fields disappear leaving the stress state inside triangles AOC and BOD one dimensional and parallel to AC and DB. The tensile force T results in the one dimensional stress state inside triangles ACO and BDO acting at angle α with respect to the one-dimensional stresses acting on surfaces CD and AB. The tensile force T acts across OF while an equal and opposite compressive force acts across OE. If the intensities of the one-dimensional stress field are known then the tensile force T depends only on the length of the transition area dictated by α. To define the length of the transition area, the compressive stress acting on OE is set equal to the compressive strength of the concrete defining the position of point O and the transition length. The tensile strength of concrete can be set at one value or be reduced according to the intensity of the compressive stresses present in the one-dimensional stress fields.

Equation 5-2 was derived by M. Schlaich that relates the length of the transition area in proportion to the initial width of the larger one dimensional stress field. Equation 5-2 is plotted in Figure 5.22 for various values of the design strength of the node and a tensile capacity of concrete equal to 10% of the compressive capacity.

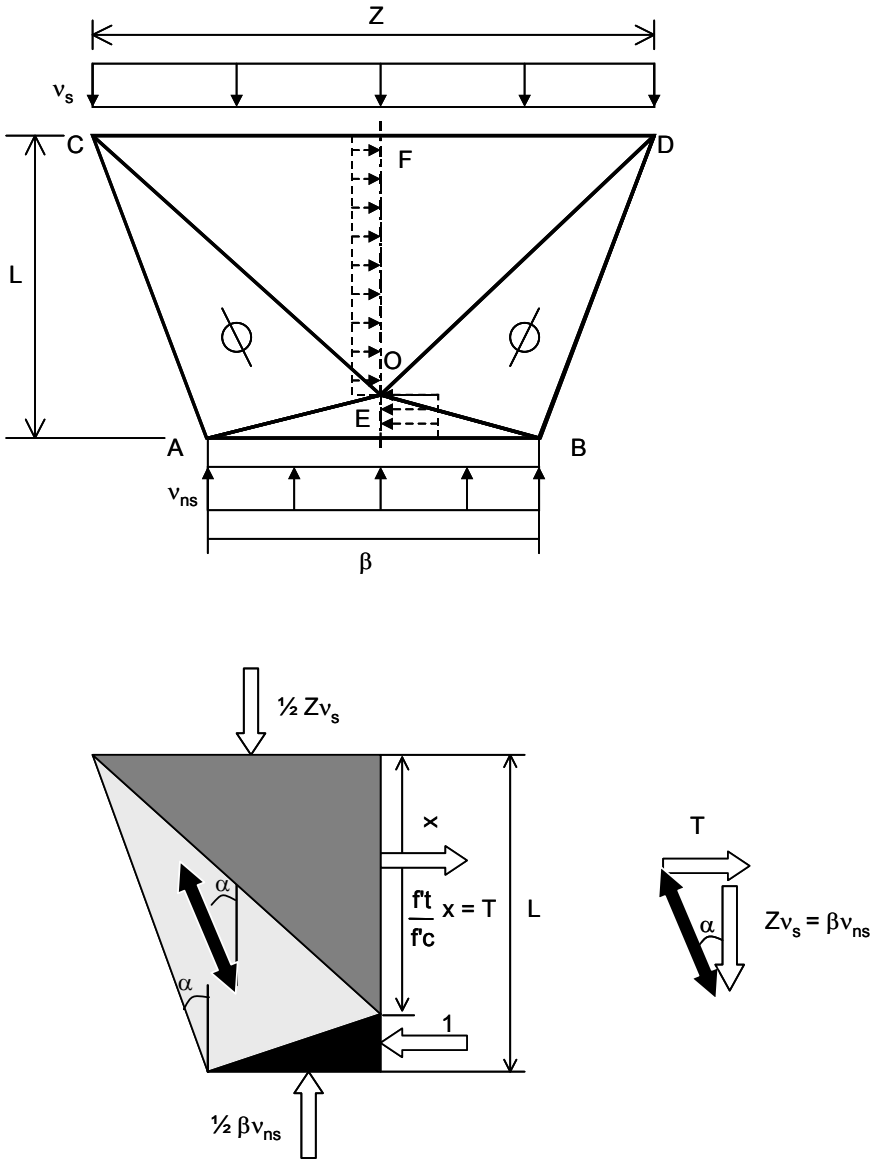

Figure 5.21 Transition Stress Field Adapted from [46]

$$\psi = \frac{1}{2} \cdot \sqrt{\frac{1 + \frac{f't}{f'c}}{\frac{f't}{f'c}} \cdot \frac{\nu s}{\nu ns} \cdot \left| \nu s - \nu ns \right|} \qquad (5\text{-}2)$$

where:

$$\psi = \frac{Z}{L}$$

$$\nu s = \frac{\sigma strut}{f'c}$$

$$\nu ns = \frac{\sigma node\_strut\_interface}{f'c}$$

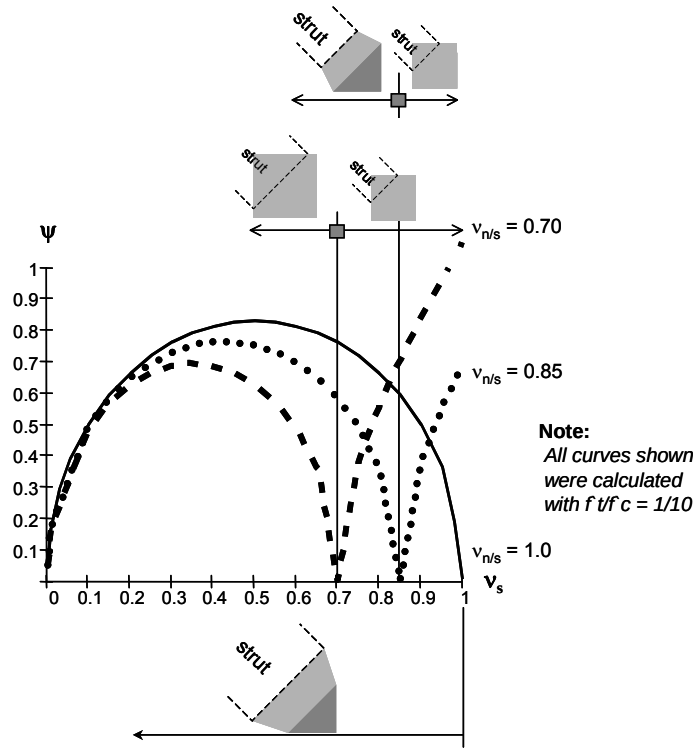

Figure 5.22 ψ- ν_s Relationship with Differing Values of ν_{ns}

As seen in Figure 5.22 for values of ν_s less than nodal-strut compression limit the strut tapers to the node, and for values grater than the node-strut compression limit, the strut enlarges to the node. The latter case may apply to nodes anchoring reinforcement in which the biaxial tension associated with the anchorage of the reinforcement might limit the compressive stress at the node-strut interface as shown in Figure 5.20 B.

The transition stress field is a planar model as shown in Figure 5.22 that indirectly incorporates a biaxial failure criterion. The planar model may be improved by adding a stress tensor in the third dimension, but is beyond the scope of this phase of the research project. The elegancy of the transition stress field lies in the fact that any biaxial failure criterion can be implemented. To illustrate this point 3 different biaxial failure criteria were investigated which are in the form of Kupfer's [23] envelope for planar stress.

The first failure criterion was developed using 3 data points obtained in the experimental program and is shown in Figure 5.23. The first point (point i) was derived from the average tensile stress and compressive stress from the split cylinders tested, the second point (point ii) was computed by integrating the best fit curve of the tensile stress in the reinforcement (Figure 4.13) just before cracking over the area of concrete between the nodes and dividing by the mean modular ratio between all reinforcing steels and concrete used in fabrication of the specimens. The compressive stress corresponding to this tensile stress was taken as the average of the best-fit curve of the compressive stresses at the mid-height of the specimens for each geometrical condition of loading (Figure 4.22, Figure 4.23). The third point (point iii) was found by

averaging the cylinder strengths for all batches of concrete used and was the value to which all other values were normalized.

The two other bi-axial failure models compared in Figure 5.24 were the common failure criterion established by Chen and Drucker and given in the paper by M. Schlaich [46], as well as, a failure criterion that did not reduce the tensile stress from 0.1 f`c as the intensity of the compressive stress increased.

In Figure 5.24 6 values of ψ (eq.5-2) as function of the stress in the strut are plotted. In 3 of the plots a maximum value of 0.85 (ν_{ns}) for the node-strut interface was used and in 3 plots the maximum value of 1.0 at the node-strut interface was used. The discontinuity seen in the curves for ν_{ns} equal to 1.0 are the points at which the tensile stress begins to decrease which, in turn, increase the transition length. The area of the strut always remains a constant value only dependent on the ratio between the nodal compression limit and the stress in the strut since the normal force applied to these two faces are the same. The length of the transition area depends only on the value of α in Figure 5.21. As the tensile capacity of the concrete decreases based on the level of compressive stress applied to the strut face, the length of the transition area increases based on the value of α which is continually decreasing toward zero. At an angle of α equal to zero the transition area would no longer be trapezoidal; it would be square with length of the strut equal to the length of the node face and equal to the length of the transition area. This concept is shown in Figure 5.25. As the tensile capacity decreases at the point of discontinuity the value of ψ as a function of the level stress

applied to the strut becomes asymptotic with the square root of the ratio of the area of the node to the area of the strut.

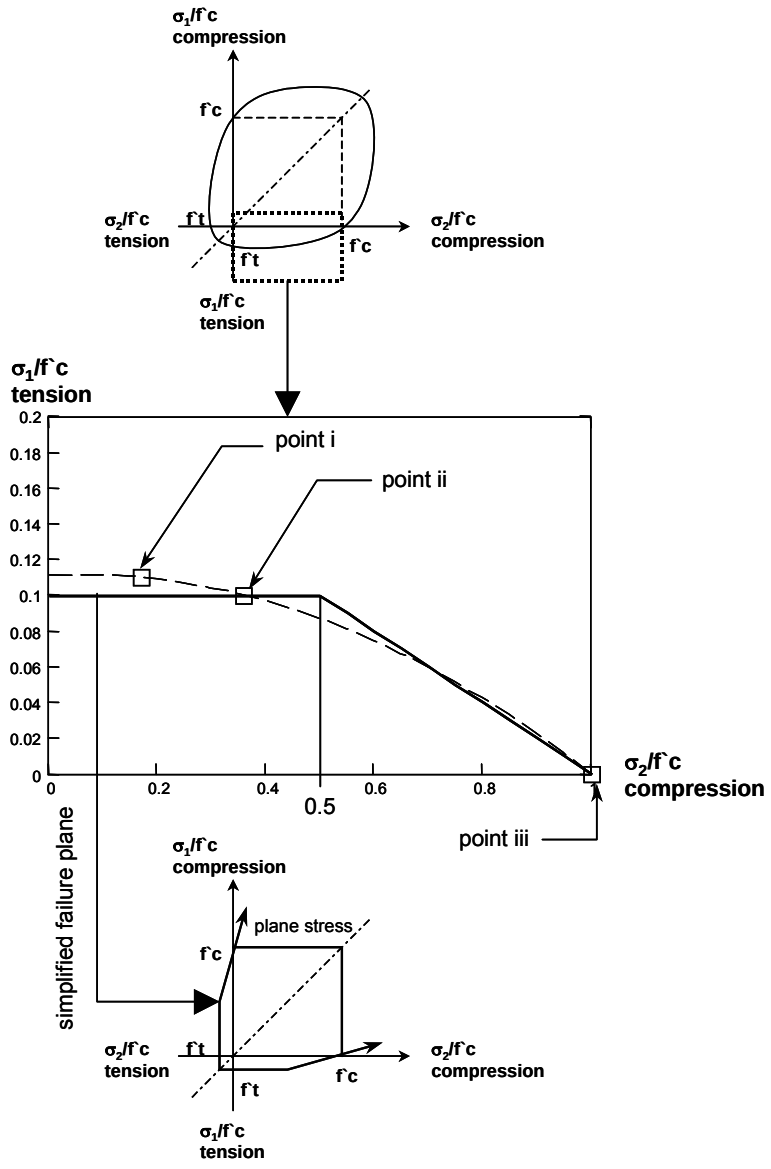

Figure 5.23 Example Bi-axial Failure Criterion Developed from the Experimental Program

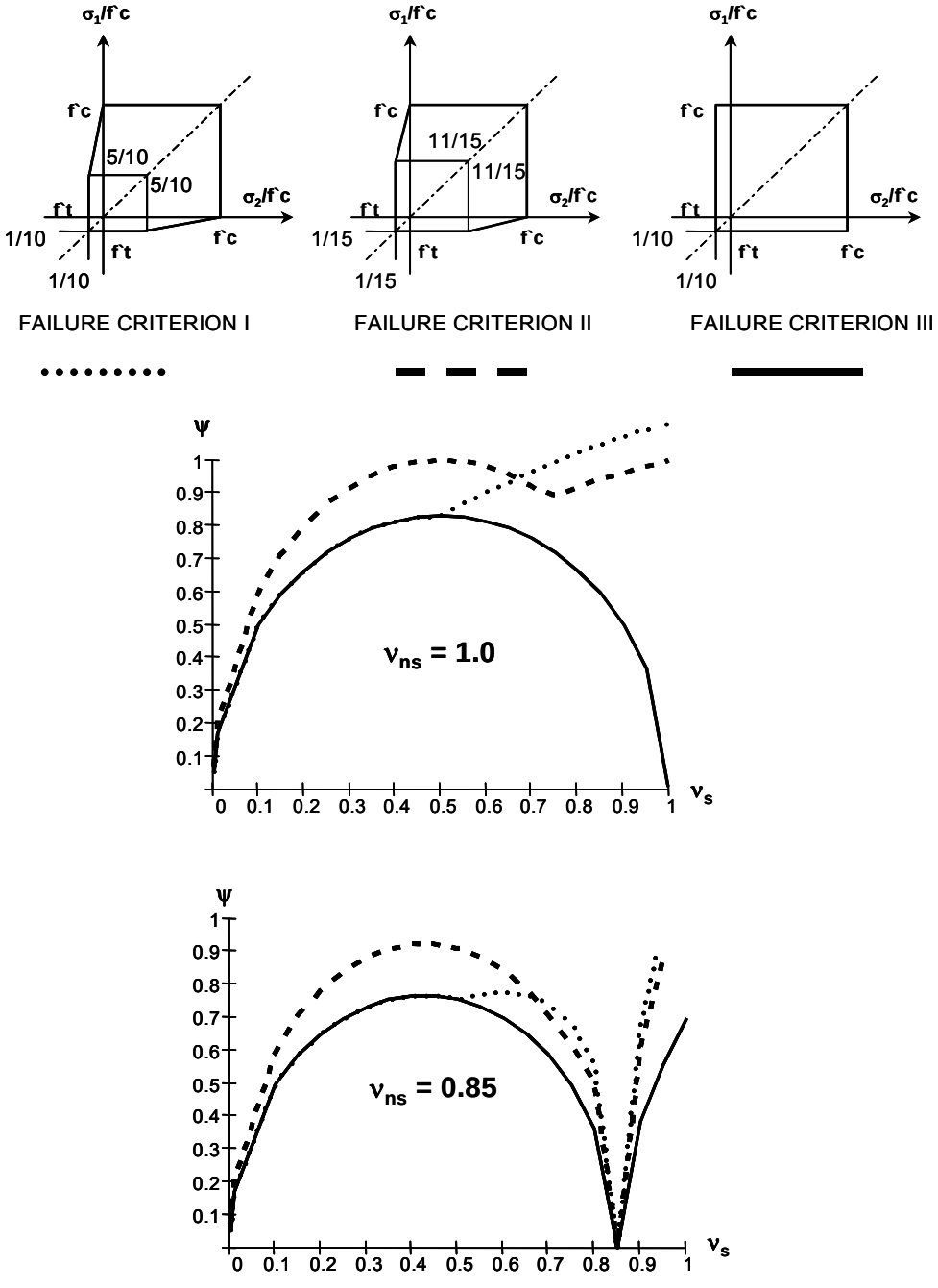

Figure 5.24 Effect of the Failure Criterion on the ψ-ν_s Relationship

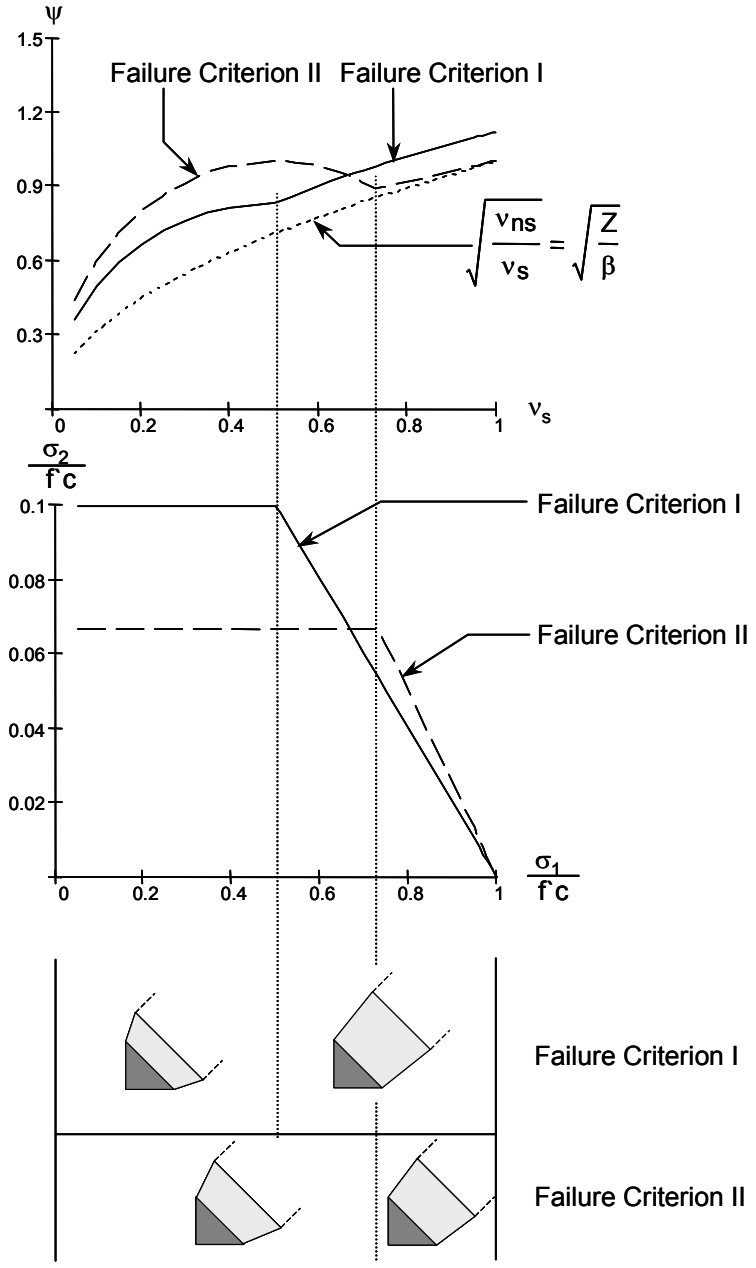

Figure 5.25 Explanation of the Point of Discontinuity in the ψ-ν_s Relationship

5.6 APPLICATION OF THE TRANSITION STRESS FIELD TO TEST DATA

The transition stress field as presented here is a planar model, and assumes that the stress fields at the node-strut interface and at the strut face are one-dimensional, as well as the normal force applied to the transition field is constant. With the fundamental assumptions behind the model understood, it may reasonably be applied to the specimens tested in the experimental program only after the basic parameters of the model are chosen. The two main parameters are the failure criterion used and the maximum allowable stress at the node-strut interface.

The value of α that determines the length of the transition area is only dependent on the level of stress applied at the strut face and the value of ψ which, in turn, is only dependent upon the failure criterion chosen. The decision made regarding the failure criterion used in the model was based on the advice of Drucker,

> *"…once we leave the elastic range, all hope disappears of finding both a simple and complete description of the mechanical behavior. When solving problems simplicity comes first. Full generality is not the goal; full generality is complete chaos and contains no information."*
>
> -Drucker-

and the fact that the observed failure planes were at maximum 10 inches away from the assumed isosceles triangle forming the singular node. The simplest failure criterion that results in the shortest transition length was Failure Criterion III as proven in Figure 5.24. Drucker might consider

failure Criterion III full generality; however, when used in combination with the transition stress field, the information provided by the combination proves to be valuable.

A correctly chosen value for the node compression limit (ν_{ns}) poses some epistemic uncertainty and needs further substation through experimental testing. It was decided that this value should be set equal to 1.0 indicating the face of the node could withstand compressive stresses equal to the compressive strength of concrete. The decision was made based on several planar specimens achieving values of ν_e greater than 1.0 and as high as 1.3 (S3-4). Since the concrete forming the node was intact in these specimens, the indication was that the area around the node-strut interface (area of the transition stress field) could be pushed into the realm of bi-axial compression if enough reinforcement was provided so that the value of ν_{ns} equal to 1.0 was a conservative estimate. It could be argued that the specimens tested within the experimental program are highly determinate and therefore were able to achieve such high values of compressive stress due to the fact that the specimens tested underwent a constant deformation. For indeterminate structures the failure deformation is not reached simultaneously for all elements, but at different deformation stages of the complete system. Therefore, the effective concrete strength should be reduced according to the theory of plasticity. This point is valid but depends on the level of stress redistribution in the structure considered. More experimental testing is needed to prove or refute this argument. For the time being a value of ν_{ns} = 1.0 is considered to be adequate.

Once the parameters of the model were chosen, the model could then be applied to the specimens. The transition stress field, when applied to one half of the singular node of the specimen is shown in Figure 5.26. The recorded bearing capacity form the specimens tested in the experimental program can then be applied to the model as the ν_s value. Using the bearing capacity as the ν_s term in the ψ - ν_s relationship (eq. 5-20) is justified by the assumptions that the nodes developed at the bearing plates of the specimens were hydrostatic and the assumption that the same force was applied to the strut face (area Z in Figure 5.26) and the node-strut interface (area β in Figure 5.26). Figure 5.27 shows the transition stress field superimposed on the nodal region of two specimens tested in the experimental program.

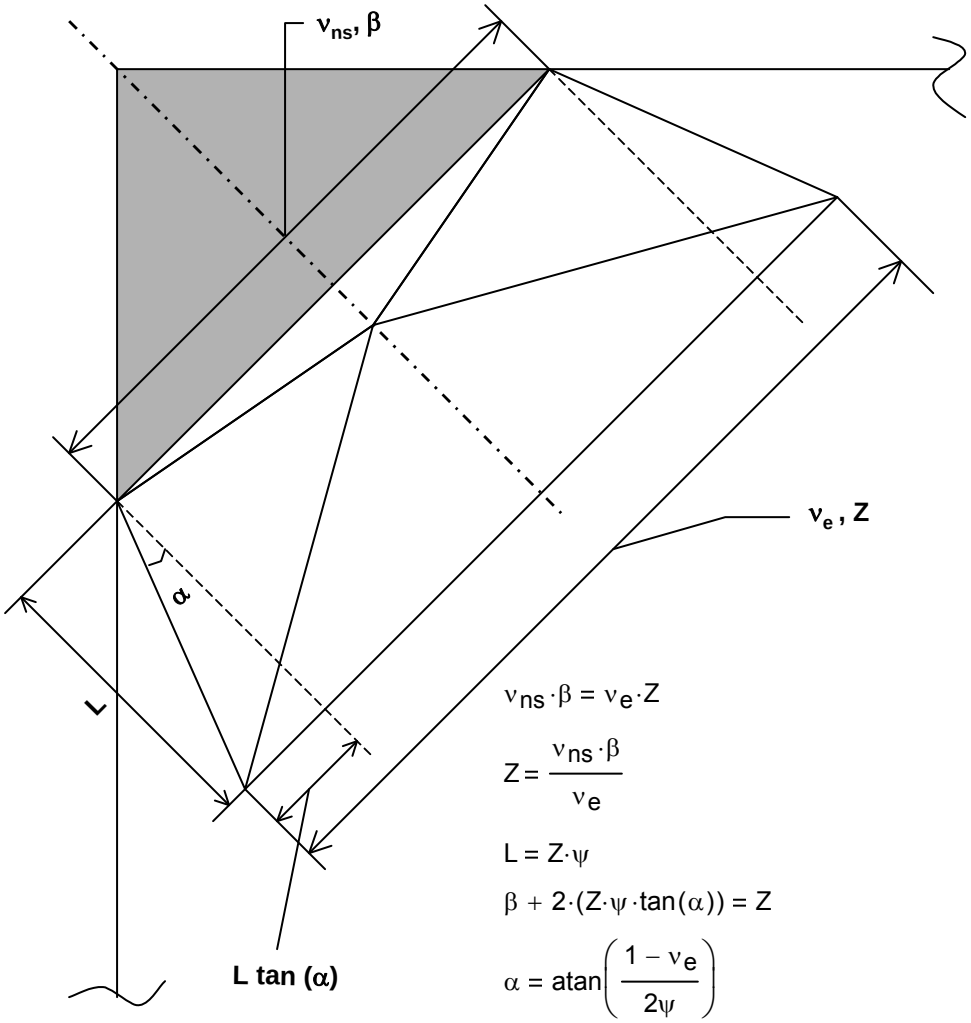

$$\nu_{ns} \cdot \beta = \nu_e \cdot Z$$

$$Z = \frac{\nu_{ns} \cdot \beta}{\nu_e}$$

$$L = Z \cdot \psi$$

$$\beta + 2 \cdot (Z \cdot \psi \cdot \tan(\alpha)) = Z$$

$$\alpha = \operatorname{atan}\left(\frac{1 - \nu_e}{2\psi} \right)$$

where:

$$\psi = \frac{1}{2} \cdot \sqrt{\frac{1 + \frac{f't}{f'c}}{\frac{f't}{f'c}} \cdot \frac{\nu_e}{\nu_{ns}} \cdot \left| \nu_{ns} - \nu_e \right|}$$

Figure 5.26 The Transition Stress Field Applied to the Singular Node of the Specimens

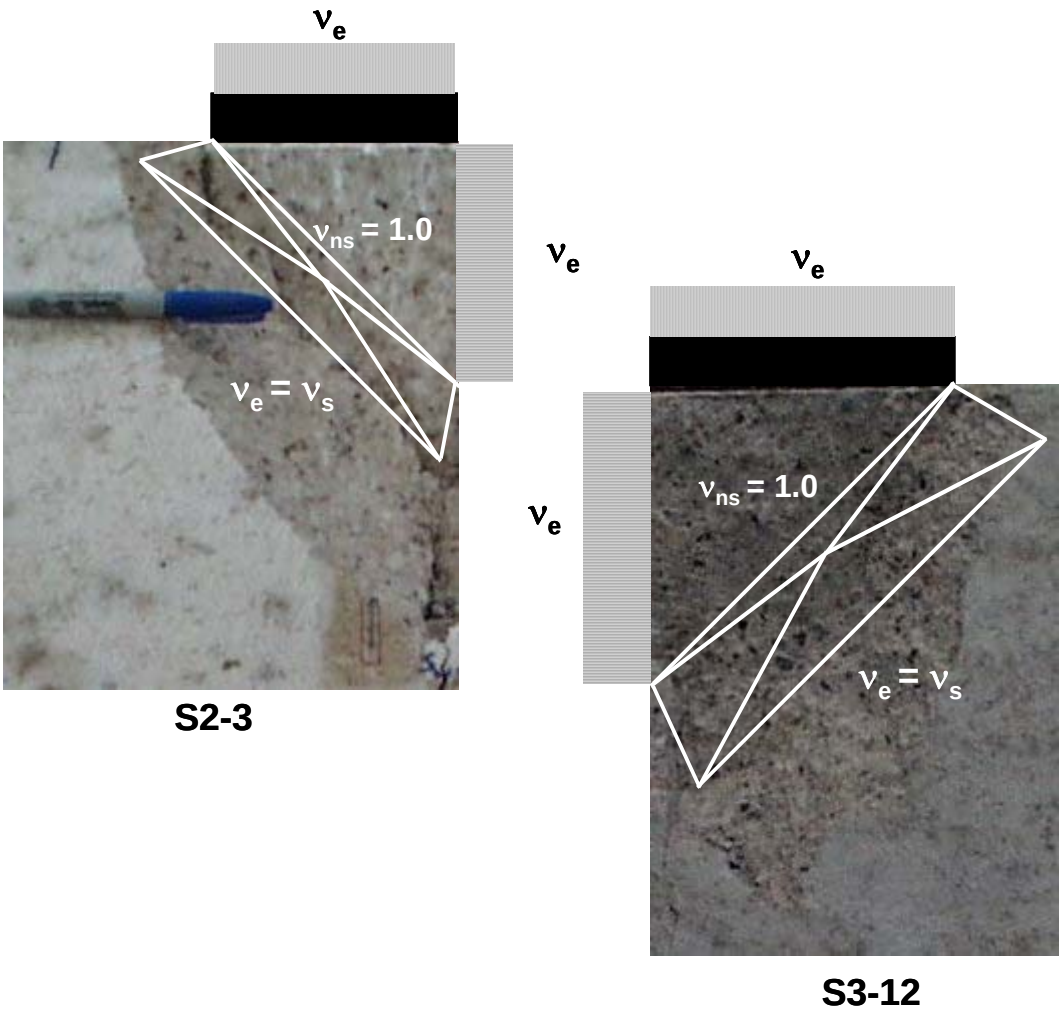

Figure 5.27 The Transition Stress Field Applied with Experimental Data

With test values of ν_e used in place of the ν_s values of the ψ - ν_s relationship, the decision to use ν_{ns} equal to 1.0, and using Failure Criterion III in Figure 5.24, a domain of the ψ - ν_s relationship could be established for the test specimens. The domain of the ψ - ν_s relationship for the specimens tested is plotted in Figure 5.28.

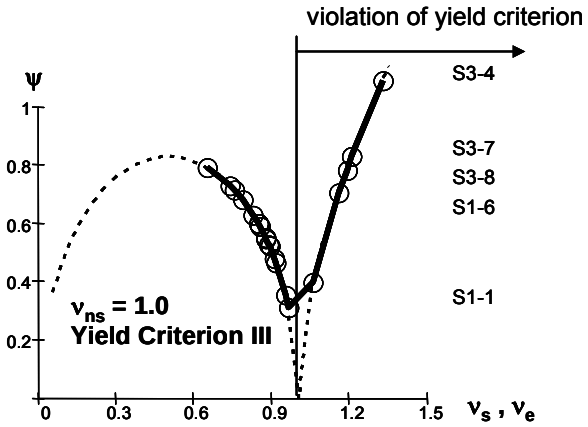

A) ψ - ν_e Relationship Used in Analysis

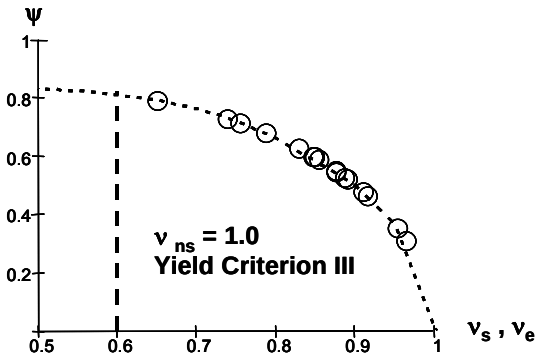

B) ψ - ν_e Domain Used in Analysis

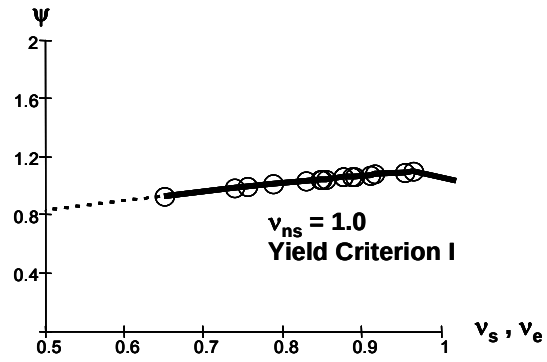

C) Possible ψ - ν_e Relationship

Figure 5.28 Domain of the ψ - ν_s Relationship Used

It can be seen from Figure 5.28 A. that certain test specimens violated the yield criterion for planar stress meaning that the strut failed at the node face in a manner conducive to biaxial compression having compressive capacities in the vicinity of 1.2 f`c. These specimens include the three specimens tested with 6 in by 6 in bearing plates, and two specimens fabricated in the first series that were 4 inches thick. Automatically excluded from this analysis were the two specimens tested in which the behavior was three dimensional (S3-9, S3-10), and the specimens in the first series that included confining reinforcement of the node by means of rectangular ties, which introduce tri-axial compression. For the specimens not automatically excluded from the analysis, the violation of the yield criterion possibly resulted in the fact that the area of steel provided relative to the area of bearing plate was sufficient to confine the stress field of the strut at the node-strut interface in a bi-axial manner. Figure 5.28 C is included to remind the reader that any failure criterion could have been used in this type of analysis. With further testing in regard to the failure criteria for concrete and maximum compressive capacities for nodes, a more suitable model might be implemented that could be easily incorporated into the analysis

The biggest influence on the compressive capacities of the specimens tested were the amount of transverse reinforcement crossing the vertical plane perpendicular to the axis at which the load was applied and the size of bearing plates used to load the specimens. A combination of these two parameters was plotted that renormalized the percentage of reinforcement with respect to the area of the bearing plate used to load

the specimens. The plot yielded a straight-line regression shown in Figure 5.29.

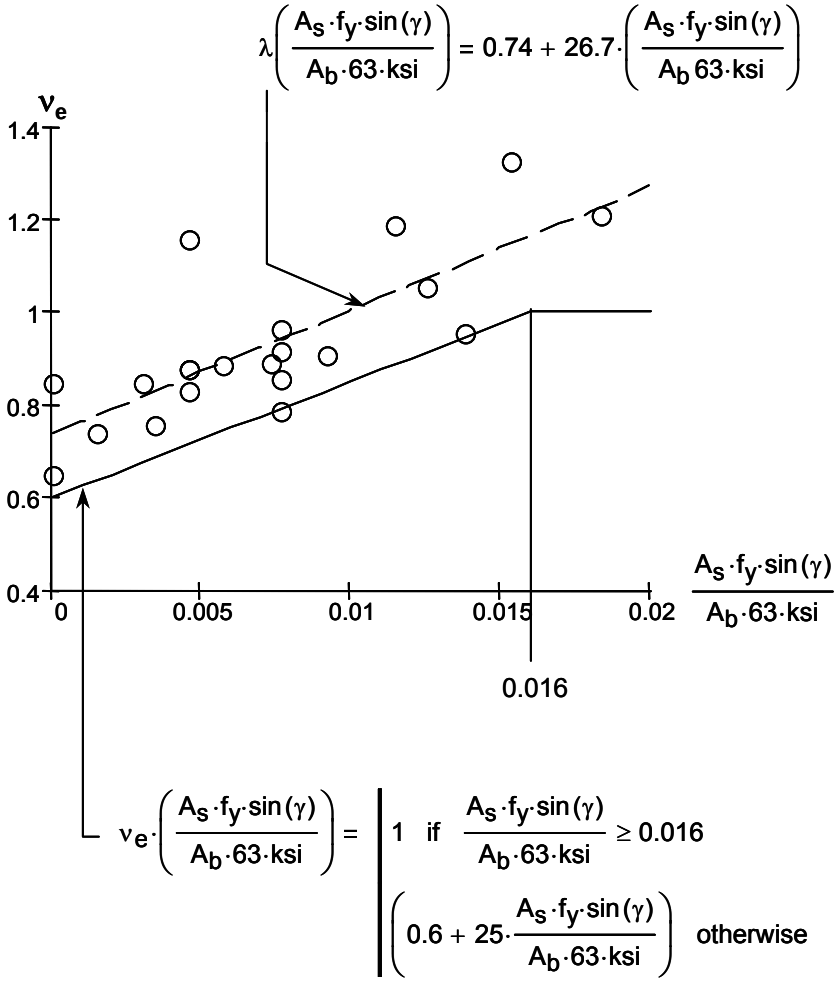

Figure 5.29 Linear Regression of the Strut Capacity based on the Area of Steel Provided Normalized to Area of the Bearing Plate

A reduction from the straight-line regression is also shown that was fit by passing a straight line through the two lowest values of compressive capacity based on the amount of steel provided relative to the bearing

plate dimensions. The reduction of the straight-line regression should provide conservative estimates of the bearing capacity. The reduction line was capped where it predicted a compressive capacity of the strut greater than 1.0 f`c. The cap is needed because the model used to analyze the specimens is planar with no allowance for bi-axial compression and values of ν_e greater than 1.0 violate the yield criterion. Substituting the conservative equation for the strut capacity based on the reinforcement provided for the ν_s term in the ψ - ν_s relationship with the parameters of ν_{ns} = 1.0 and Failure Criterion III in Figure 5.24 produces the curves shown in Figure 5.30.

As seen from Figure 5.30 as the amount of reinforcement increases so does the strut capacity until a maximum level of the compressive strength of the concrete is reached. While the compressive capacity of the strut face increases to 1.0 the length of the transition area in proportion of the area of the node face (L/β) decreases to zero and the area of the strut face (Z/β) relative to the area of the node face decreases to unity. The inverse of the (Z/β) value is ultimately the effective compressive force capable of the strut. It can also be seen that the transition length relative to the length of the node face takes the same form as the variation of α as a function of the amount of reinforcement provided. This similarity lies in the fact that the transition length is purely a function of α which is exclusively a function of the failure criterion chosen.

The maximum capacity of the strut occurs when the transition length equals zero meaning that the strut face becomes the node-strut interface. This is consistent with the observations of the confined failure planes, as well as, the fact that tensile stresses decrease at closer

distances to the introduction of applied stresses which enhances the compressive capacity.

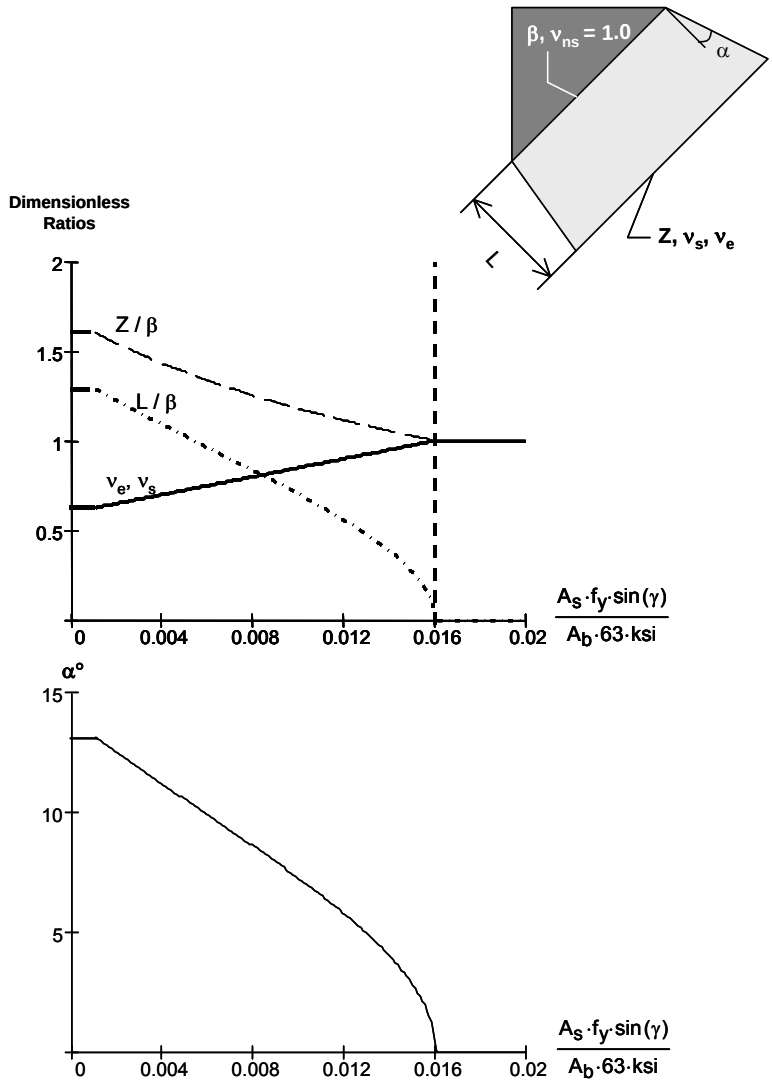

Figure 5.30 Transition Stress Field as a Function of the Reinforcement Provided

With no reinforcement provided, the maximum capacity of the strut is equal to 0.6 times the uni-axial compressive strength of concrete occurring at the maximum distance of 1.3 times the length of the node face. The maximum compressive force acts over the strut face equal to 1.6 times the length of the node face. If the length of the node face is set equal to 1.0 then α equals $\tan^{-1}$ ½(1.6-1.0)/1.3 which equals 13 degrees and is the same value for α depicted in Figure 5.30. The transition stress field when applied to two specimens within the experimental program in shown in Figure 5.31. As seen from Figure 5.31, the application of the transition stress field to both sides of the node leads to developing stress fields for the entire specimen. From the stress fields the strut-and-tie model shown in Figure 5.6 B can be envisioned as seen in Figure 5.32.

The ultimate load capable by the strut and hence the specimen is calculated by dividing the value of β which is always known by Z obtained from Figure 5.30 based on the amount of reinforcement provided and multiplying that value by the bearing area of the applied load. This value shown in Figure 5.31 is a simplification of the ultimate load obtained as shown in Figure 5.32. Finally, the geometry of the transition stress field should be checked to ensure that it does not overlap any other stress fields and is within the boundary of the structural element considered.

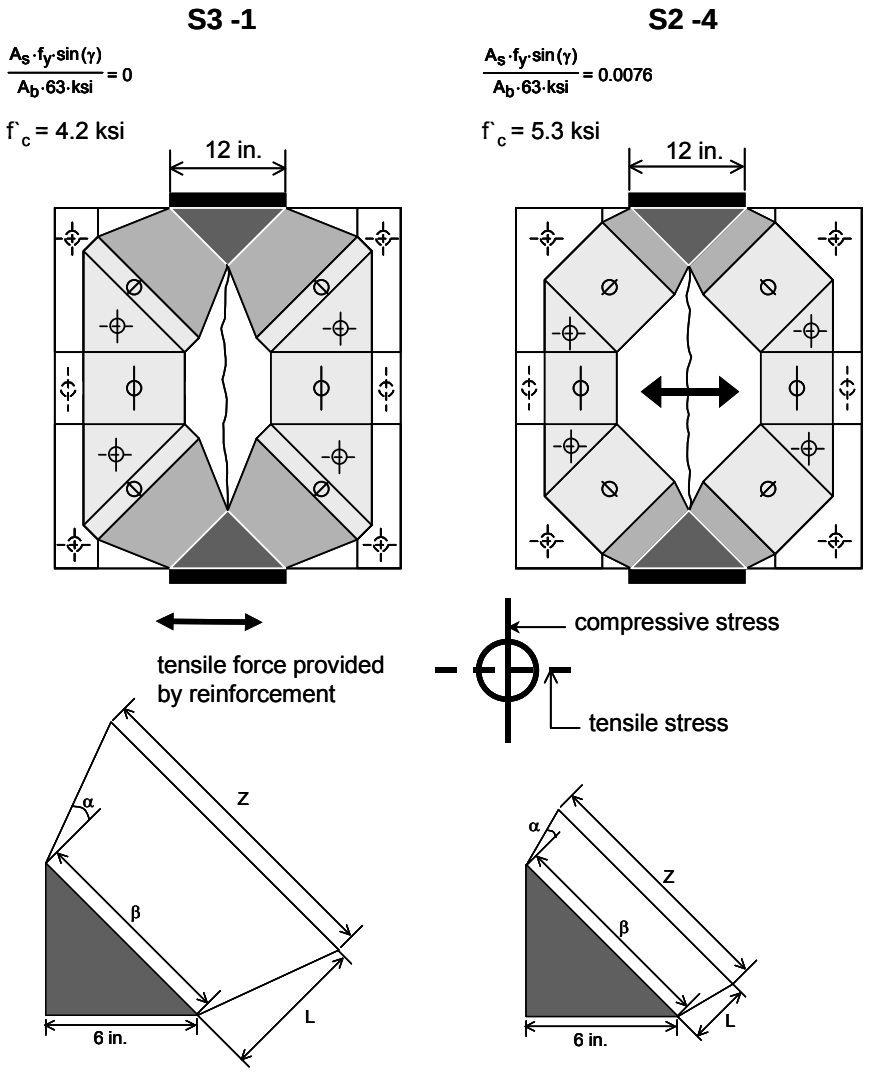

Figure 5.31 Stress Fields for Two Specimens

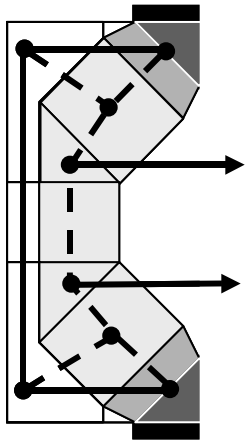

Figure 5.32 Strut-and-Tie Model obtained from the Stress Fields in Figure 5.31

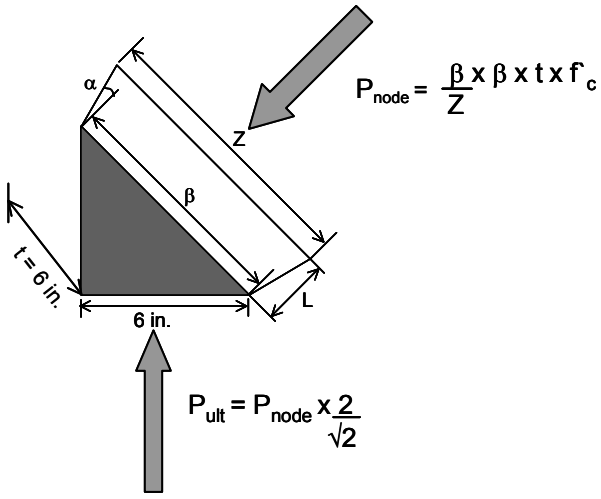

Figure 5.33 Obtaining the Ultimate load for a Strut from the Transition Stress Field

5.7 CONCLUSIONS

The objective of this research project was to either substantiate or refute the stress limitations for bottle-shaped struts given by ACI 318-02 Appendix A STM provisions and AASHTO LRFD 5.6 STM provisions and to unify the provisions for bottle-shaped struts given by each code. The ACI 318-02 Appendix A provisions provided a reinforcement ratio (ACI equation A-4) as an amount of reinforcement required to confine bottle-shaped struts to increase their compressive capacity. The substantiation of this amount of confining steel stipulated by ACI equation A-4 was necessary to meet the objective

The specimens tested within the experimental program constantly failed at higher levels of compressive stress than allowed by ACI or AASHTO. The AAHSTO expression for strut capacity (equation 5-1) based on active transverse tensile strains in the reinforcement did not reflect the behavior of the specimens tested, in that, the transverse strains in the reinforcement were developed passively through deformation of the specimen and had no detrimental effect on the compressive capacity of the strut as the strain in the steel increased.

The compressive capacity for bottle-shaped strut as a function of the amount of steel required to confine the strut is reported here as equation 5-3 taken from Figure 5.29 without the normalization with respect to the yield stress of the steel used in the fabrication of specimens.

$$\nu_e\left(\frac{A_s}{A_b}\cdot\sin(\gamma)\right) = \begin{cases} 1 & \text{if } \frac{A_s}{A_b}\cdot\sin(\gamma) > 0.016 \\ \left[0.6 + 25\cdot\left(\frac{A_s}{A_b}\cdot\sin(\gamma)\right)\right] & \text{otherwise} \end{cases} \tag{5-3}$$

ACI equation A-4 was reported here in Chapter 1 as equation 1-4.

$$\sum_{i=1}^{n} \frac{A_s}{b\cdot s_i}\cdot\sin(\gamma) \geq 0.003 \tag{1-4}$$

The ACI 318-02 provisions stipulate that if a reinforcement ratio of 0.003 or greater is provided to confine the transverse spreading of the bottle-shaped strut then the strut may resist compressive stresses not exceeding 0.64 f`c. If the reinforcement ratio called for by equation 1-4 is not provided then a bottle-shaped strut may resist compressive stresses not exceeding 0.51 f'c.

To allow for a comparison between equation 1-4 and equation 5-4 it must be assumed that the dimensions of the bearing plate (A_b) in equation 5-4 are a unit dimension along the length of the structural element and equal to the thickness of the element. For this condition, equation 5-4 predicts exactly half the amount of steel (0.0015) for a compressive capacity of 0.64 f'c. Furthermore, equation 5-4 allows a bottle-shaped

strut to resist compressive stresses equal to the compressive strength of the concrete if a reinforcement ratio of 0.016 or greater is provided.

M. Schlaich [46] proposed a geometrical stress field that is statically admissible between two one-dimensional stress fields. This transition stress field developed by M. Schlaich was used to describe the observed and recorded behavior of the bottle-shaped struts developed within the specimens tested. The transition stress field is significant because it employs a bi-axial failure criterion for concrete under compressive and tensile stresses, while simultaneously providing a physical geometry for the stress fields originating from an applied source of loading. The added information about the geometry of the stress fields helps the designer in determining sufficient dimensioning of the members of a truss model.

The rudimentary failure criterion used in the stress field developed by M. Schlaich [46] as it was engaged to the specimens may be altered with further experimental investigation to incorporate bi-axial compression and tension in the third dimension or any other combination of stresses in the three principal axes of a structural element.

With further investigation, the stress field may also be used to describe the behavior of struts anchored by CCT nodes. Since the transition stress field depends on allowable values of compressive stresses placed on various nodes, failure criteria may be developed that link node and strut behavior for singular nodes. The correlation between nodes and struts is ideal because the critical stresses within strut-and-tie models are usually those at the node-strut interface of singular nodes.

References

1. "AASHTO LRFD Bridge Design Specifications, 2nd ed.," American Association of State Highway and Transportation Officials, Washington, DC, 1998.

2. ACI 318-02, "Building Code Requirements for Structural Concrete and Commentary," American Concrete Institute, Farmington Hills, Michigan, October 2002.

3. ASTM A615/A615M-96a, "Standard Specification for Deformed and Plain Billet-Steel for Concrete Reinforcement," American Society for Testing and Materials, West Conshohocken, Pennsylvania, September 1996.

4. ASTM C39/C39M-99, "Standard Test Method for Compressive Strength of Cylindrical Concrete Specimens," American Society for Testing and Materials, West Conshohocken, Pennsylvania, September 1999.

5. ASTM C496-96, "Standard Test Method for Splitting Tensile Strength of Cylindrical Concrete Specimens," American Society for Testing and Materials, West Conshohocken, Pennsylvania, September 1996.

6. CSA Standard CAN3-A23.3-94, "Design of Concrete Structures for Buildings with Explanatory Notes," Canadian Standards Association, Rexdale, Ontario, 1994.

7. "Ontario Highway Bridge Design Code, 3rd Edition," Canadian Ministry of Transportation, Toronto, Ontario, Canada, 1991.

8. PCI Design Handbook 3rd Edition, Prestressed Concrete Institute, Chicago, Illinois, 1985.

9. "Structural Concrete: The Textbook on Behavior, Design, and Performance - Volume 2: Basis of Design," Federation Internationale du Beton (FIB), Lausanna, Switzerland, July 1999.

10. Adebar, P., Kuchma, D., and Collins, M.P., “Strut-and-Tie Models for the Design of Pile Caps: An Experimental Study,” ACI Structural Journal, Proceedings Vol. 87, No. 1, pg. 81-92, Detroit, Michigan, January-February 1990.

11. Adebar, P. and Zhou, Z., “Bearing Strength of Compressive Struts Confined by Plain Concrete,” ACI Structural Journal, Proceedings Vol. 90, No. 5, pg. 534-541, Detroit, Michigan, September-October 1993.

12. Adebar, P. and Zhou, Z., “Design of Deep Pile Caps by Strut-and-Tie Models,” ACI Structural Journal, Proceedings Vol. 93, No. 4, pg. 437-448, Detroit, Michigan, July-August 1996.

13. Ahmed, T., Burley, E., Rigden, S., “Bearing Capacity of Plain and Reinforced Concrete Loaded over a Limited Area,” ACI Structural Journal, Vol. 95, No. 1, January-February 1998.

14. Ahmed, T., Burley, E., Rigden, S., “Effect of Alkali Silica Reaction on the Bearing Capacity of Plain and Reinforced Concrete,” ACI Structural Journal, Vol. 96, No. 4, July-August 1999.

15. Bergmeister, K., Breen, J.E., Jirsa, J.O., and Kreger, M.E., “Detailing for Structural Concrete,” Center for Transportation Research Report CTR 0-1127-3F, Austin, Texas, May 1993.

16. Breen, J.E., Burdet, O., Roberts, C., Sanders, D., and Wollmann, G., “Anchorage Zone Reinforcement for Post-Tensioned Concrete Girders,” National Cooperative Highway Research Program Report No. 356, Washington, DC, 1994.

17. Burdet, O, “Analysis and Design of Anchorage Zones in Post-Tensioned Concrete Bridges,” Ph.D. Dissertation, The University of Texas at Austin, Austin, Texas, August 1990.

18. Chen, B.S., Hagenberger, M.J., and Breen, J.E., “Evaulation of Strut-and-Tie Modeling Applied to Dapped Beam with Opening,” ACI Structural Journal, Vol. 99, No. 4, July-August 2002.

19. Chen, W.F., “Double Punch Test for Tensile Strength of Concrete,” Journal of the American Concrete Institute, Proceedings Vol. 67, No. 12, pg. 993-995, Detroit, Michigan, December 1970.

20. Baumann, Peter, “Die Druckfelder bei der Stahlbetonbemessung mit Stabwerkmodellen,” Institut fur Massivbau, University of Stuttgart, Germany, 1988.

21. Hawkins, N.M., “The Bearing Strength of Concrete: 1. Loading Through Rigid Plates Covering Part of the Full Supporting Area,” The University of Sydney, Research Report No. 54, Sydney, Australia, March 1967.

22. Hawkins, N.M., “The Bearing Strength of Concrete: 2. Loading Through Flexible Plates,” The University of Sydney, Research Report No. 84, Sydney, Australia, August 1967.

23. Kupfer, H., Hilsdorf, H.K., and Rusch, H., “Behavior of Concrete Under Biaxial Stresses,” Journal of the American Concrete Institute, Proceedings Vol. 66, No. 8, pg. 656-666, Detroit, Michigan, August 1969.

24. Lampert, P. and Thürlimann, B., “Ultimate Strength and Design of Reinforced Concrete Beams in Torsion and Bending,” IASBE Publications, No. 31-1, pg. 107-131, Zurich, Switzerland, 1971.

25. MacGregor, J.G., “Reinforced Concrete: Mechanics and Design (3rd Edition),” Prentice Hall, Upper Saddle River, New Jersey, 1997.

26. Marti, P., “Basic Tools in Reinforced Concrete Beam Design,” Journal of the American Concrete Institute, Proceeding Vol. 82, No. 1, pg. 46-56, Detroit, Michigan, January-February 1985.

27. Marti, P., “Size Effect in Double-Punch Tests on Concrete Cylinders,” ACI Materials Journal, Proceedings Vol. 86, No. 6, pg. 597-601, Detroit, Michigan, November-December 1989.

28. Marti, P., “Truss Models in Detailing,” Concrete International, Vol. 7, No. 12, pg. 66-73, Detroit, Michigan, December 1985.

29. Maxwell, B.S. and Breen, J.E., “Experimental Evaluation of Strut-and-Tie Model Applied to Deep Beam with Opening,” ACI Structural Journal, Proceedings Vol. 97, No. 1, pg. 142-148, Detroit, Michigan, January-February 2000.

30. Mitchell, D. and Collins, M., “Diagonal Compression Field Theory – A Rational Model for Structural Concrete in Pure Torsion,” Journal of the American Concrete Institute, Proceedings Vol. 71, No. 8, pg. 396-408, Detroit, Michigan, August 1974.

31. Mörsch, E., “Der Eisenbetonbau, seine Theorie und Anwendung (Reinforced Concrete, Theory and Application),” Stuggart, Germany, 1902.

32. Mörsch, E., “Über die Berechnung der Gelenkquader,” Beton-und Eisen, No. 12, pg. 156-161, Stuttgart, Germany, 1924.

33. Muttoni, A., Schwartz, J. and Thürlimann, B.,”Design of Concrete Structures with Stress Fields,” Birkhaüser, Verlag, Switzerland.

34. Niyogi, S.K., “Bearing Strength of Concrete – Geometric Variations,” ASCE Journal of Structural Engineering, Vol. 99, No. 7, pgs. 1471-1490, New York, New York, July 1973.

35. Niyogi, S.K., “Concrete Bearing Strength – Support, Mix, Size Effect,” ASCE Journal of Structural Engineering, Vol. 100, No. 8, pgs. 1685-1702, New York, New York, August 1974.

36. Niyogi, S.K., “Bearing Strength of Reinforced Concrete Blocks,” ASCE Journal of Structural Engineering, Vol. 101, No. 5, pgs. 1125-1137, New York, New York, May 1975.

37. Ramirez, J. and Breen, J.E., “Proposed Design Procedures for Shear and Torsion in Reinforced and Prestressed Concrete,” Center for Transportation Research Report No. 248-4F, Austin, Texas, 1983.

38. Reineck, K.H. (Ed), “Examples for the Design of Structural Concrete with Strut-and-Tie Models,” The American Concrete Institute, SP-208, Farmington Hillls, Michigan, 2002.

39. Roberts, C., “Behavior and Design of the Local Anchorage Zone of Post-Tensioned Concrete Members,” Master’s Thesis, The University of Texas at Austin, Austin, Texas, May 1990.

40. Rogowsky, D.M. and MacGregor, J.M., “Shear Strength of Deep Reinforced Concrete Continuous Beams,” The University of Alberta, Structural Engineering Report No. 110, Edmonton, Alberta, November 1983.

41. Rogowsky, D.M. and MacGregor, J.M., “Design of Reinforced Concrete Deep Beams,” Concrete International, Vol. 6, No. 8, pg. 49-58, August 1986.

42. Richart, F., “An Investigation of Web Stresses in Reinforced Concrete Beams,” University of Illinois Engineering Experiment Station, Bulletin No. 166, Urbana, Illinois, 1927.

43. Ritter, W., “Die Bauweise Hennebique (The Hennebique System),” Schweizerische Bauzeitung, Bd. XXXIII, No. 7, Zurich, Switzerland, 1899.

44. Sanders, D. “Design and Behavior of Anchorage Zones in Post-Tensioned Structures,” Ph.D. Dissertation, The University of Texas at Austin, Austin, Texas, August 1990.

45. Schlaich, J., Schäfer, K., and Jennewein, M., “Towards a Consistent Design of Structural Concrete,” PCI Journal, Vol. 32, No. 3, pg. 74-150, Chicago, Illinois, May-June 1987.

46. Schlaich, M., and Anagnostou, G., “Stress Fields for Nodes of Strut-and-Tie Models,” Journal of Structural Engineering, Vol. 116, No. 1, pg.13-23, January 1990.

47. Thompson, K. “The Anchorage Behavior of Headed Reinforcement in CCT Nodes and Lap Slpices,” Ph.D. Dissertation, The University of Texas at Austin, Austin, Texas, May 2002.

48. Vecchio, F.J. and Collins, M.P., “The Modified Compression Field Theory for Reinforced Concrete Elements Subjected to Shear,” Journal of the American Concrete Institute, Proceedings Vol. 83, No. 2, pg. 219-231, Detroit, Michigan, March-April 1986.

49. Vecchio, F.J. and Collins, M.P., “The Response of Reinforced Concrete to In-Plane Shear and Normal Stresses,” The University of Toronto, Department of Civil Engineering Publication No. 82-03, Toronto, Canada, 1982.

50. Williams, A., “The Bearing Capacity of Concrete Loaded Over a Limited Area,” Cement and Concrete Association, Technical Report 526, Wexham Springs, Slough, The United Kingdom, August 1979.

51. Wollman, G. “Anchorage Zones in Post-Tensioned Concrete Structures,” Ph.D. Dissertation, The University of Texas at Austin, Austin, Texas, May 1992.

52. Young, M.J., “Performance of Headed Reinforcing Bars in CCT Nodal Regions,” Master’s Thesis, The University of Texas at Austin, Austin, Texas, August 2000.